2004-03

Modeling optical turbulence with COAMPS during two observation periods at Vandenberg AFB

Horne, Jimmy D., Jr.

Monterey, California. Naval Postgraduate School

NAVAL POSTGRADUATE SCHOOL

MONTEREY, CALIFORNIA

THESIS

MODELING OPTICAL TURBULENCE WITH COAMPS DURING TWO OBSERVATION PERIODS AT VANDENBERG AFB

by

Jimmy D. Horne Jr.

March 2004

Thesis Advisor: Douglas Miller

Approved for public release; distribution is unlimited.

THIS PAGE INTENTIONALLY LEFT BLANK

REPORT DOCUMENTATION PAGE	Form Approved OMB No. 0704-0188

1. AGENCY USE ONLY *(Leave blank)*	2. REPORT DATE	3. REPORT TYPE AND DATES COVERED
	March 2004	Master's Thesis

4. TITLE AND SUBTITLE:	5. FUNDING NUMBERS
Modeling Optical Turbulence with COAMPS During Two Observation Periods at Vandenberg AFB	
6. AUTHOR(S) Jimmy D. Horne	
7. PERFORMING ORGANIZATION NAME(S) AND ADDRESS(ES) Naval Postgraduate School Monterey, CA 93943-5000	**8. PERFORMING ORGANIZATION REPORT NUMBER**
9. SPONSORING /MONITORING AGENCY NAME(S) AND ADDRESS(ES) N/A	**10. SPONSORING/MONITORING AGENCY REPORT NUMBER**

11. SUPPLEMENTARY NOTES The views expressed in this thesis are those of the author and do not reflect the official policy or position of the Department of Defense or the U.S. Government.

12a. DISTRIBUTION / AVAILABILITY STATEMENT	12b. DISTRIBUTION CODE
Approved for public release; distribution is unlimited.	

13. ABSTRACT (maximum 200 words)

The objective of this thesis is to investigate the forecastability of optical turbulence using the U.S. Navy's Coupled Ocean Atmosphere Mesoscale prediction System (COAMPS). First, a detailed synoptic study was performed over the Eastern Pacific region for observation periods in October 2001 and March 2002 to focus on mesoscale features affecting Vandenberg AFB. Second, a modified version of COAMPS version 2.0.16 model output was evaluated to ensure reasonable modeling of the mesoscale. Next, temperature and dewpoint temperature vertical profiles of COAMPS, modified with the Turbulent Kinetic Energy (TKE) Method, were compared with balloon-launched rawinsondes, initially, then with higher resolution thermosondes. Optical turbulence parameters were then calculated from the data and a comparison between synthetic profiles and thermosonde-derived profiles were qualitatively and quantitatively studied. Then the vertical resolution of the model was increased for selected forecasts to determine the potential for forecast improvement.

14. SUBJECT TERMS	15. NUMBER OF PAGES
Atmospheric Modeling, COAMPS, Modeling, Numerical Modeling, Optical Turbulence, Optics, TKE Method, TKE-Free Method, Turbulence, Turbulent Kinetic Energy	163
	16. PRICE CODE

17. SECURITY CLASSIFICATION OF REPORT	18. SECURITY CLASSIFICATION OF THIS PAGE	19. SECURITY CLASSIFICATION OF ABSTRACT	20. LIMITATION OF ABSTRACT
Unclassified	Unclassified	Unclassified	UL

NSN 7540-01-280-5500 Standard Form 298 (Rev. 2-89)
Prescribed by ANSI Std. 239-18

THIS PAGE INTENTIONALLY LEFT BLANK

Approved for public release; distribution is unlimited.

MODELING OPTICAL TURBULENCE WITH COAMPS DURING TWO OBSERVATION PERIODS AT VANDENBERG AFB

Jimmy D. Horne
Lieutenant Commander, United States Navy
B.S., Louisiana State University, 1994

Submitted in partial fulfillment of the
requirements for the degree of

MASTER OF SCIENCE IN METEOROLOGY AND PHYSICAL OCEANOGRAPHY

from the

NAVAL POSTGRADUATE SCHOOL
March 2004

Author: Jimmy D. Horne Jr.

Approved by: Douglas Miller
Thesis Advisor

Carlyle Wash
Second Reader

Carlyle Wash
Chairman, Department of Meteorology

THIS PAGE INTENTIONALLY LEFT BLANK

ABSTRACT

The objective of this thesis is to investigate the forecastability of optical turbulence using the U.S. Navy's Coupled Ocean Atmosphere Mesoscale prediction System (COAMPS). First, a detailed synoptic study was performed over the Eastern Pacific region for observation periods in October 2001 and March 2002 to focus on mesoscale features affecting Vandenberg AFB. Second, a modified version of COAMPS version 2.0.16 model output was evaluated to ensure reasonable modeling of the mesoscale. Next, temperature and dewpoint temperature vertical profiles of COAMPS, modified with the Turbulent Kinetic Energy (TKE) Method, were compared with balloon-launched rawinsondes, initially, then with higher resolution thermosondes. Optical turbulence parameters were then calculated from the data and a comparison between synthetic profiles and thermosonde-derived profiles were qualitatively and quantitatively studied. Then the vertical resolution of the model was increased for selected forecasts to determine the potential for forecast improvement.

THIS PAGE INTENTIONALLY LEFT BLANK

TABLE OF CONTENTS

LIST OF FIGURES

THIS PAGE INTENTIONALLY LEFT BLANK

LIST OF TABLES

THIS PAGE INTENTIONALLY LEFT BLANK

ACKNOWLEDGMENTS

First and foremost, I would like to recognize the love, support, and devotion that my wife, Kathi, and son, Christian, have given me while at the Naval Postgraduate School. All things I do, I do for them.

Additionally, I would like to express my most sincere gratitude to my advisor, Dr. Douglas Miller. His insight and direction helped me stay the course and achieve the goals I had set for this thesis. Also deserving recognition are Robert Creasey, LCDR Dan Eleuterio, LCDR Dominick “Nick” Vincent, LCDR Dave Brown, Brian Blair, and Mary Jordan for the various technical support and sanity checks they provided me.

Finally, I would like to thank Lt. Cmdr. Andrew “Andy” Moys of Her Majesty’s Royal Navy, a dear friend, for the many ‘focusing’ sessions we had at the Trident Room. Though we may not have solved any of the world’s problems, we certainly thought we could.

THIS PAGE INTENTIONALLY LEFT BLANK

I. INTRODUCTION

A. MOTIVATION

With the expanding application of lasers by the military, the challenge of predicting atmospheric effects on these systems has attracted increasing interest. The dynamics of an ever-changing atmosphere have profound effects on the performance of high-energy laser (HEL) systems in the form of transmission loss, scattering, absorption, obstruction, and optical turbulence degradation. Whether applied to missile defense, laser communications, or weapon's system targeting, optical turbulence degradation will act to limit the systems effectiveness and range.

The capability to predict HEL's performance under specific atmospheric conditions could dramatically enhance the system viability. To do this, higher quality modeling and forecasts of the atmosphere's temporal variability, with emphasis on optical turbulence, are required. In return, military meteorologists will be given the ability to provide quantitative forecasts of HEL's maximum effective range and dwell time. This thesis will explore application of the U.S. Navy's Coupled Ocean/Atmospheric Mesoscale Prediction Systems (COAMPS) model as a means to meet this requirement and ultimately increase environmental support to the warrior.

B. FOCUS

An abundance of research has been conducted on the application of high-energy lasers (HEL) for the U.S. armed forces. In recent years, significant emphasis has been placed on the negative impacts of atmospheric turbulence

and its effects on laser-based weapons and communications systems. With key focus areas being space, air, and surface based elements, each warrants special attention when considering the source level of initial transmission, path taken, and target location. Although much of the information provided in the following sections is general enough to address the effects of turbulence in all of these elements, the direction of this study approachs the optical turbulence problem from the space-based laser perspective with emphasis on the modeling and forecasting of optical turbulence in the upper tropospheric/lower stratospheric region. This is accomplished by comparing a modified version of the COAMPS 2.0.16 mesoscale model output to thermosonde measurements taken over Vandenberg AFB during HEL test periods in October 2001 and March 2002. Specifically, turbulence parameterizations are evaluated and then adjusted for potential improvements. To better understand the complexity of the issue, a background in atmospheric turbulence and modeling is provided in the following section.

II. BACKGROUND

A. THE CHALLENGE OF MODELING

The question we must always be asking is," What is the required resolution for the given forecast?" In operational forecasting, we encounter a direct conflict between simulating atmospheric physics accurately and producing timely forecast products; this is addressed by running the numerical models at coarser resolutions, in both the vertical and horizontal, as well as focusing the model on a limited area. To adequately represent the atmosphere at scales smaller than the resolution being modeled, sub-grid physics schemes, or parameterizations, are required. When running the model over a limited area, mesoscale models become extremely sensitive to lateral boundary conditions in addition to their sensitivity to initial conditions, found in all models. Generally, initial conditions are taken from the coarser horizontal, vertical, and temporal resolutions of synoptic scale models, thus requiring interpolation into the mesoscale. With interpolation comes the potential for introducing errors at each time step that could have even greater impacts on the smaller scaled features that were parameterized. By understanding the processes, sensitivities, and tendencies of a model, these errors can be mitigated.

It is also important to note that using a model to research a phenomenon in retrospect is approached much differently than using a model to predict the same phenomenon in an operational environment. As explained by Warner *et al*. (1997), a subjective estimate of the

importance of error can be based on the degree to which the meteorology in a given case is dominated by initial conditions, local forcing and the propagation of the features outside the area of interest. When applied to a single meteorological case as is typically done in research, the estimate is based upon the prevailing meteorological condition. In an operational case, decisions are made based on the worst-case estimates encompassing an ensemble of meteorological situations.

Addressing our specific interest in optical turbulence, determining the threshold for optimum timeliness at the minimum resolution depends on accurate parameterization of the turbulent processes. Paying particularly close attention to variables within the prognostic Turbulent Kinetic Energy Equation, and their inter-relationships, will help us in this endeavor.

B. TURBULENCE

The atmosphere is a fluid in turbulent motion that continually undergoes fluctuations in density from various influences. Turbulence is, in the most general sense, random irregularities in the atmospheric flow. The major origins of these irregularities arise from: (1) mechanical mixing induced by orographic effects; (2) thermal interaction associated with the vertical currents caused by surface heating in the boundary layer; (3) thunderstorm induced vertical motions; (4) mountain waves; and (5) wind shear effects. The latter is most relevant to this paper as it specifically addresses the turbulence caused by the shearing of horizontal winds in the vertical direction

which occur along air-mass boundaries, temperature inversions, and near jet streams (Lee and Crane, 1994).

Atmospheric turbulence leads to the development of optical turbulence in the free atmosphere through the energy cascade process, optical turbulence occurring on a similar scale to clear air turbulence (CAT). Though not identical to CAT, the temperature and velocity fluctuations are so closely linked that indicators for CAT can be used to identify regions where optical turbulence would likely be found. As described by Beniston (1998), turbulent flows are always dissipative, since viscous shear stresses perform deformation work that increases the internal energy of the fluid at the expense of the kinetic energy of the turbulence. These characteristics have a profound effect on the dispersion of heat, moisture, and momentum. By definition, optical turbulence manifests itself as the temporal and spatial fluctuations of the index of refraction (n). These fluctuations can cause the HEL beam to jitter on the target as well as decrease the energy density on target.

A major source region of clear air turbulence (approximately 60%), and subsequently optical turbulence through similarity, lies on the fringes of the jet stream in the vicinity of upper level frontal zones. Here, the wind shear and thermal gradients act to produce areas conducive to the production of turbulence. These regions include (Meteorological Office College, 1996):

1. the cold side of the jet, near and below the core;
2. the warm side of the jet, above the core;

3. marked curvature and diffluent areas associated with jet exit regions;
4. the confluent and diffluent regions of two jets;
5. in the vicinity of sharp upper troughs;
6. in the vicinity of the warm side of sharp ridges;
7. where one jet undercuts another; and
8. in regions of tropopause height fluctuations.

Typical scenarios for development of turbulence also include the amplification of gravity waves as strong winds cross mountain ranges and propagate vertically. Atmospheric waves form above and downwind of the barrier in a stable environment as strong winds travel across topographic barriers. In certain thermal conditions, the resulting waves can break down into smaller scale turbulence (Ellrod, 2004). Another prolific producer of turbulence is found in the region where a cut-off low pressure systems is located to the south of a blocking high pressure cell (Rosendal, 2004). Additionally, the stably stratified conditions in the lower stratosphere can support sheets of strong optical turbulence (Mahalov and Nicolaenko, 2004).

When a HEL encounters the irregularities associated with turbulence, the optical wave fronts are subject to distortion. This distortion is the result of variations in the refractive index caused by the density fluctuation. These density fluctuations are produced by the presence of pressure and temperature gradients. The resultant density changes occur because density is proportional to the ratio of pressure and absolute temperature via the ideal gas law.

Kyle (1993) defines the index of refraction (n) for wavelength (λ), in terms of pressure (P) in millibars and temperature (T) in Kelvin, that are within or near the visible range, like those used in HEL applications, as:

$$n-1=77.6\times10^{-6}(1+\frac{7.5\times10^{-3}}{\lambda^2})\frac{P}{T} \quad . \qquad (1)$$

The effects of turbulence induced pressure variations are negligible when compared to temperature and humidity fluctuations, temperature being more important in the upper atmosphere. While considering fluctuations in the index of refraction, the wavelength can be ignored because dependence on the averaged portion of the index becomes more important (Wolfe and Zissis, 1978). Thus n fluctuations depend only on temperature so that we can express the index fluctuations with respect to temperature variations by:

$$\frac{\partial n}{\partial T}=\frac{(79\times10^{-6})P}{T^2} \quad , \qquad (2)$$

where P is the local air pressure in millibars (mb) and T is the absolute temperature in Kelvin.

By incorporating Kolmogorov's theory of turbulence (Kolmogorov, 1941), it is assumed that the kinetic energy associated with larger eddies is redistributed without loss to successively smaller eddies until ultimately being dissipated by viscosity. Furthermore, Kolmogorov determined that the structure function for temperature fluctuations obey the isotropic two-thirds power law,

$$D_T(r)=C_T^2 r^{2/3} \quad , \qquad (3)$$

where $D_T(r)$ represents the structure function, C_T^2 is the optical turbulence temperature structure parameter, and r is the separation distance between two measurements, in this case temperature, that fall between the inner and outer scales of turbulence. This leads to the proportionality relationship between the optical turbulence structure parameter as a function of the index of refraction (C_n^2) and the optical turbulence temperature structure parameter (C_T^2) given by:

$$C_n^2 = \left[\frac{(79\times10^{-6})P}{T^2}\right]^2 C_T^2 \quad . \tag{4}$$

This relationship is arrived at by applying Eq. (3) to both C_n^2 and C_T^2 where,

$$C_n^2 = \left\langle (n_1 - n_2)^2 \right\rangle \Big/ r^{2/3} \quad , \tag{5}$$

$$C_T^2 = \left\langle (T_1 - T_2)^2 \right\rangle \Big/ r^{2/3} \quad , \tag{6}$$

with $\left\langle (n_1 - n_2)^2 \right\rangle$ and $\left\langle (T_1 - T_2)^2 \right\rangle$ representing the ensemble average of the index of refraction, n_1 and n_2, and temperature, T_1 and T_2, between two points. Equations (5) and (6) can then be combined as

$$C_n^2 = \frac{\left\langle (n_1 - n_2)^2 \right\rangle}{\left\langle (T_1 - T_2)^2 \right\rangle} C_T^2 \quad . \tag{7}$$

Despite the considerable complexity in the dynamics of turbulence, equations (5) and (6) give parameters which allow us to identify it in the free atmosphere. *In situ*

measurements of C_T^2 can be made with aircraft and balloon-borne temperature sensors while C_n^2 measurements can be obtained with radar, lidar, and acoustic sounders.

C. NUMERICAL MODELING

To adequately model the dynamics and thermodynamics at the scales consistent with turbulence, the fundamental physics and mathematical laws that govern the atmosphere must be applied in a manner that will yield meaningful results while maintaining computational efficiency. In a mesoscale model, this is achieved through treating the phenomena as a parameterized sub-gridscale process. Parameterizations are used when:

- the process being considered is smaller than the characteristic grid of the model, horizontally or vertically;
- the physics describing the phenomenon would act to decrease computational efficiency if they were computed explicitly;
- or the scales of fundamental forcing related to the phenomenon are not well observed or understood.

Focusing attention on turbulent flow, its characteristic randomness makes a deterministic approach to the problem implausible; therefore, turbulence is treated with statistical methods. Fortunately, turbulent energy cascades from larger eddies to smaller eddies, allowing the turbulence-forecasting to be an achievable goal if the larger-scale numerical prediction is sufficiently accurate.

For this study, optical turbulence predictions were performed by the U.S. Navy's Coupled Ocean Atmosphere Mesoscale Prediction System (COAMPS) the U.S. Navy

mesoscale model and compared to observations at Vandenberg AFB during October 2001 and March 2002.

D. COAMPS

A detailed description of COAMPS is provided by Hodur (1997) so that only a summary of the governing equations and a brief overview of some of its numerical schemes will be provided here. COAMPS is a meso-β scale model that utilizes nonhydrostatic equations (Klemp and Wilhelmson, 1978) to predict idealized or real-data simulations. The importance of the non-hydrostatic condition is that it allows the model to deal with convection and smaller-scale topographic features so that vertical accelerations are not ignored. This is particularly important for this study since the study requires modeling at resolutions where the hydrostatic approximation breaks down and the area of interest is in the vicinity of a coastal mountain range.

COAMPS utilize the Arakawa C grid structure and has the ability to nest smaller meshes at a 3:1 ratio. Static inner grids can be arbitrarily specified within the confines of the next coarser grid. In this case, an 81 km grid spacing was defined in the outer domain with an innermost domain grid spacing of 3 km. Vertical levels are defined in the sigma-z coordinate system (Gal-Chen and Somerville, 1975). The vertical deminsion is resolved in 47 non-standard levels from sea level up to 20 km, 11 of which in the lowest 2000 m of the troposphere. The vertical resolution in the upper-troposphere and lower-stratosphere is 500 m.

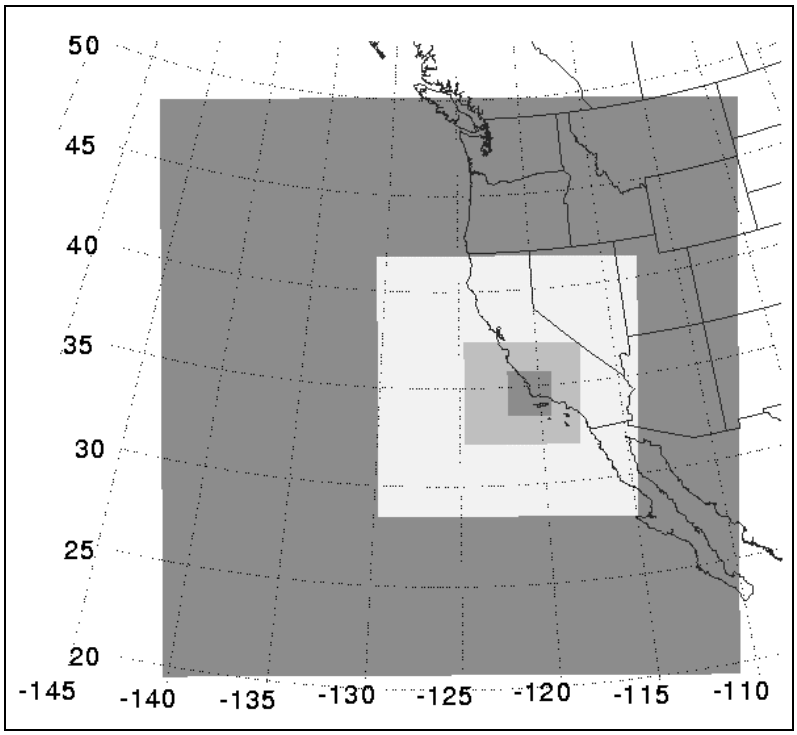

Figure 1. Orientation of COAMPS 81, 27, 9, and 3 km nested grids over Vandenberg AFB.

The model was initialized with the Nuss and Titley (1994) two-dimensional multiquadric interpolation scheme using available observations blended with NCEP's ETA 22 km horizontal resolution and 39 vertical p-levels grid fields. The verification observations were *not* included in the initialization process. All model simulations begin with a "cold" start, meaning that neither clouds nor three-dimensional mesoscale structures of wind or thermal fields, were passed on to the initialization from model first guess fields.

E. MODELING OPTICAL TURBULENCE

Since optical turbulence is not explicitly addressed within the COAMPS model physics, it must be predicted using prognostic variables from the model. As mentioned before, the full set of prognostic turbulence equations would be too costly on processing time to be viable for operational purposes. To remedy this, COAMPS incorporates Mellor and Yamada (MY) level 2.5 parameterization to estimate the vertical turbulent flux terms $\overline{u'w'}$, $\overline{v'w'}$, and $\overline{\theta'w'}$ as explained in Mellor (1973), Mellor and Yamada (1974), and Mellor and Yamada (1982). Even though calculations for the required prognostic variables are directly affected by closing the set of prognostic turbulence equations with parameterization, it is a computational necessity. In this parameterization the horizontal wind components (U,V) and potential temperature (Θ) define the vertical turbulent fluxes as,

$$\overline{u'w'} = -K_m \frac{\partial U}{\partial z}, \tag{8}$$

$$\overline{v'w'} = -K_m \frac{\partial V}{\partial z}, \tag{9}$$

$$\overline{\theta'w'} = -K_h \frac{\partial \Theta}{\partial z}, \tag{10}$$

where both,

$$K_m = S_m L E^{1/2}, \tag{11}$$

and

$$K_h = S_h L E^{1/2}, \tag{12}$$

define the turbulent momentum and thermal diffusivities, respectively. L is a mixing length scale and E is the turbulent kinetic energy (TKE) such that,

$$E = \frac{1}{2}\left(u'^2 + v'^2 + w'^2\right). \tag{13}$$

Mellor and Yamada define S_m as the momentum stability function and S_h as the heat stability function. Both are functions of gradient Richardson number,

$$R_i = \frac{\left(\frac{g}{\theta_v}\left(\frac{\partial \theta_v}{\partial z}\right)\right)}{\left(\left(\frac{\partial u}{\partial z}\right)^2 + \left(\frac{\partial v}{\partial z}\right)^2\right)}. \tag{14}$$

The gradient Richardson number represents the ratio of the energy extracted by buoyancy forces to the energy gained from the shear forces, giving quantitative information on the relation between the stabilizing effect of buoyancy and the destabilizing effect of velocity shear. Once the ratio exceeds a critical threshold of 0.25, turbulence can no longer be generated. This particular study will focus on examining stable atmospheric conditions.

Given the proportional relationship between the optical turbulence parameter (C_n^2) and thermal structure parameter (C_T^2) seen in (3), the problem can be approached by solving for C_T^2. In a stable atmosphere where C_T^2 depends on the atmospheric stratification, the thermal structure parameter can be expressed in terms of the bulk potential temperature (θ) as explained by Bougeault *et al*.

(1995). The resultant C_T^2 in terms of the mechanical mixing length scale (L_m) and the dissipation length scale (L_ε) is

$$C_T^2 = 1.4 L_m L_\varepsilon^{1/3} \left(\frac{\partial \theta}{\partial z} \right)^2 . \quad (15)$$

This was further simplified in Walters and Miller (1999) in terms of a special mixing length scale (L_o) so that

$$C_T^2 = 2.8 L_o^{4/3} \left(\frac{\partial \theta}{\partial z} \right)^2 . \quad (16)$$

To date, the TKE and TKE-Free Methods show great potential for aiding us in the forecasting of optical turbulence. The TKE Method, as described in Walters and Miller (1999), will be examined in this thesis. This method uses three-dimensional predictions of potential temperature and turbulent kinetic energy, one of the prognostic variables affected by the Mellor and Yamada (MY) parameterization scheme. The TKE-Free Method, which is important to mention for future investigation, uses predictions of potential temperature and winds. Each method calculates L_o in a different manner, as explained below.

1. TKE Method

To achieve realistic turbulent kinetic energies and temperature fluctuations in the stable atmosphere an appropriate thermal to eddy diffusivity (K_h/K_m) dependence must be incorporated into the turbulent kinetic energy tendency equation. Although the default MY eddy

diffusivity parameterization attempts to meet this requirement, known deficiencies exist and are addressed later in this section. The COAMPS prognostic equation for TKE (Hodur 1997) is

$$\frac{\partial E}{\partial t} = -u\frac{\partial E}{\partial x} - v\frac{\partial E}{\partial y} - w\frac{\partial E}{\partial z} + K_m\left[\left(\frac{\partial u}{\partial z}\right)^2 + \left(\frac{\partial v}{\partial z}\right)^2\right] - K_h\frac{g}{\theta}\frac{\partial \theta}{\partial z} + D_e + K_b\nabla^4 E - \varepsilon. \quad (17)$$

(a) (b) (c) (d) (e) (f)

Components of (17) are:

(a) three-dimensional advection;

(b) shear production;

(c) buoyancy production;

(d) sub-grid scale mixing;

(d) numerical diffusion;

(e) and dissipation.

The thermal mixing length applied in the TKE Method uses the Deardorff (1980) definition where

$$L_o = 0.76\sqrt{\frac{E}{\frac{g}{\theta}\left(\frac{\partial \theta}{\partial z}\right)}}. \quad (18)$$

With regards to eddy diffusivity parameterization, Walters (1995) and Walters and Bradford (1997) noted that when comparing observed optical turbulence TKE profiles with modeled TKE values, more realistic results where achieved by using the Kondo *et al*. (1978) polynomial,

$$\frac{K_h}{K_m} = \frac{a_1}{a_2 R_i + \dfrac{1}{1 + a_2 R_i}}. \qquad (19)$$

Miller *et al.* (2001) showed that the simulated turbulent processes are quite sensitive to the K_h/K_m vs. R_i relationship. Generally, too aggressive of a parameterization can exaggerate the turbulent processes while a too conservative approach can dampen it out completely.

2. TKE-Free Method

This method represents a lower order closure of the vertical turbulent fluxes compared to the TKE Method and, as stated before, uses predictions of potential temperature and winds. It estimates the mixing length scale required in Eq. (16) based on observations presented by Tjernstrom (1993) so that

$$L_o = \frac{23}{\left(1 + 15 R_i \sqrt{1 + 5 R_i}\right)^{1/2}}, \qquad (20)$$

where R_i is defined in Eq. (14).

III. ORGANIZATIONAL APPROACH

Initially, a synoptic re-analysis of the Eastern Pacific is provided for both the October 2001 and March 2002. Emphasis will be placed on those synoptic scale features that would most likely produce optical turbulence over the area of interest, Vandenberg AFB.

To gauge of the model's initial performance, COAMPS's horizontal model output will be directly compared to the synoptic analysis from National Centers for Environmental Prediction/Marine Prediction Center (NCEP/MPC) at 00Z and 12Z, or closest available analysis if those times were not available. This will validate the model's accuracy and expose inconsistencies that may have been inherited by errors in lateral boundary conditions or by poor initialization. Additionally, rawinsonde data will be used to compare vertical depictions of the model output at the closest relevant grid-point. These steps will reveal inconsistencies that may be present in the column above the point of interest. Next, the TKE Method will be applied to 3 km COAMPS runs of the October 2001 case to produce synthetic vertical profiles. This will be accomplished by creating a synthetic balloon launch within the model to produce a trajectory comparable to that of an actual profile. These profiles will in turn be compared to corresponding "real world" balloon launched thermosonde data and qualitatively analyzed in detail. Additionally, these results will be quantitatively compared by determining the isoplanatic angle, defined in CH. V Sec. C., for each sonde to produce a scatter plot. Results will subsequently be used to make adjustments to measure

the improvement of new parameterizations in outlying model runs selected from the October 2001 and March 2002 cases. The "Default" and "Adjusted" COAMPS model runs for October 2001 and March 2002 will then be quantitatively compared to thermosonde data in the same manner as described for the October 2001 case.

IV. SYNOPTIC ANALYSIS

A. OCTOBER 2001

For this period of study, the synoptic conditions for October 18th through 25th are derived from the National Climatic Data Center's (NCDC) surface analysis, supplemented by Unysis composite GOES infrared satellite imagery and 300 mb AVN jet level wind analysis from San Francisco State University Meteorology Department. Conditions conducive to the production of optical turbulence will be highlighted to help focus mesoscale analysis on those periods likely to have affected the experiment over Vandenberg AFB. Relevant charts and imagery will be shown in the following synoptic summary while the complete compliment of charts are located in Appendix A with satellite imagery in Appendix B.

Beginning on October 18th, the synoptic picture is dominated surface high-pressure system about 800 nautical miles (nm) west of Oregon as can be seen in Figure 2. This persistent high remains a synoptic forcing feature throughout the period. A semi-permanent thermal low in southern California is present in the beginning of the period with an associated inverted trough extending up though the California Central Valley, affecting weather over the area of interest. The 300 mb jet level winds, as depicted in the AVN analysis in Figure 3, show the Polar Front Jet (PFJ) north of the surface high arcing from the Gulf of Alaska into British Columbia.

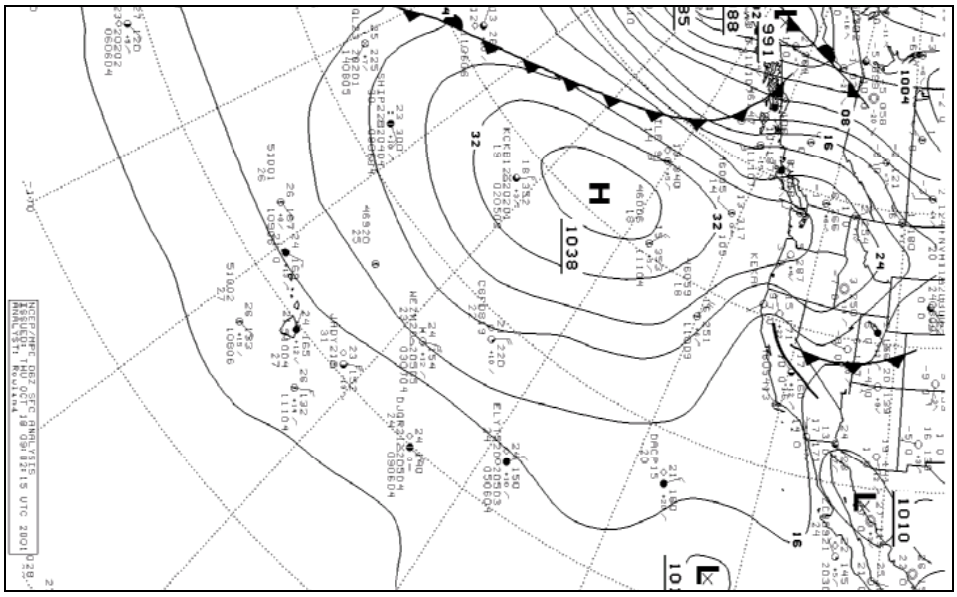

Figure 2. NCEP/MPC 06Z Surface Analysis, 18OOCT01.

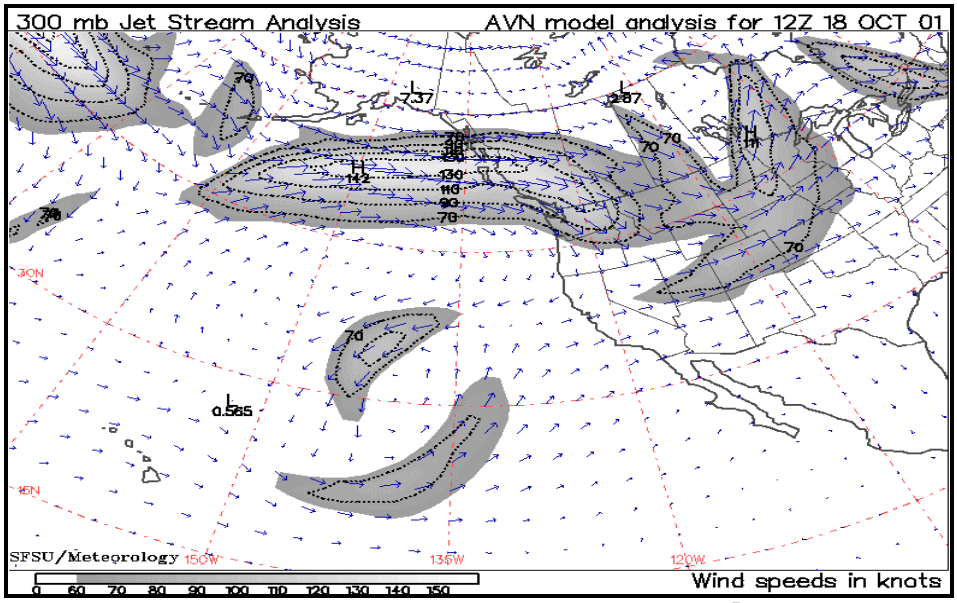

Figure 3. AVN 12Z 300mb Jet Stream Analysis, 18OCT01.

By 12Z on the 18th, a cyclonic circulation off the coast of California, indicative of an upper level cut-off low, becomes apparent in the jet level winds depicted in the 300 mb AVN analysis. Satellite imagery from the GOES composite indicates that a well-developed circulation had developed from 12Z on the 18th to 00Z on the 19th with

high-level clouds exhibiting the characteristic 'comma' signature associated with cyclonic circulation (Figure 4). On the surface analysis, this upper level feature is manifested as a stationary trough (Figure 5).

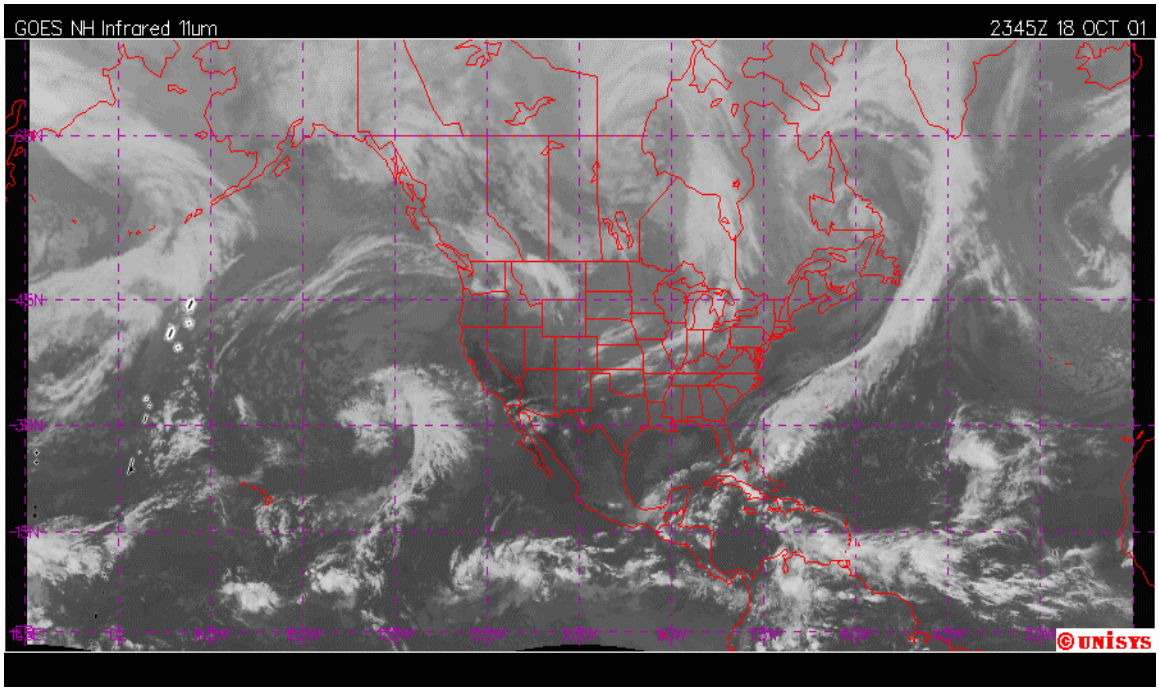

Figure 4. GOES 00Z Composite IR, 19OCT01.

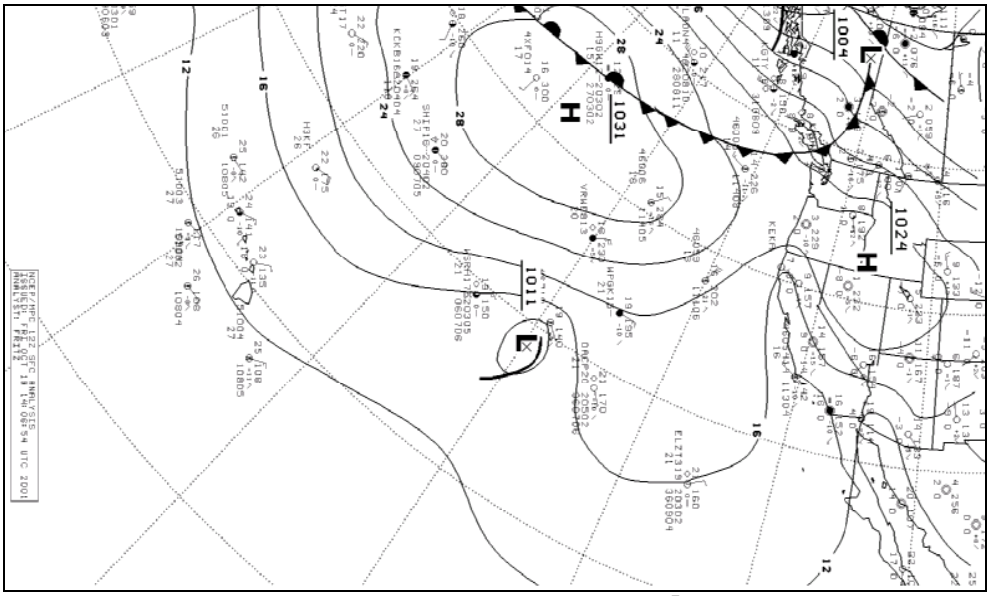

Figure 5. NCEP/MPC 12Z Surface Analysis, 19OCT01.

As the Northeast Pacific High begins to weaken slightly on the 19th, the 300 mb winds on the southeast quadrant of the cut-off low begin to intensify. This intensification is the result of two different processes contributing to its development. First, cold air advected by the Northeast Pacific high is being wrapped up below the upper-level cutoff low, helping to deepen it. Second, interaction with the Subtropical Jet (STJ) produces speed convergence along the southern edge of the cut-off low. These two interactions cause a jet maximum to form near 30 N 135 W. By the 21st, the jet extends to the central coast of California and begins to propagate eastward as the Northeast Pacific high starts rebuilding. The jet edge is clearly visible crossing central California on the Figure 6 satellite image.

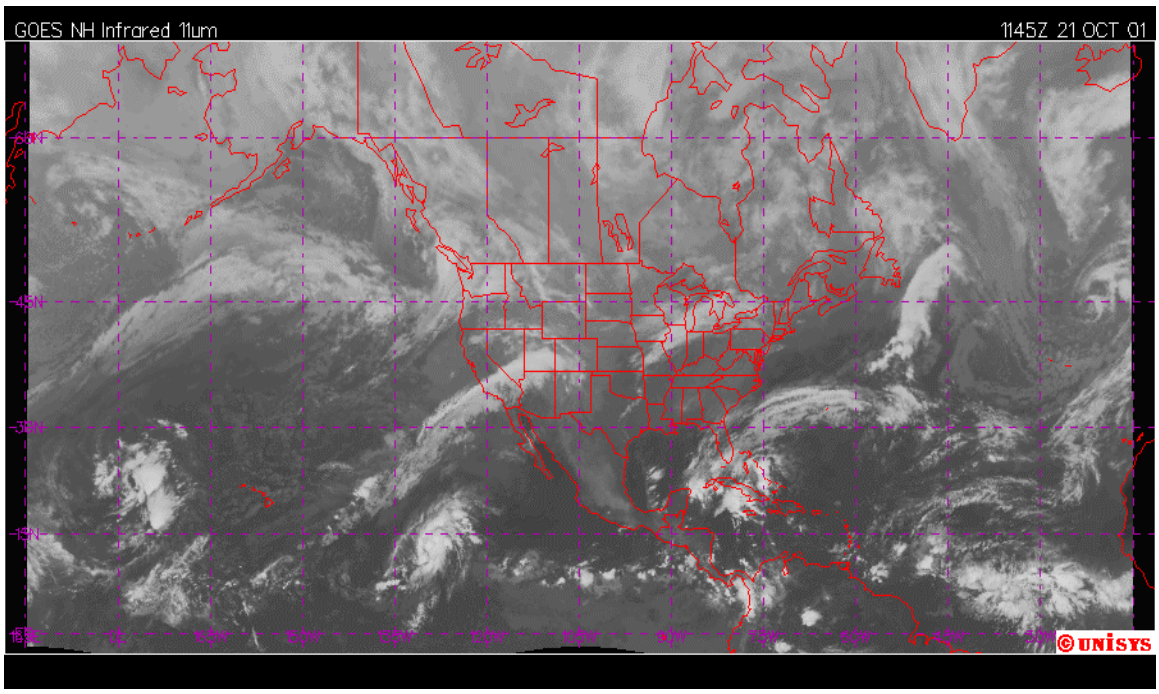

Figure 6. GOES 12Z Composite IR, 21OCT01.

Continuing through the period, the jet max moves eastward until it merges with the PFJ on the 23rd. At the

end of the period, the northeast Pacific high moves southwest of its original position from the 18th and reestablishes itself as the dominant weather influence over the California coast. The PFJ has similarly reoriented itself northwesterly across Oregon and Washington state.

This STJ core is of particular interest because it is expected to be a prolific producer of turbulence in the upper levels over our area of interest. Similarly, since the beginning of the period was not affected by a strong turbulence producing feature, this event should provide a an opportunity to test the forecast capability, both strengths and weaknesses, of mesoscale COAMPS analysis.

B. MARCH 2002

This second period covers synoptic features over the Eastern Pacific from March 1st through 7th, 2002. Surface analysis charts used in this review are the eastern segment of NCEP's Pacific surface analysis. Both NCEP analysis and infrared 4 km GOES satellite half disk imagery were obtained from archives of the Naval Postgraduate School (NPS) Meteorology Department. Jet level winds were taken from the 300 mb AVN analysis archived by San Francisco State University Meteorology Department.

On March 1, the surface analysis shows a high-pressure system just west of the Washington coast and a stationary trough between Hawaii and California. Over southern California, a stationary low is anchoring an inverted trough that extends to the north (Figure 7). This surface pattern persists until March 4th.

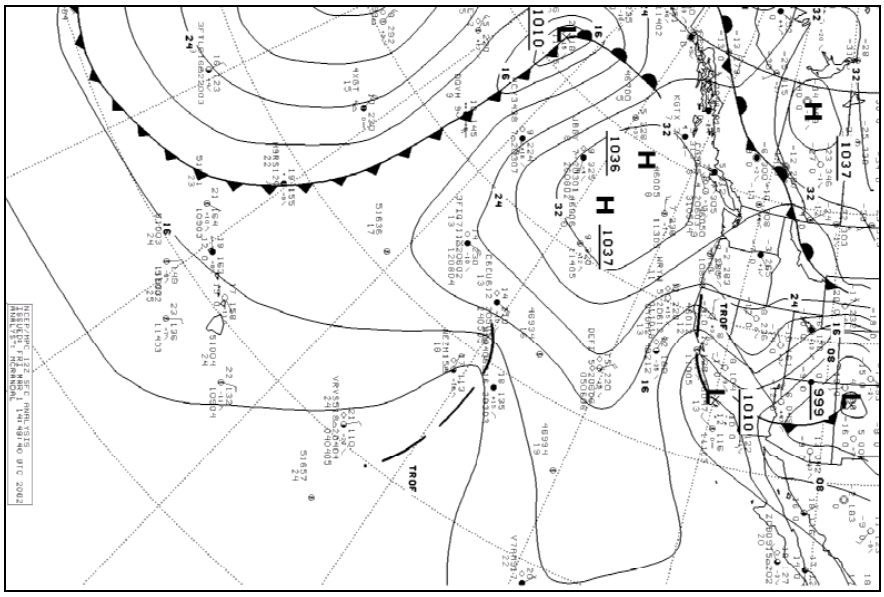

Figure 7. NCEP/MPC 12Z Surface Analysis, 01MAR02.

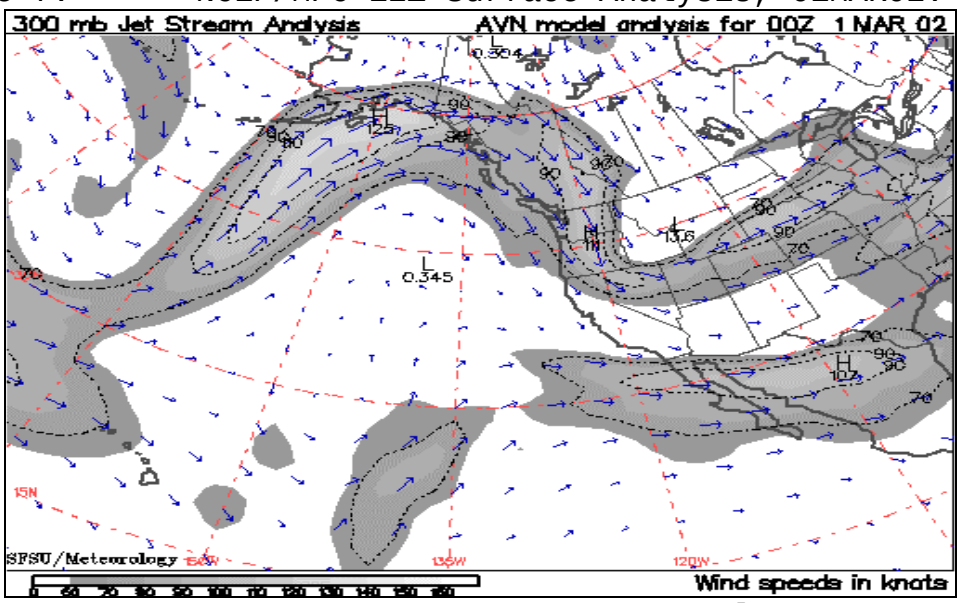

Figure 8. AVN 12Z 300mb Jet Stream Analysis, 01MAR02.

Aloft, Figure 8 shows that the PFJ is highly meridional, becoming northerly over Washington and Oregon before deviating sharply to the East over northern California. The STJ is zonal along the Baja Peninsula and northern Mexico. Continuing through the period, the PFJ extends further south along the California coast, eventually merging with the STJ on the 2nd, then becoming

southwesterly over the middle of the United States (Figure 9). IR satellite imagery depicts this feature with clear skies to the north of the jet and scattered cloudiness on the warm side (Figure 10), as seen in imagery from the 3rd to the 5th.

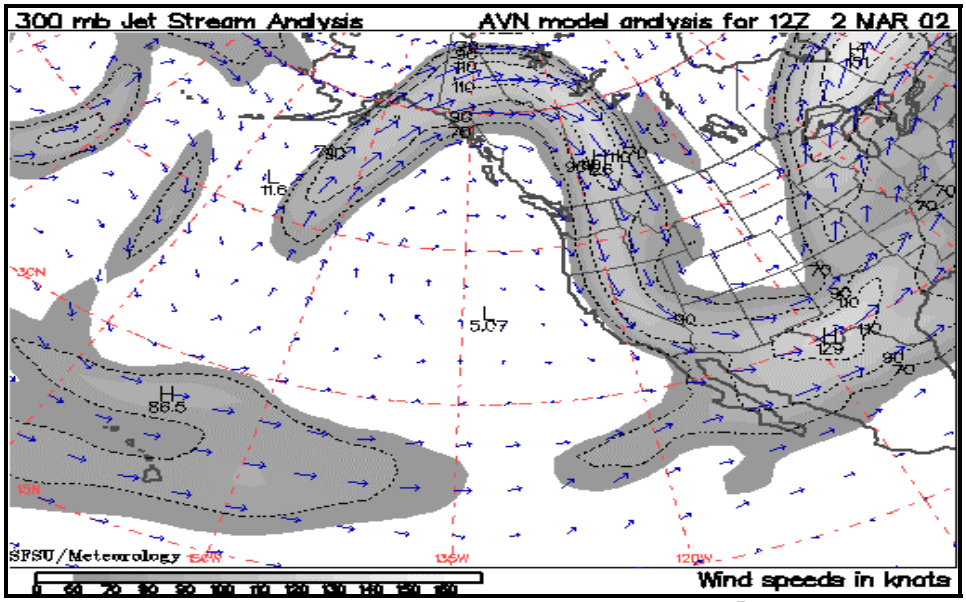

Figure 9. AVN 12Z 300mb Jet Stream Analysis, 02MAR02.

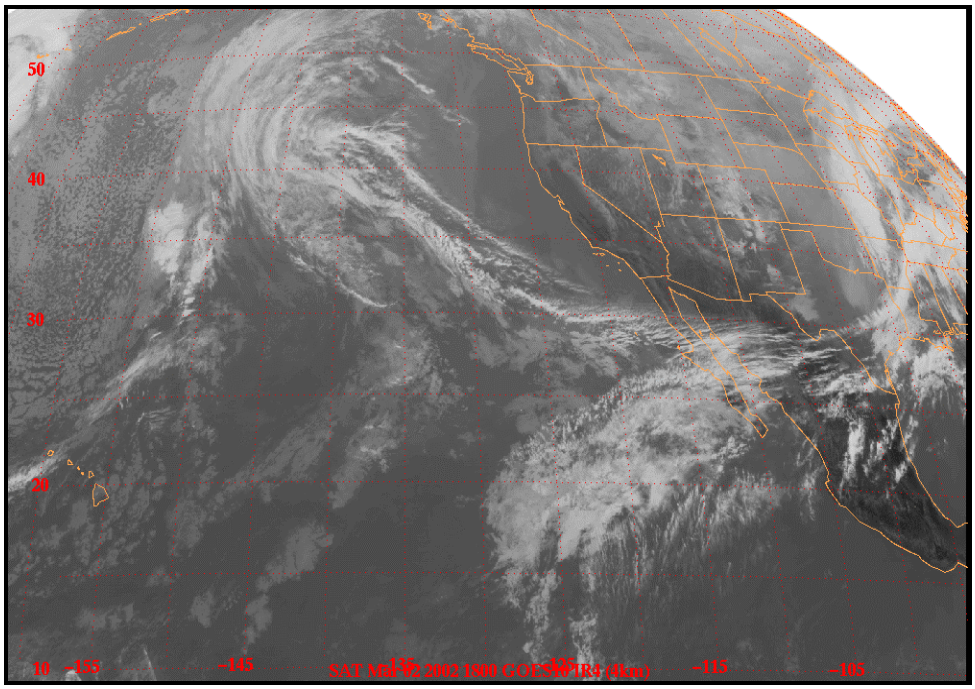

Figure 10. GOES WEST 18Z IR, 02MAR02.

On the 4th of March, the pattern begins to change as a short wave interacts with the stationary trough that was located near 140W, resulting in development of the low and frontogenesis. This new baroclinic system with its associated fronts begins tracking northeast. Due to interaction with the STJ, a jet maxima forms in the southeastern quadrant of the cyclonic circulation as it intensifies, extending the jet northeastward as with the frontal system propagates (Figure 11). This elongation of the jet continues until it crosses the California coast on 5th and persists until mid-period (12Z) on the 7th.

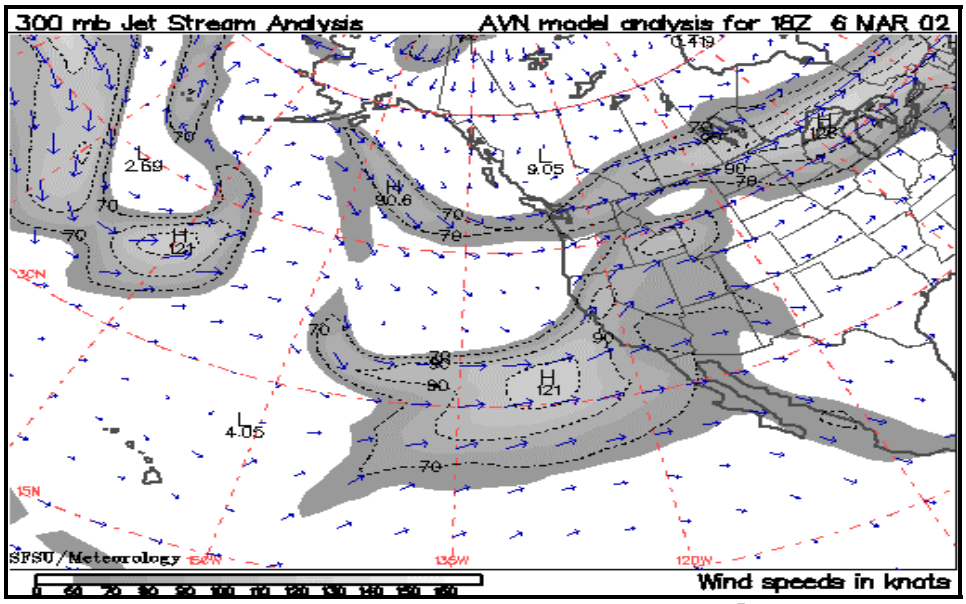

Figure 11. AVN 18Z 300mb Jet Stream Analysis, 06MAR02.

The STJ interacts with the PFJ on the 8th and the two jets again combine to form a 300 mb trough that quickly propagates eastward, setting the stage for another low-pressure system to move into the California coast mid-period on the 9th.

In summary, the PFJ placement on the 1st and 2nd of March are expected to produce optical turbulence aloft. From the 3rd to late on the 5th, conditions aloft are less conducive to produce extreme gradients in the index of refraction. During the second half of the study, when the STJ crosses the West Coast, we would once again expect higher values of optical turbulence, including the interaction that takes place between the PFJ and STJ on the 8th.

THIS PAGE INTENTIONALLY LEFT BLANK

V. MODEL ANALYSIS

A. COAMPS ANALYSIS

1. Surface Analysis

The first analysis that was performed compared the NCEP Pacific 00Z and 12Z Analysis with the corresponding COAMPS 81 km resolution model runs to ensure that the model was depicting the synoptic situation with reasonable accuracy. Furthermore, both the previous 12 hour forecast and the 00Z model analysis valid for the particular NCEP surface analysis were compared and contrasted against one another. This was done to investigate if poor turbulence forecast could be traced to poor initialization of the synoptic conditions.

As can be seen when comparing Figure 12 with Figures 13 and 14, the synoptic NCEP analysis and model runs match relatively well considering the low resolution depicted. This example also shows artifacts that are common considering the forecast time. Specifically, it can be seen in Figure 13 that the 12-hour forecast shows increased detail in isobar structure but tends to make the high-pressure center slightly higher than the NCEP analysis. Also commonly encountered as the forecast progresses, distortion of isobaric gradients becomes more clearly visible near the lateral boundaries of the model. The 00Z model analysis typically depicts the high-pressure system in the Northeast Pacific similar to the NCEP analysis with isobars that more relaxed when directly compared to the prior run’s 12-hour forecast. Additionally, lateral boundaries for this run haven’t distorted the isobaric

pattern as seen in the 12-hour forecast. Also significant is that the surface trough at 140W is wising in the 12 hour forecast.

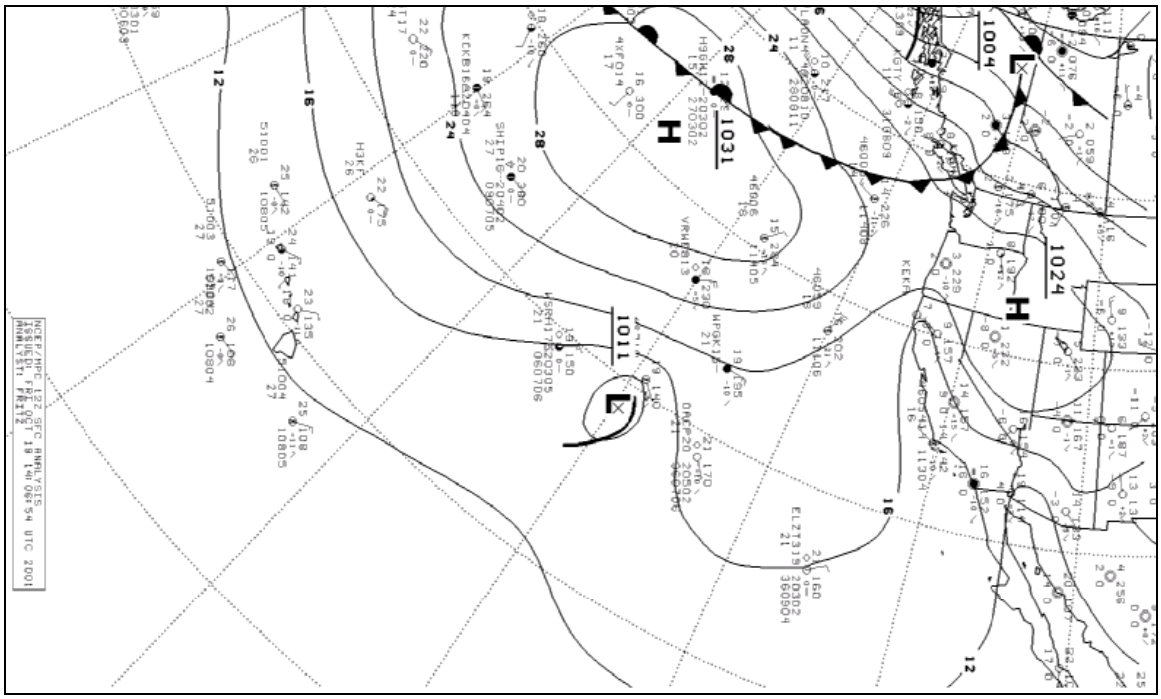

Figure 12. NCEP/MPC Surface Analysis, 12Z 19OCT01.

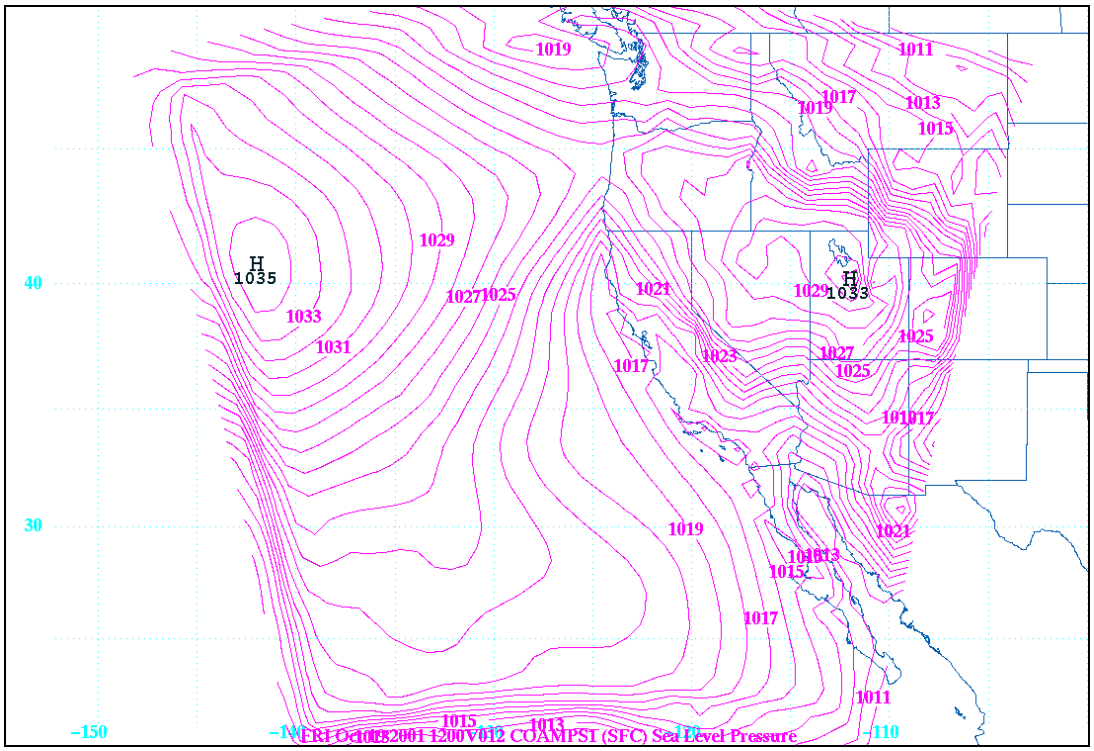

Figure 13. COAMPS 12h forecast for 81 km 12Z, 19OCT01.

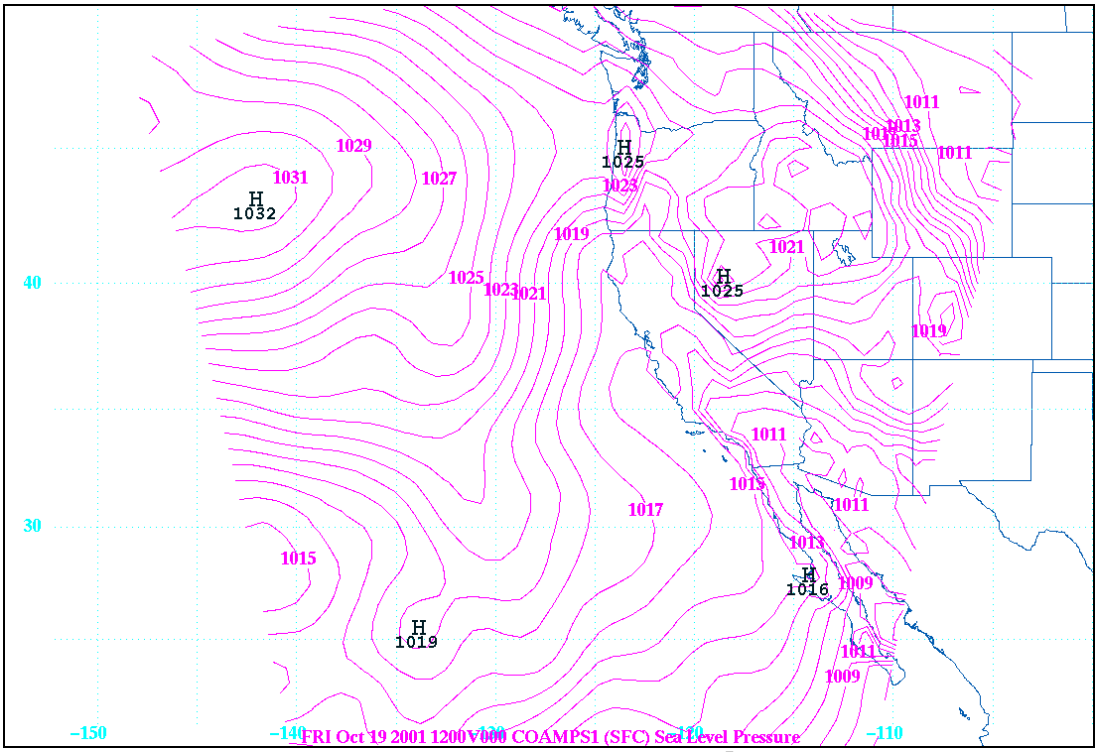

Figure 14. COAMPS 81 km Surface Analysis for 12Z, 19OCT01.

A similar review of COAMPS analysis and 12 Hour forecasts showed satisfactory agreement depicting the synoptic situation from the 19th to the 25th of October. The sea level pressures were within 5 millibars at the high/low pressure centers. The complete set of 81 km COAMPS runs for this time period are provided in Appendix C.

2. Jet Analysis

Jet stream analysis was performed by comparing the AVN 300 mb model analysis with COAMPS's previous 12-hour forecast and the 00Z analysis using isotachs and winds at the 300 mb level. This was conducted in the same manner as the surface analysis just discussed. Figures 15, 16 and 17 show the typical scheme used for this comparison.

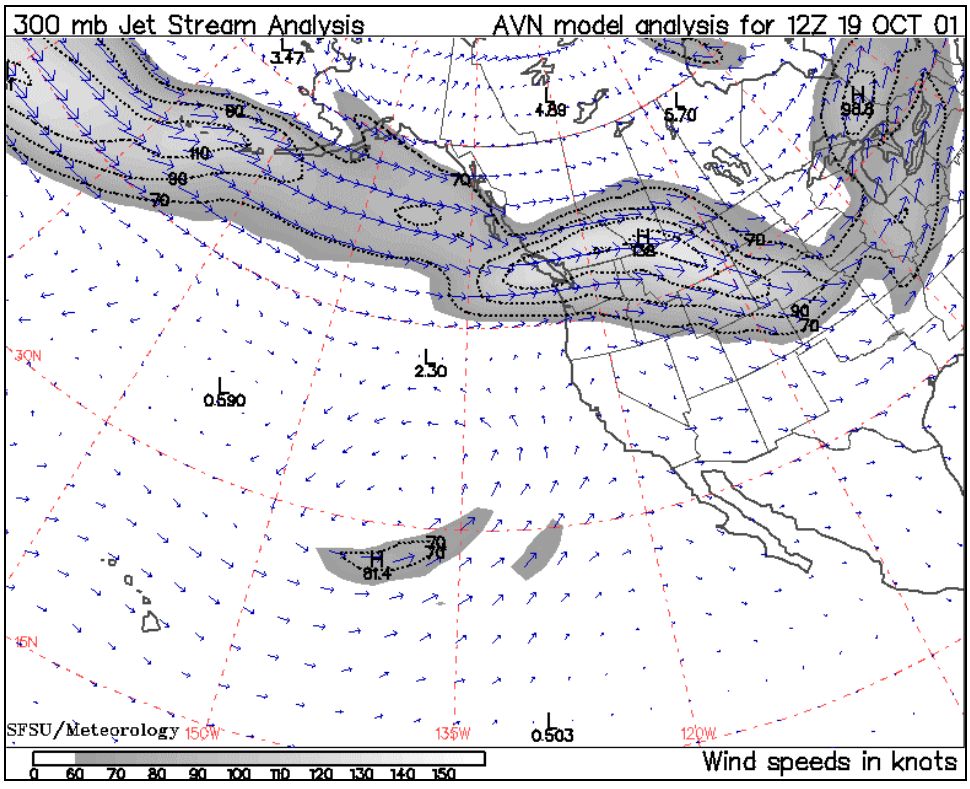

Figure 15. AVN Jet Stream Analysis 12Z,19OCT01.

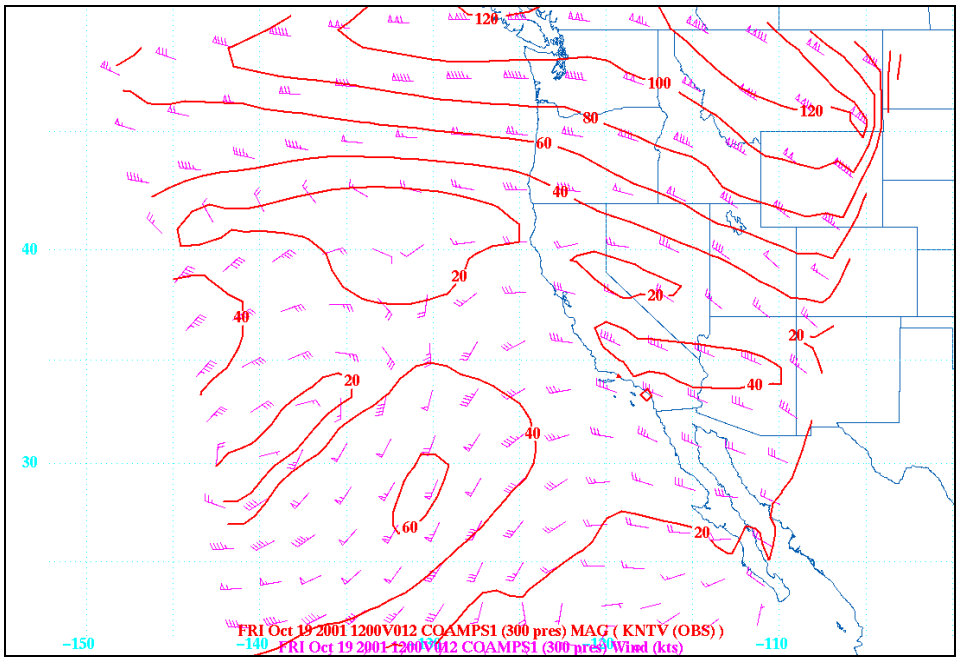

Figure 16. COAMPS 12h forecast for 300mb 12Z, 19OCT01.

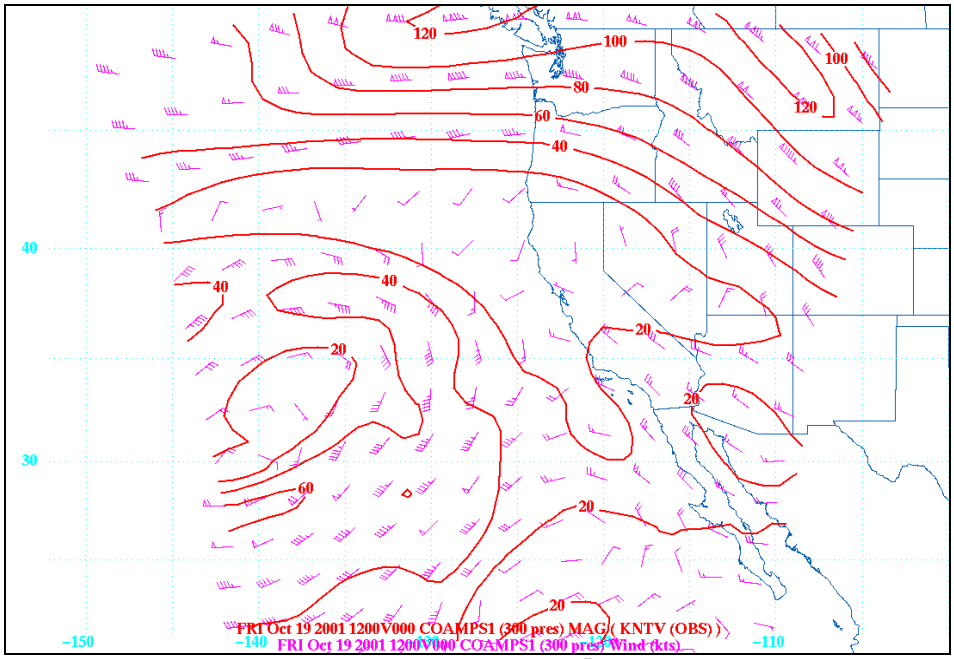

Figure 17. COAMPS 300mb 12Z Analysis, 19OCT01.

Attention was directed to the position of the jet stream, orientation, and the maximum speeds occurring within the lateral boundaries of the model in relation to the maximum speeds and wind directions taken from the AVN 300 mb analysis.

Typically, the position of the jet maxima in the 12-hour forecasts were slightly behind, or more westerly in position, to that of the AVN analysis while the analysis typically had better position, as should be expected. Aside from the slight differences in position, the COAMPS runs were depicting the 300 mb jets reasonably. Applicable AVN analysis are located in Appendix D while the full set of COAMPS 300 mb forecast and analysis are located in Appendix E.

Since the focus of this study delves into the ability to forecast turbulence in the mesoscale, particular attention was given to the times surrounding the 21OCT01 12Z analysis over Vandenberg AFB, shown in Figure 18. On this date, an extension of the Sub-Tropical Jet, a prolific producer of turbulence, was affecting the nested area of interest.

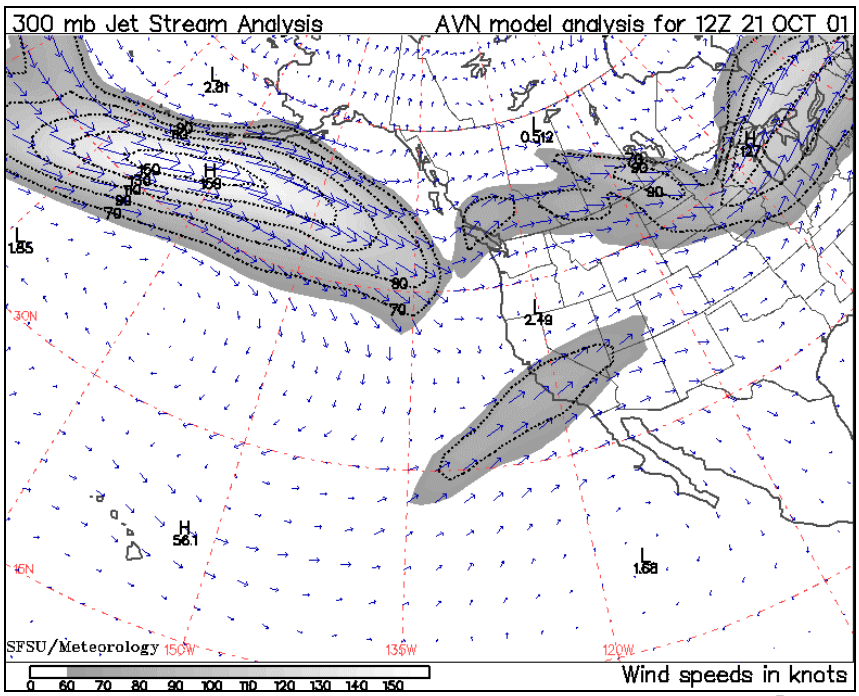

Figure 18. AVN 12Z 21OCT01 Jet Stream Analysis.

3. COAMPS Skew-T Comparison with Rawinsondes

Satisfied that the COAMPS model was correctly depicting the synoptic scale thus far, the next logical step was to verify the mesoscale. This was achieved by directly comparing balloon-launched rawinsonde measurements in the skew-T format with synthetically produced profiles for the same area, Vandenberg AFB, using COAMPS forecast from the 3 km domain. Although not as detailed as a thermosonde/model comparison to come, this step provide a more general indication of whether the model is providing reasonable output.

Table 1 shows the balloon launched that was compared to a particular model run. The 00Z 19OCT01 balloon launch was unavailable so, the earlier launch (18Z 18OCT01) was used. Equally important to mention, COAMPS runs for 21OCT01 12Z and 22OCT01 00Z valid times where not initiated due to thermosonde failure.

Balloon ttZ ddmmmyy	Model dd ttZvtt
18Z 18OCT01	18 12Zv12
00Z 20OCT01	19 12Zv12
00Z 21OCT01	20 12Zv12
00Z 23OCT01	22 12Zv12
00Z 24OCT01	23 12Zv12
00Z 25OCT01	24 12Zv12

Table 1. Balloon launch times and the COAMPS forecast.

In all cases, the 12-hour forecast from the model was used for the comparison. The reasons for using the 12-hour forecast instead of the 00Z model analysis was; 1) model instability for the first six hours after

initialization, and 2) a consistent surface temperature discrepancy apparent in the 00Z analysis. Figure 19 shows a typical comparison of forecast with the analysis from the same valid times to demonstrate this point. As can be seen, the surface temperature in the analysis is 10 degrees Celsius greater than, more in some cases, the surface temperature reflected in the balloon launched data. Although an interesting anomaly, because this takes place during a time of expected instability, this observation does not interfere with the focus of this study, forecasting turbulence above the boundary layer.

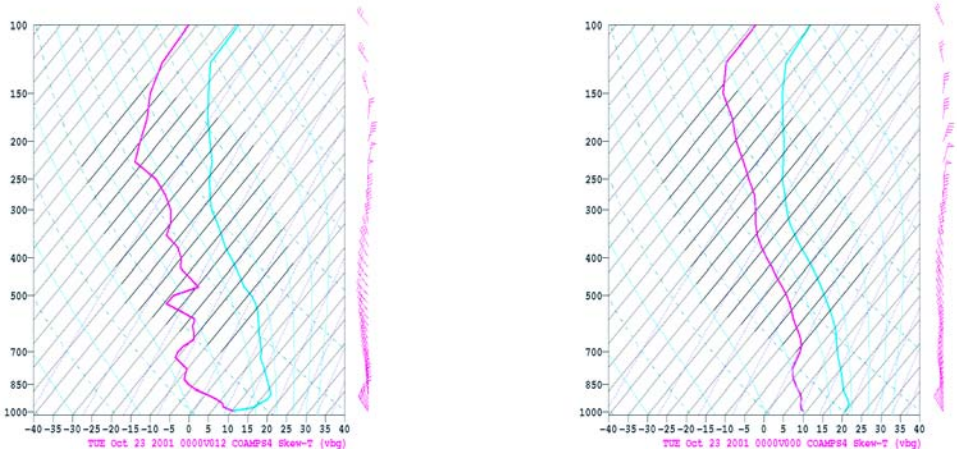

Figure 19. 22OCT01 12Zv12 COAMPS forecast(left) and the 23OCT01 00Zv00 COAMPS analysis (right).

Figures 20 and 21 show a typical comparison between balloon-derived skew-T with the corresponding forecast. Overall, balloon-launched sonde comparisons to COAMPS's vertical model where reasonable with the following discrepancies noted:

1. The 20OCT01 12Z model run (Figure 152), 12 hour forecast, showed a marked departure from the corresponding balloon-sonde (00Z 21OCT01) at the 500

mb level, Figure 136. Although the actual conditions seem to indicate a drying at this level, the model's dry layer is clearly excessive.

2. The 22OCT01 12z model run's 12 hour forecast (Figure 155), indicated a dryer column with consistently lower dew point temperatures than that indicated by the 00Z 23OCT01 balloon, Figure 140.

3. The 23OCT01 12Z model run's 12 forecast (Figure 158) shows a stronger inversion with less moisture from 800 mb to 300 mb when compared to the 00Z 24OCT01 balloon profile, Figure 142. Additionally, stronger and more northerly winds are indicated around the 250 mb level in the model.

Archived Sounding data from the University of Wyoming is located in Appendix F with corresponding COAMPS vertical profiles taken from the 3 km nest located in Appendix G.

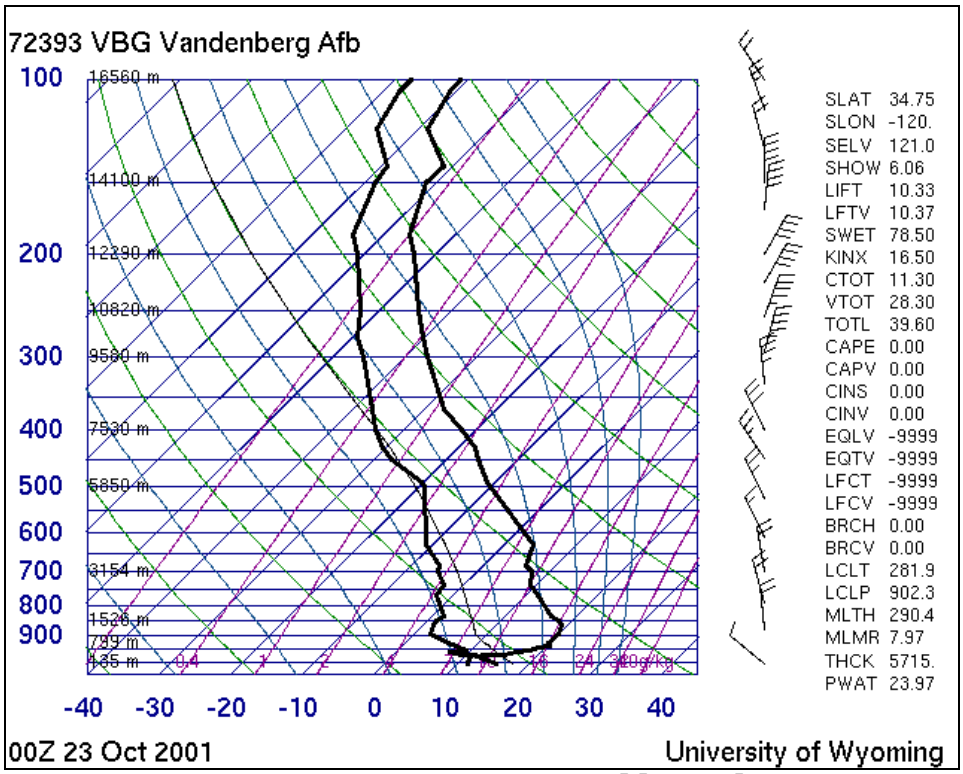

Figure 20. Skew-T derived from balloon launched data, 00Z 23OCT01.

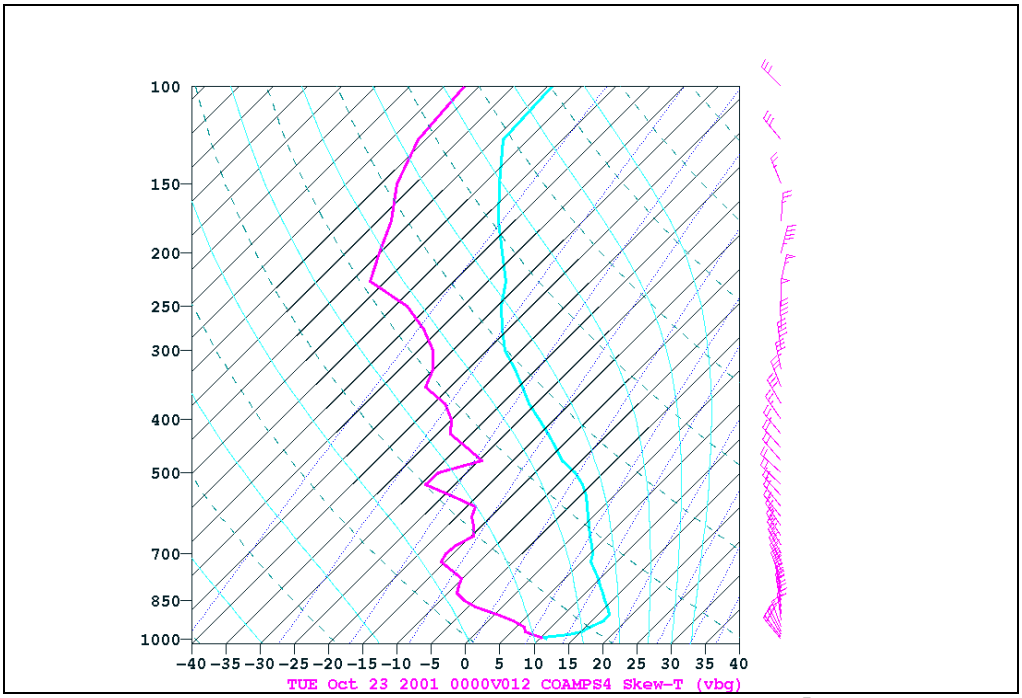

Figure 21. Skew-T derived from COAMPS, valid 00Z 23OCT01.

4. COAMPS Skew-T Comparison with Thermosonde Data

Similar to the analysis performed in Section 3, this step served as verification that the model was depicting the environment well in a relative sense. A thermosonde is a balloon-launched sensor that measures temperature differences of less than one percent of a degree centigrade between two locations in the atmosphere. Thus, the thermosonde measurements represent extremely high resolutions (up to 350 data points per kilometer) in the vertical while the model depiction is coarse (one point per 500m in the upper troposphere, 47 points throughout the column). It is also reasonable to expect that sondes launched on the same day should show similar structure since they are launched only hours apart.

To reiterate an earlier point, finding the balance between resolution, computational cost, and timeliness of the product is key to operational viability. Since this step simply served as verification, details will be explored in the next section. Table 2 shows a list of the thermosonde, launch times, and the applicable COAMPS run that were compared. The full set of thermosonde profiles are included in Appendix H.

Thermosonde	Launch time (UT)	Model time (UT)
Thermosonde 2	19OCT01 0132	18OCT01 12Zv14
Thermosonde 3	19OCT01 0322	18OCT01 12Zv16
Thermosonde 5	20OCT01 0115	19OCT01 12Zv14
Thermosonde 6	20OCT01 0300	19OCT01 12Zv16
Thermosonde 7	20OCT01 0444	19OCT01 12Zv17
Thermosonde 10	21OCT01 0235	20OCT01 12Zv14
Thermosonde 11	21OCT01 0413	20OCT01 12Zv16
Thermosonde 12	23OCT01 0115	22OCT01 12Zv14
Thermosonde 13	23OCT01 0254	22OCT01 12Zv16
Thermosonde 15	24OCT01 0114	23OCT01 12Zv14
Thermosonde 16	24OCT01 0248	23OCT01 12Zv14
Thermosonde 17	24OCT01 0430	23OCT01 12Zv16
Thermosonde 18	25OCT01 0115	24OCT01 12Zv14
Thermosonde 19	25OCT01 0253	24OCT01 12Zv16
Thermosonde 21	26OCT01 0249	25OCT01 12Zv14
Thermosonde 22	26OCT01 0423	25OCT01 12Zv16

Table 2. Thermosonde and corresponding model run times.

B. QUALITATIVE EVALUATION OF C_n^2 PROFILES DERIVED FROM THERMOSONDE AND COAMPS DATA

This analysis was performed by overlaying C_n^2 results from both the thermosonde data and the corresponding COAMPS model forecast. Since the thermosonde data was at a much higher resolution, as demonstrated in Figure 22, the C_n^2 values were averaged over 50 data points, roughly 400 m, to reduce noise while maintaining the optical turbulence trend for comparison, as shown in Figure 23.

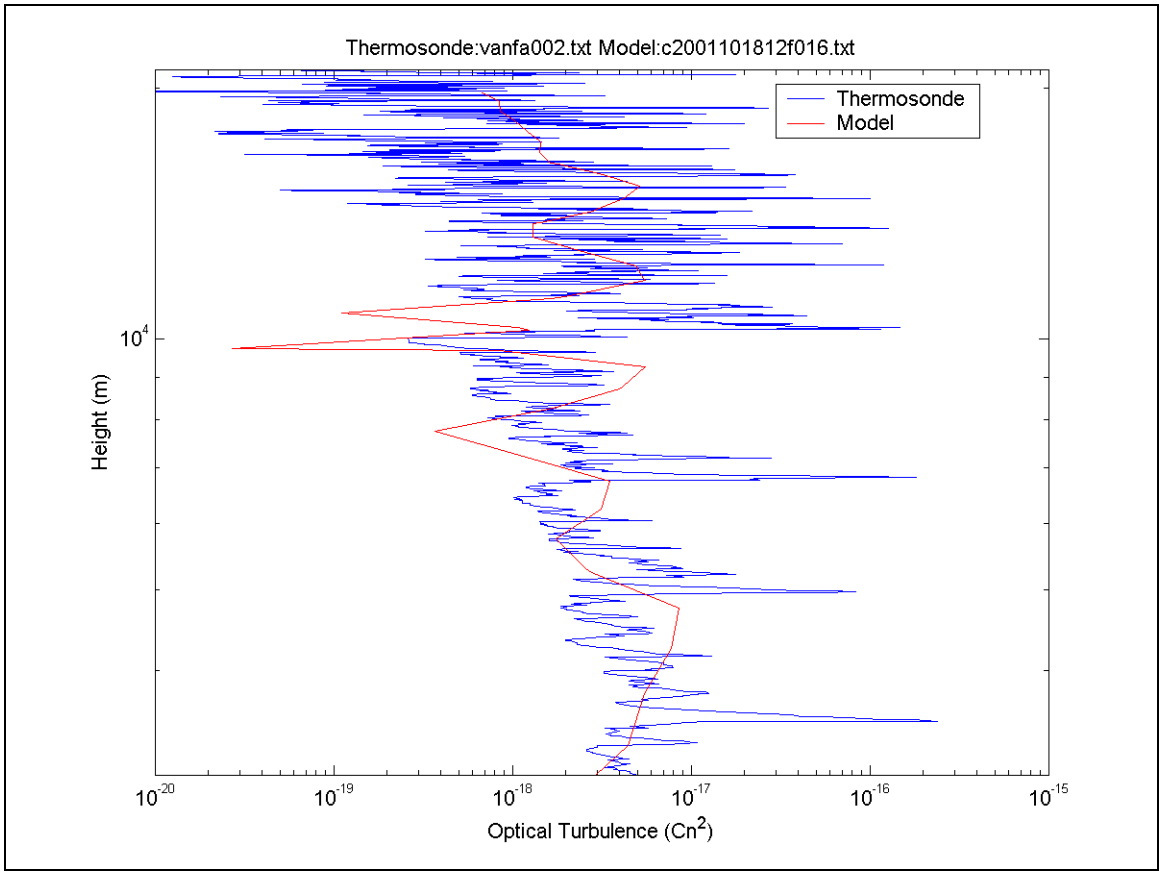

Figure 22. Comparison with full thermosonde data.

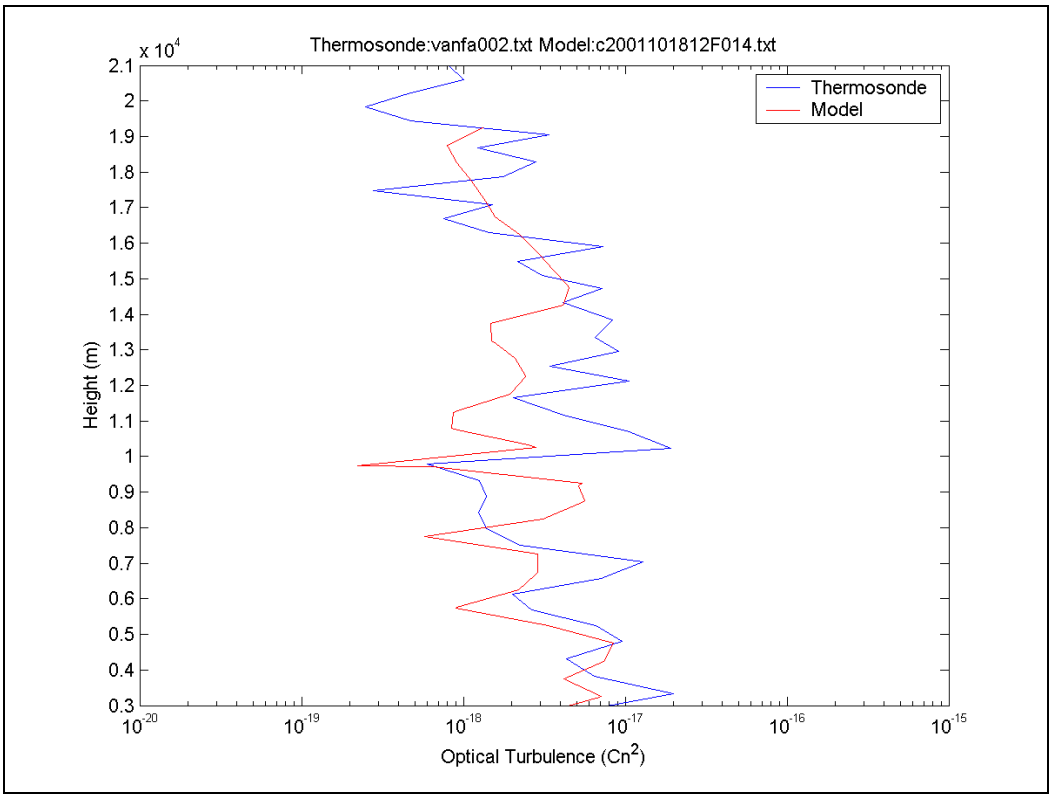

Figure 23. Thermosonde data averaged over 50 points.

Because this paper is focusing on the upper-troposphere interactions affecting optical turbulence, this analysis concentrates on heights above the boundary layer from 3000 m to 17500 m. The model's sponge layer extends from 17.5 km to 20 km, making any quantitative or qualitative comparison in that region minimally valuable. The model balloon ascent assumes "steady state" by using 3-D model flow field at *a single model output time* during its ascent. Although steady state is a reasonable approximation to the synoptic conditions shown by *Thermosondes 21 – 22* it may not as reasonable approximation to the dynamic synoptic conditions depicted by *Thermosondes 2-19*. As a result, this may be the source of some error in the profiles.

Results from the surface to 3000 m, as represented by *Thermosonde 2* in Figure 24, are not commented on here since this paper is not focused in the boundary layer.

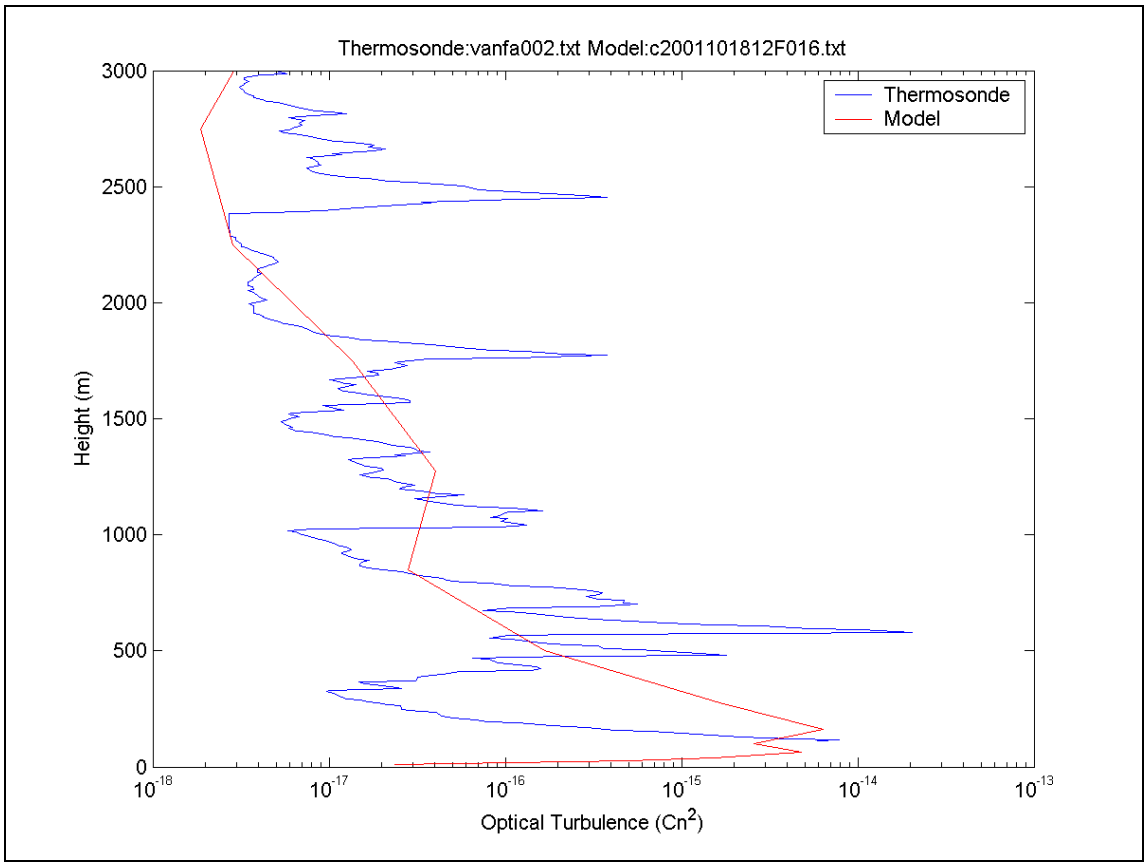

Figure 24. Representative comparison of boundary layer.

Trends from this analysis will identify model discrepancies, allowing detailed investigation into the possible causes. Profiles that exhibit similar patterns and maintain values within an order of magnitude are considered acceptable. Profiles that diverge with values exceeding an order of magnitude are considered unacceptable, thus model failure. This in turn will give some insight into possible corrections that should be applied.

1. Thermosonde 2

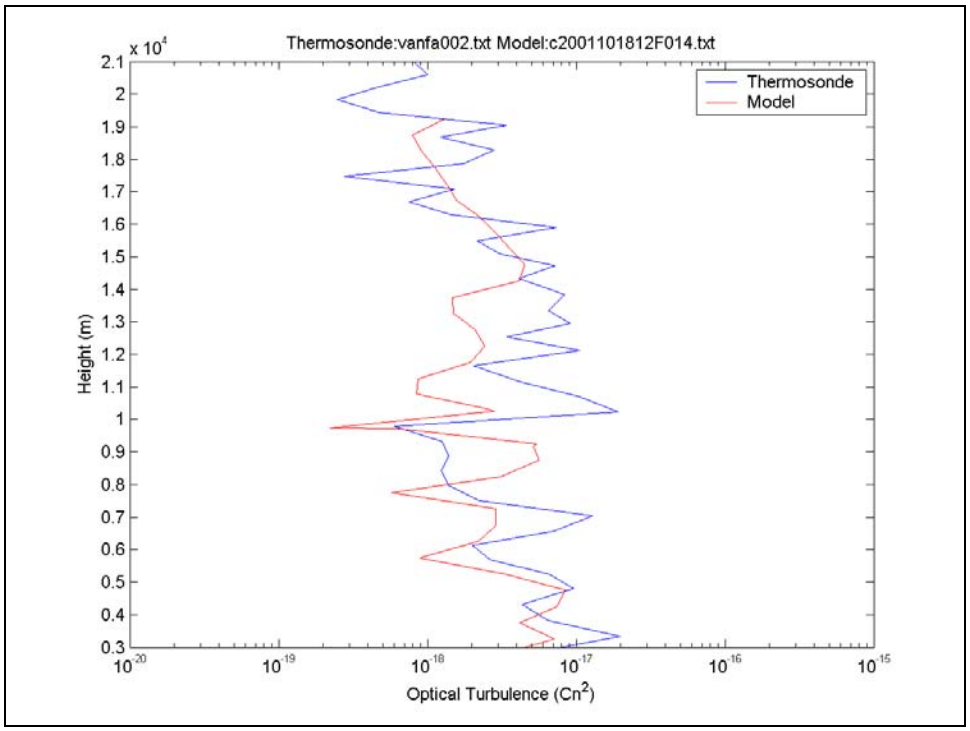

Figure 25. C_n^2 profile comparison for 19OCT01 02Z.

The most notable artifact in Figure 25 is the under-forecasting of C_n^2 present just above 10 km. The error of the model is one order of magnitude. However, when the peak in the thermosonde profile is compared to the 9 km model value, forecast error is less. Further comparison between thermosonde and model derived skew-T's, Figures 146 and 167, indicate that the stronger winds were forecast at a higher level than those measured by the thermosonde. Possibly relevant as well, the model's dewpoint temperature was higher than the actual environment, indicating cloud ice at 300 mb or 9km in the model.

2. Thermosonde 3

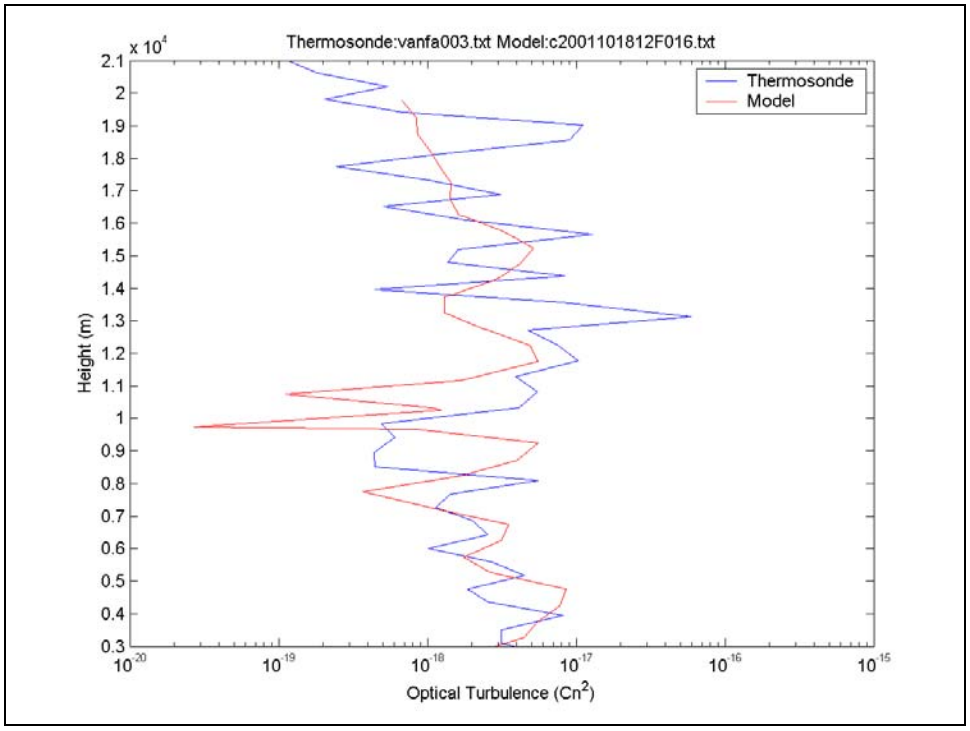

Figure 26. C_n^2 profile comparison for 19OCT01 04Z.

In Figure 26, the model appears to follow the thermosonde relatively well with the exception of under-forecasting turbulence at 11 and 13 km. The trend of the model does show an increase at 12 km but appears to dampen it out too quickly as the altitude increases. The only apparent deviation between corresponding skew-T's is the higher dewpoint temperature in the model, Figures 147 and 168. Again, the model does indicate the presence of cloud ice just above 9 km.

3. Thermosonde 5

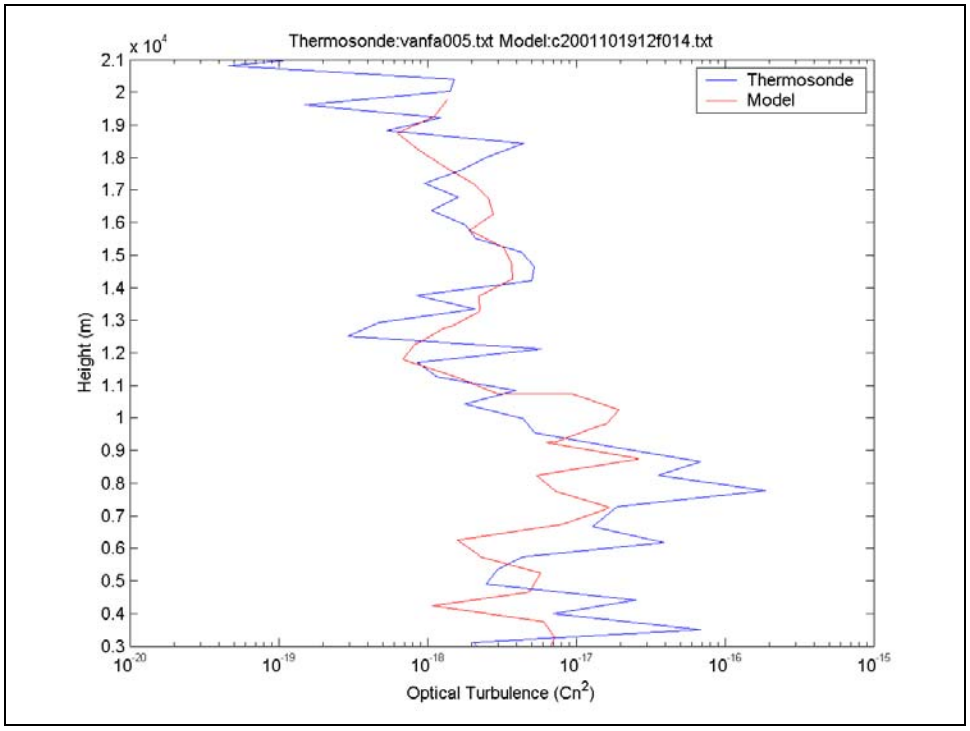

Figure 27. C_n^2 profile comparison for 20OCT01 02Z.

The first deviation in this case occurs at an altitude around 4 km, as seen in Figure 27. Comparison between the thermosonde and model vertical profiles point to a significant drying at the 600 mb level that is not represented by the model's profile, Figures 149 and 169. At 8 km, the thermosonde records much lower dewpoint temperature than what is modeled while significant cloud ice is shown in the model.

4. Thermosonde 6

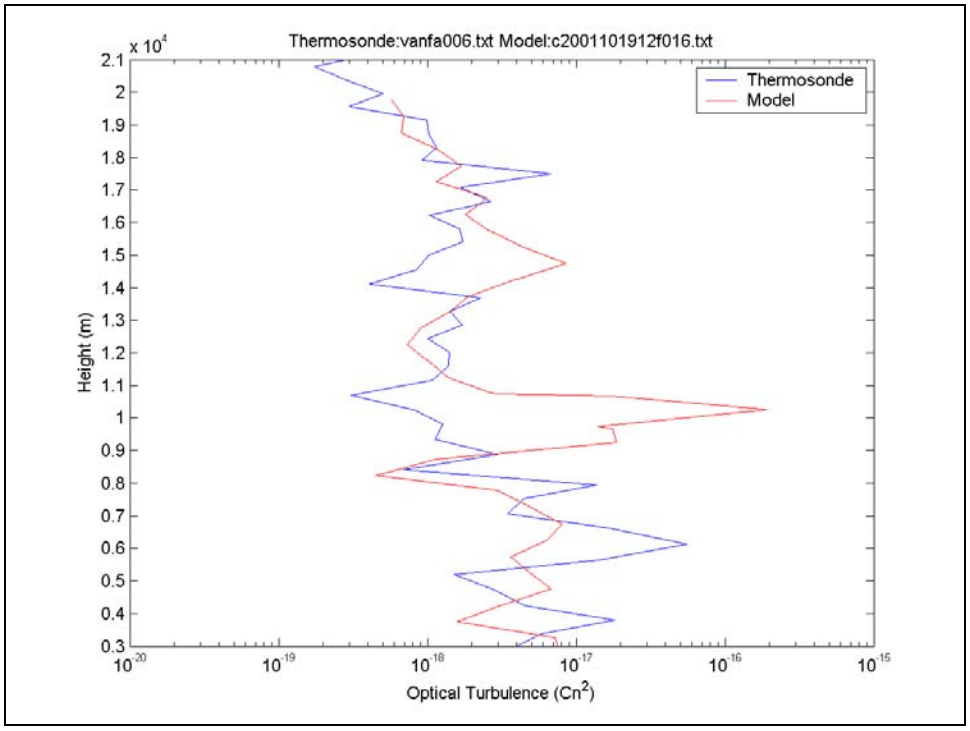

Figure 28. C_n^2 profile comparison for 20OCT01 04Z.

Unlike the previous cases, Figure 28 shows that the model has over-forecast the turbulence at 10 and 15 km while under-forecasting it at 4 and 6 km. At the under-forecasted levels, the thermosonde again indicates a much dryer layer that what the model forecast, Figures 150 and 170. As for the over-forecasts, higher dewpoint temperatures are shown in the model profile with indications of significant cloud ice around 9 km, also model winds are slightly stronger from 250 mb to 150 mb.

5. Thermosonde 7

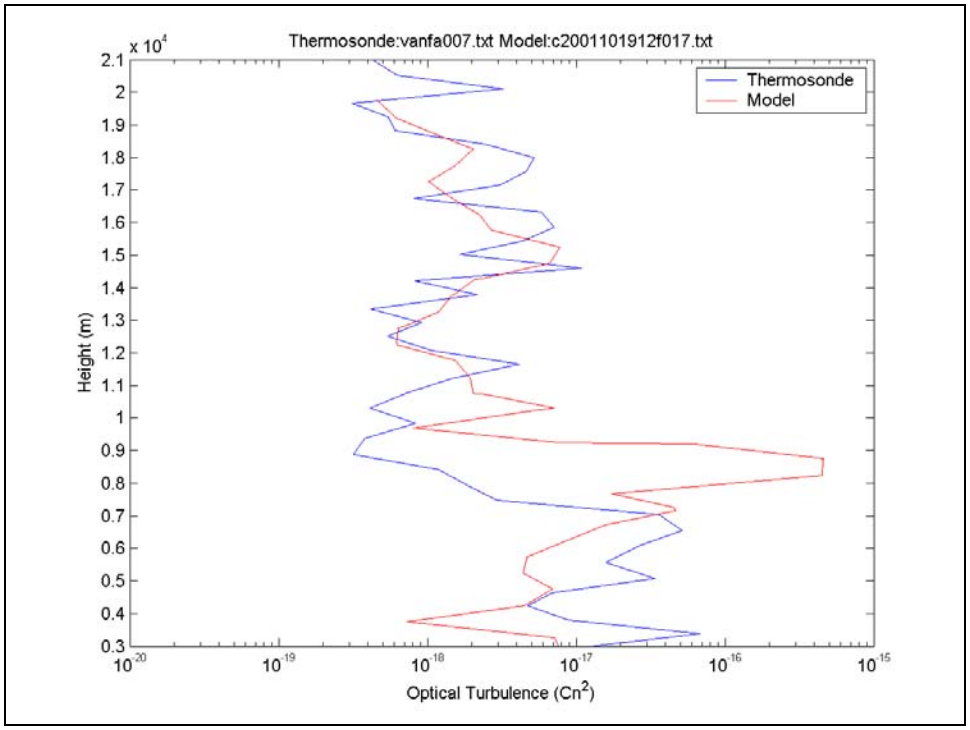

Figure 29. C_n^2 profile comparison for 20OCT01 05Z.

The analysis for Figure 29 is very similar to that of Figure 28, obviously due to time similarities. The under-forecasted turbulence at 3.5 km corresponds to a much dryer layer than what the model has depicted. Slightly stronger model winds and a warmer dewpoint temperature differentiate the model profile from the thermosonde profile relative to the over-forecast seen at 9 km, Figures 151 And 171. This is complemented by a strong indication of cloud ice around 8.5 km. No strong indications of vertical wind shear seemed to be present.

6. Thermosonde 10

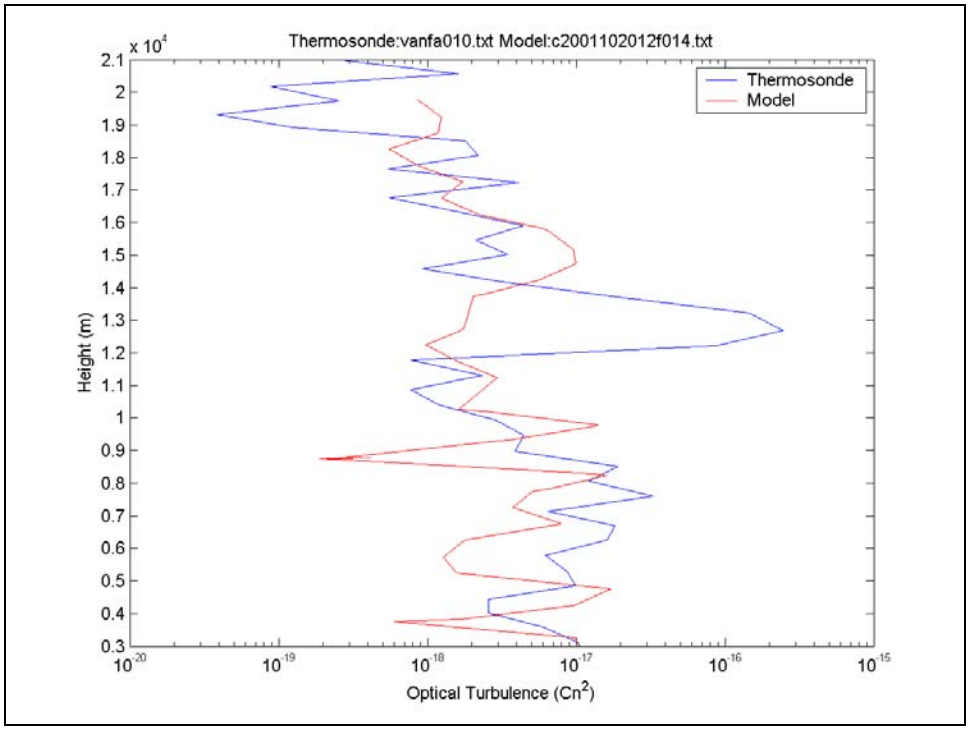

Figure 30. C_n^2 profile comparison for 21OCT01 02Z.

This profile comparison shown in Figure 30 indicates a severe under-forecast at 13 km. This anomaly corresponds to an increase in temperature on the sounding that indicates it is at the tropopause. Greater vertical wind shear is recorded at this level than was modeled, Figures 153 and 172. The model once again depicts a larger dewpoint temperature than the thermosonde with cloud ice present at 8.5 km. The under-forecast at 9 km seems to correspond with a less stable gradient in the model than measured.

7. Thermosonde 11

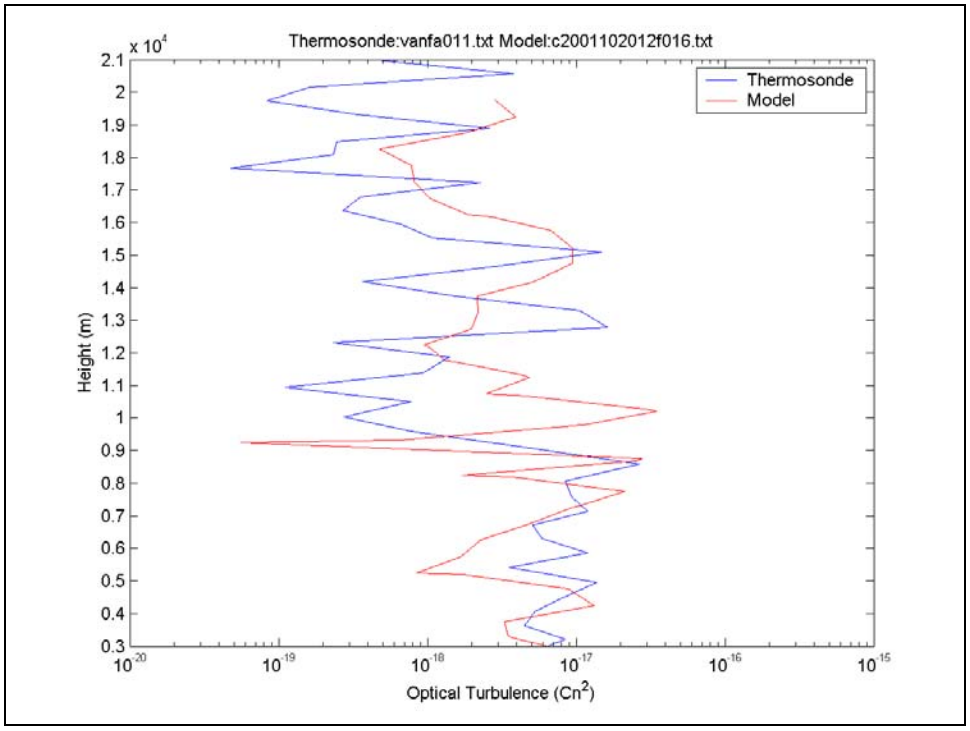

Figure 31. C_n^2 profile comparison for 21OCT01 04Z.

The most significant deviation of the model in Figure 31 appears to be the over-forecast at 10 km. Two peaks in cloud ice are modeled at 8.5 km and 10 km, the first of which being more pronounced with cloud indicated on satellite imagery. The model indicates a dryer and less stable layer than what was actually measured, Figures 154 and 173. Otherwise the trend seems reasonably depicted.

8. Thermosonde 12

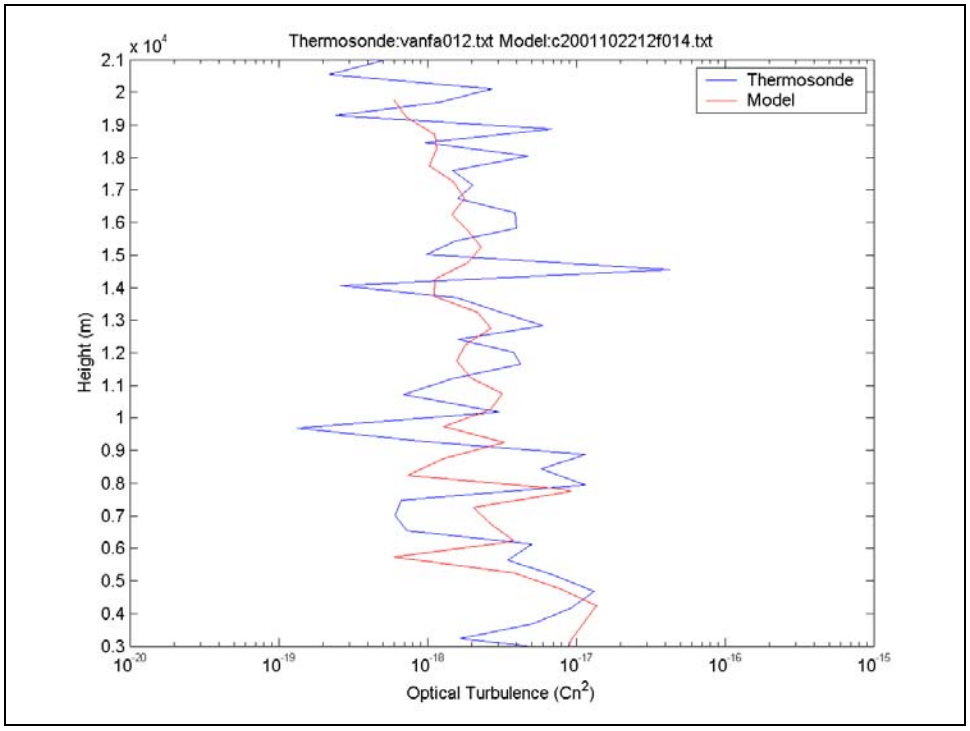

Figure 32. C_n^2 profile comparison for 23OCT01 02Z.

With the exception of the under-forecast that occurs at 15 km, the model profile shown in Figure 32 appears to closely parallel the thermosonde trends but offset by about 1 km below that of the thermosonde. The only definitive difference that can be noted between model and measurement is that the temperature gradient of the model at 15 km is less stable in the model, Figures 156 And 174. No conclusive information can be obtained from the dewpoint temperature due to apparent sensor failure.

9. Thermosonde 13

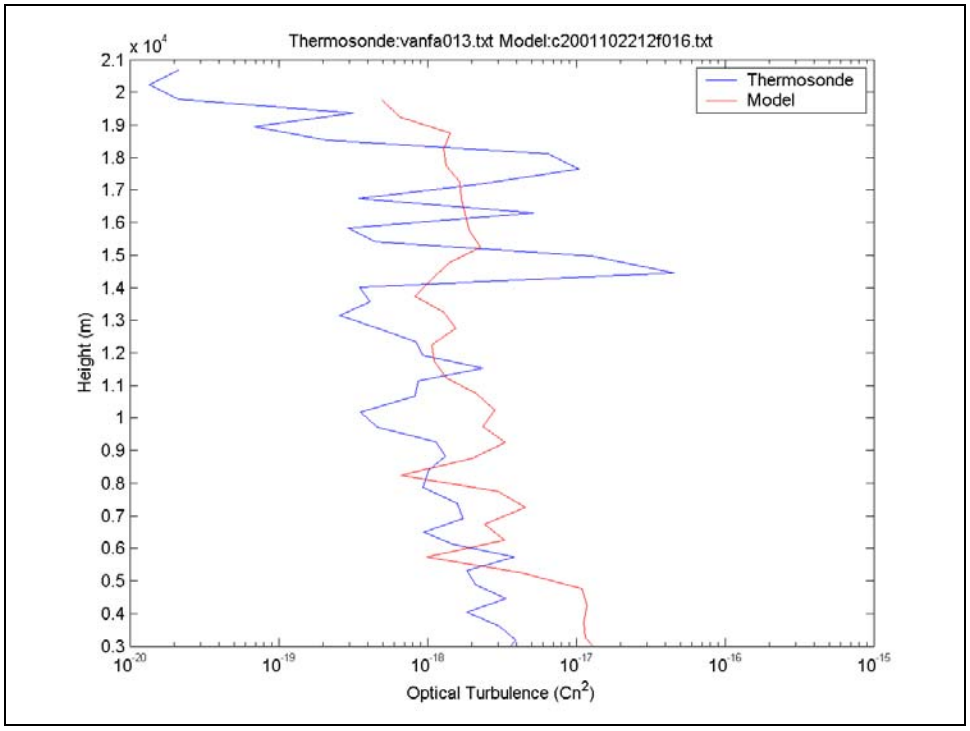

Figure 33. C_n^2 profile comparison for 23OCT01 04Z.

Two instances of under-forecasting occur in the and above the stratospheric boundary layer as shown in Figure 33. The model depicts both a less stable temperature gradient and higher dewpoint temperature than the thermosonde, Figures 157 And 175.

10. Thermosonde 15

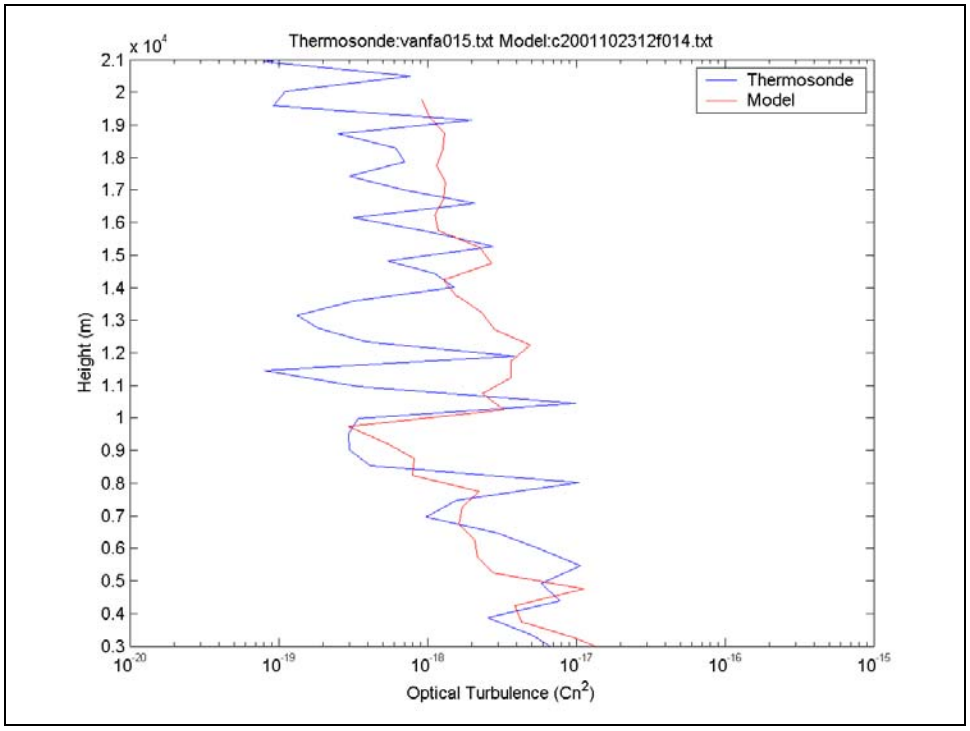

Figure 34. C_n^2 profile comparison for 24OCT01 02Z.

The over-forecast that occurs from 11 km to 14 km in Figure 34 appears to correlate with the more erratic dewpoint temperature structure of the thermosonde that was not represented in the moister and more stable structure of the model, Figures 159 and 176.

11. Thermosonde 16

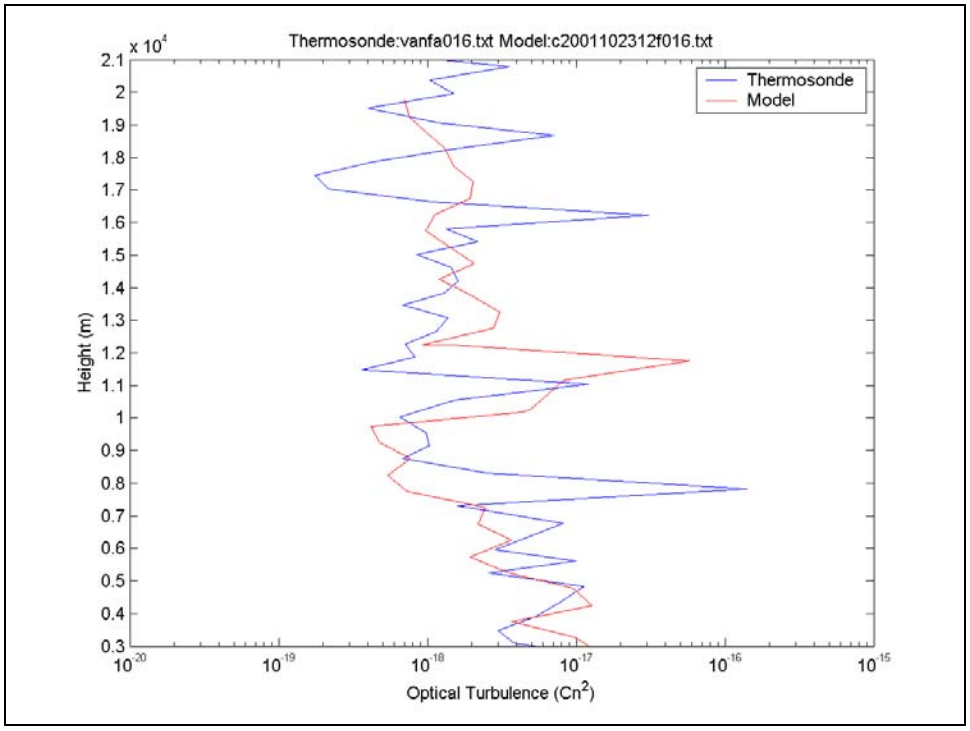

Figure 35. C_n^2 profile comparison for 24OCT01 04Z.

The only marked deviation of the model in the case shown in figure 35 appears at 8 km. With the exception of weaker winds in the model at that level, no definitive differences can be drawn from the skew-T profiles for this occurrence, Figures 160 And 177. No cloud ice was modeled in the profile.

12. Thermosonde 17

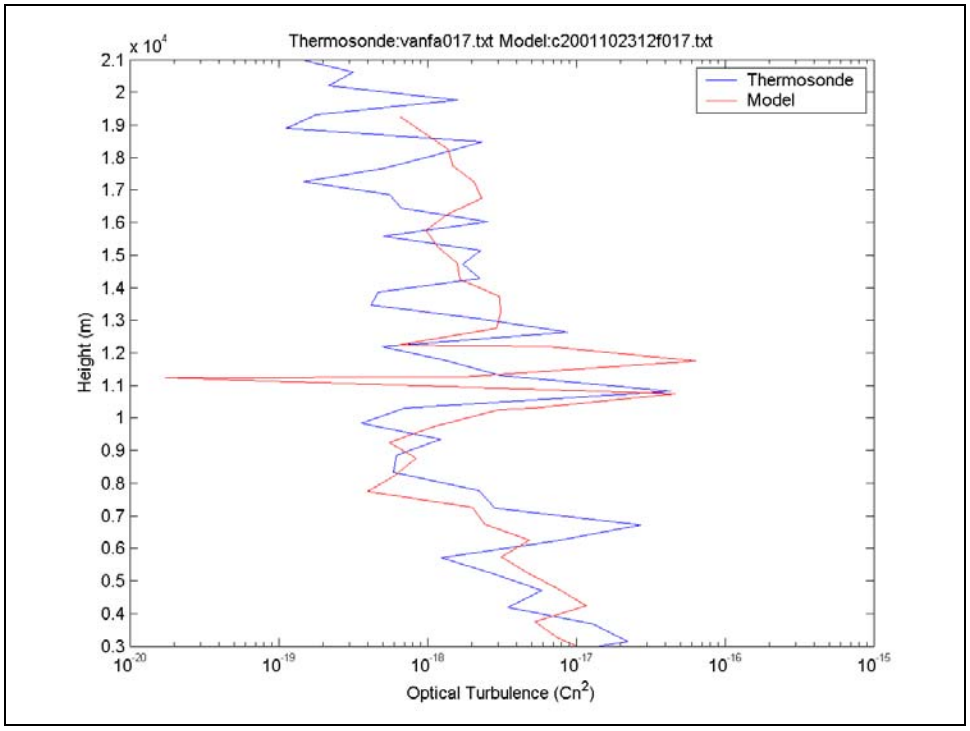

Figure 36. C_n^2 profile comparison for 24OCT01 04Z.

This model run reasonably mimics the thermosonde profile, as seen in Figure 36. The cause of the one anomaly at 11 km is uncertain when vertical profiles are compared, Figures 160 And 178. No cloud ice was present in the model.

13. Thermosonde 18

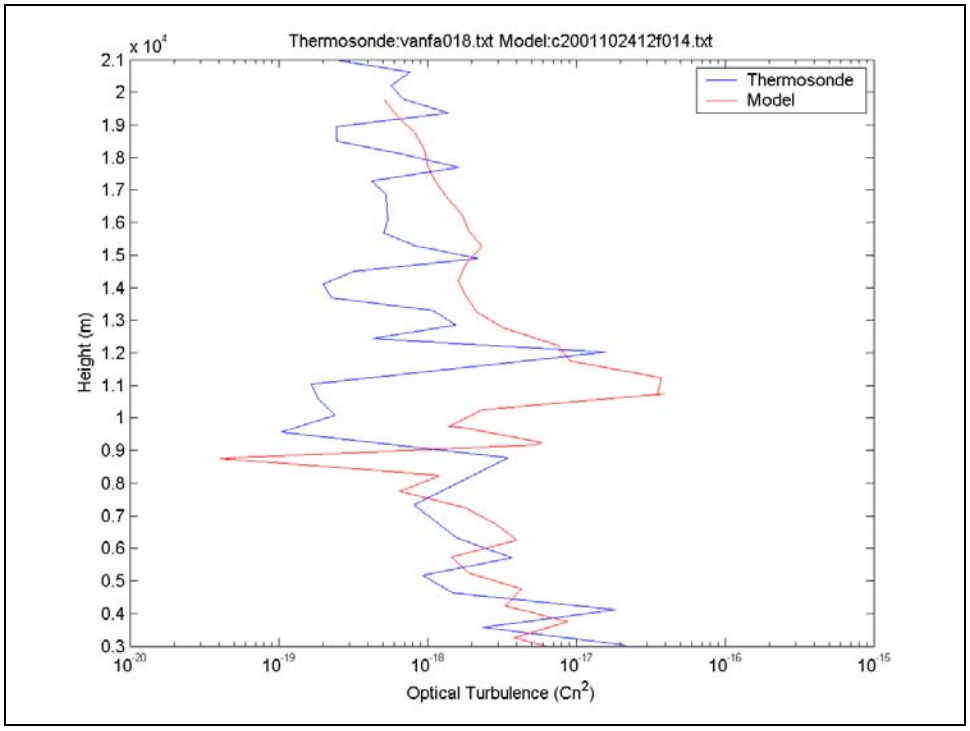

Figure 37. C_n^2 profile comparison for 25OCT01 02Z.

The profiles for the case shown in Figure 37 are reasonably similar. Although the levels are not exactly matched, the trends are represented, Figures 162 And 179. Cloud ice is present in the model at 11 km.

14. Thermosonde 19

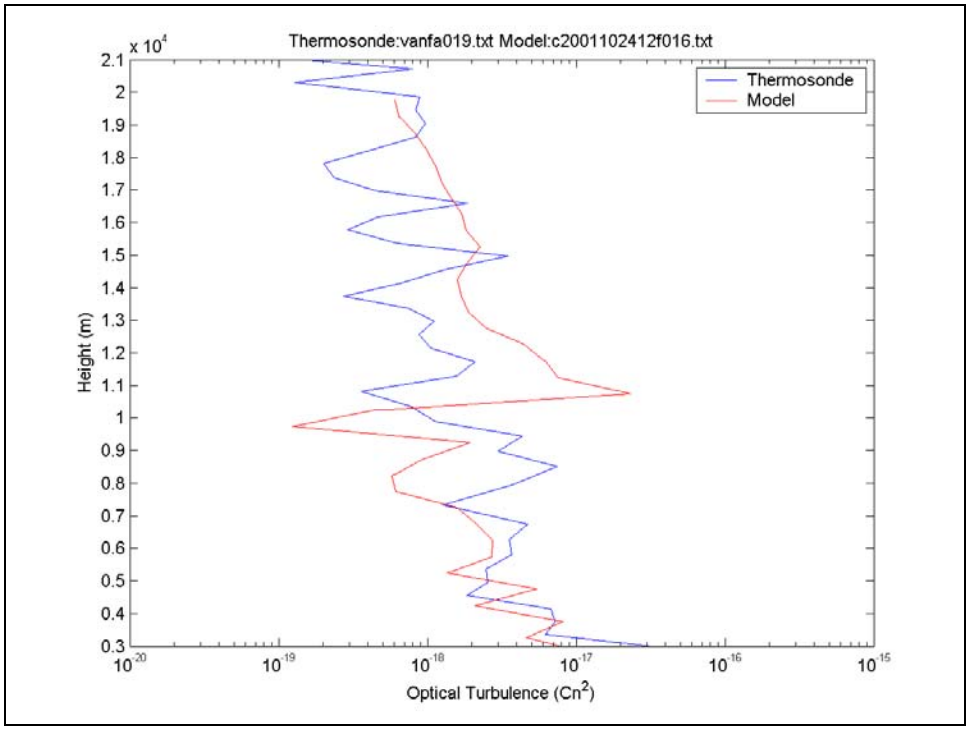

Figure 38. C_n^2 profile comparison for 25OCT01 04Z.

At 11 km the thermosonde indicates significant drying in Figure 38, indicative of the stratospheric boundary, however the model does not depict this when Figures 163 and 180 are compared.

15. Thermosonde 21 and Thermosonde 22

No comments are provided for *Thermosondes 21 and 22* (Figures 39 and 40) because model and thermosonde profiles are relatively consistent with one another. Also, no cloud ice was modeled in either case.

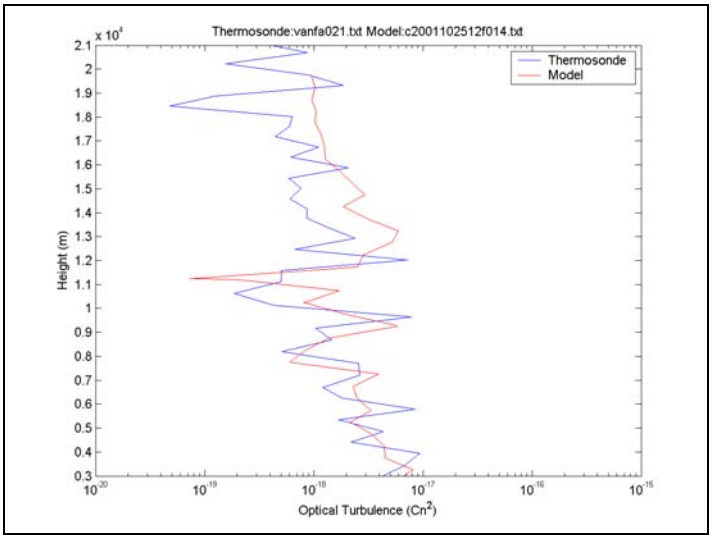

Figure 39. C_n^2 profile comparison for 26OCT01 02Z.

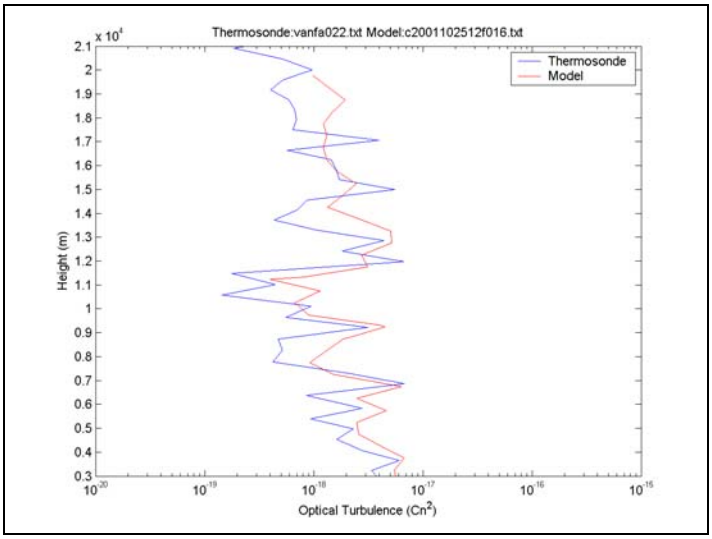

Figure 40. C_n^2 profile comparison for 26OCT01 04Z.

C. QUANTITIVE EVALUATION OF C_n^2 PROFILES DERIVED FROM THERMOSONDE AND COAMPS DATA

The quantitative evaluation of the model's performance was determined by taking the C_n^2 from both the model and thermosonde data used in Section B and determining the isoplanatic angle (θ_o) for adaptive optics, which weighs mid- and upper-troposheric C_n^2 more heavily. The θ_o is a measurement of a plane over which a source of light would undergo wavefront distortions. The critical θ_o value that separates severe from non-severe optical turbulence is $4.5 \mu rads$. Any values that fall below this is considered severe optical turbulence. Values that fall above this number are considered non-severe. Therefore, the model simulations giving larger values than what was observed are indicating a bias towards predicting weaker turbulence that what was measured. The equation used to determine θ_o is defined as (Fried, 1982)

$$\theta_o = \left[2.91 \, (2\pi / \lambda)^2 \int_0^H h^{\frac{5}{3}} C_n^2(h) \, dh \right]^{-\frac{3}{5}} . \qquad (21)$$

For this case, the λ was set to 0.5 μm and the integration was evaluated from the surface to 17.5 km. Furthermore, the trapezoidal integration process,

$$\int_a^b f(x) \, dx = \sum_{i=1}^{n} \left(x_{i+1} + x_i \right) \left(f_{i+1} + f_i \right) / 2 , \qquad (22)$$

was utilized to determine the integration approximation. Figure 41 shows the results from the October observation period and Table 4 gives the values used.

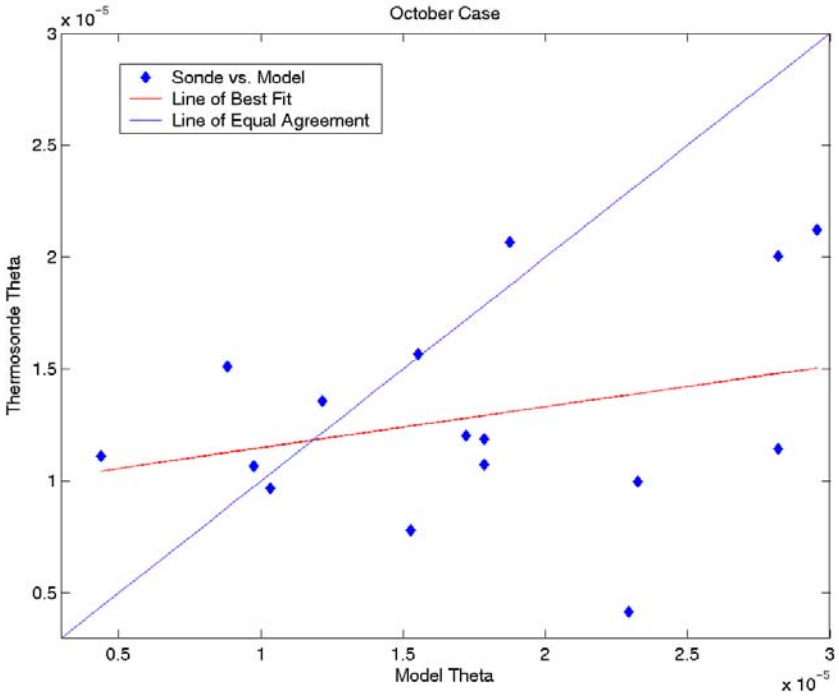

Figure 41. θ_o Scatter plot results for COAMPS and thermosonde C_n^2 values for October 2001.

Thermosonde Number	Thermosonde θ_o	Model θ_o (x1.0e-004)
2	0.1144	0.2819
3	0.0997	0.2324
5	0.0778	0.1526
6	0.1513	0.0882
7	0.1111	0.0438
10	0.0418	0.2292
11	0.1203	0.1720
12	0.1074	0.1785
13	0.1189	0.1784
15	0.1566	0.1552
16	0.0969	0.1032
17	0.1068	0.0976
18	0.1357	0.1216
19	0.2066	0.1875
21	0.2122	0.2954
22	0.2005	0.2818

Table 3. Isoplanatic angle calculations for October.

Similarly this process was applied to the March observation period and results shown in Figure 42 with corresponding values in Table 5.

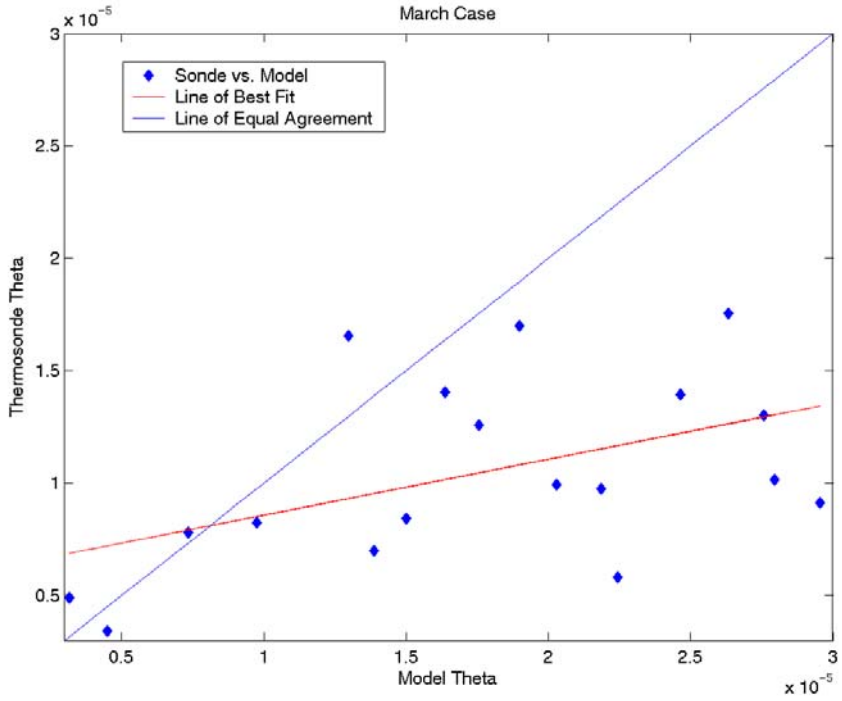

Figure 42. θ_o Scatter plot results for COAMPS and thermosonde C_n^2 values for March 2002.

Thermosonde Number	Thermosonde θ_o	Model θ_o (x1.0e-004)
6	0.1757	0.2632
7	0.1301	0.2759
8	0.0912	0.2955
9	0.0780	0.0733
11	0.0341	0.0449
12	0.0490	0.0316
13	0.0992	0.2030
14	0.1700	0.1897
15	0.1406	0.1638
16	0.1656	0.1298
17	0.0823	0.0974
18	0.0844	0.1501
19	0.1017	0.2795
20	0.1260	0.1756
21	0.0699	0.1387
22	0.1396	0.2463
23	0.0581	0.2245
24	0.0976	0.2185

Table 4. Isoplanatic angle calculations for March.

From the plots shown in Figures 41 and 42, the conclusion can be drawn that the model's overall tendency is to over-forecast C_n^2 using the TKE Method. This may be attributed to the smoothing caused by courser resolutions in the upper atmosphere, as the standard COAMPS vertical resolution scheme does.

To test this hypothesis, the model was re-run with 83 vertical levels for selected cases in October and March. For October, model runs corresponding to *Thermosondes 5-10* were analyzed to investigate the jet event that took place on October 21st. For March, the model runs corresponding to *Thermosonde 22,23 and 24* were used because a strong jet was present. Qualitative results for October and March are given in Figures 43 and 44, respectively.

Figure 43 indicates that the increased resolution did improve two of the four forecasts in the October cases, with one showing no improvement. These results were encouraging, however, when applied to the selected March observation period (Figure 44), the forecasts in all three cases deteriorated. This indicates that there is promise in improving turbulence forecasting by increasing the resolution but that resolution alone will not provide a complete solution.

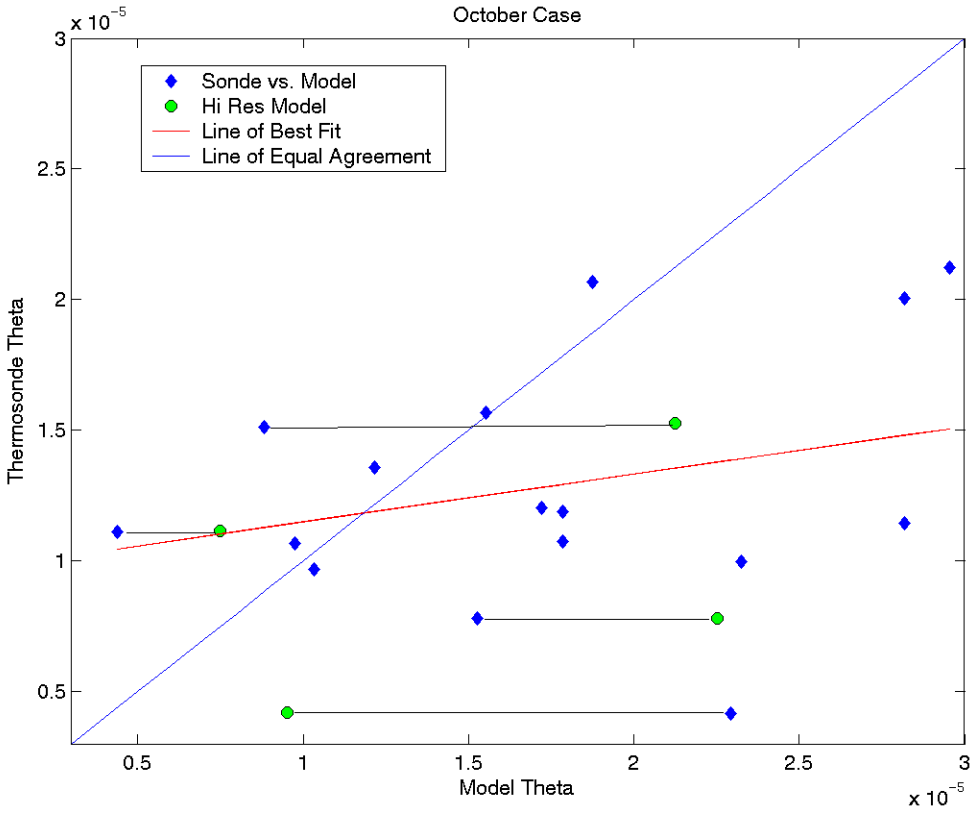

Figure 43. Hi-resolution COAMPS results for October 2001.

Thermosonde Number	Thermosonde θ_o	Model θ_o	Hi-Res θ_o (x1.0e-004)
2	0.1144	0.2819	
3	0.0997	0.2324	
5	0.0778	0.1526	**0.2252**
6	0.1513	0.0882	**0.2124**
7	0.1111	0.0438	**0.0748**
10	0.0418	0.2292	**0.0951**
11	0.1203	0.1720	
12	0.1074	0.1785	
13	0.1189	0.1784	
15	0.1566	0.1552	
16	0.0969	0.1032	
17	0.1068	0.0976	
18	0.1357	0.1216	
19	0.2066	0.1875	
21	0.2122	0.2954	
22	0.2005	0.2818	

Table 5. Higher resolution isoplanatic angle results for October 2001.

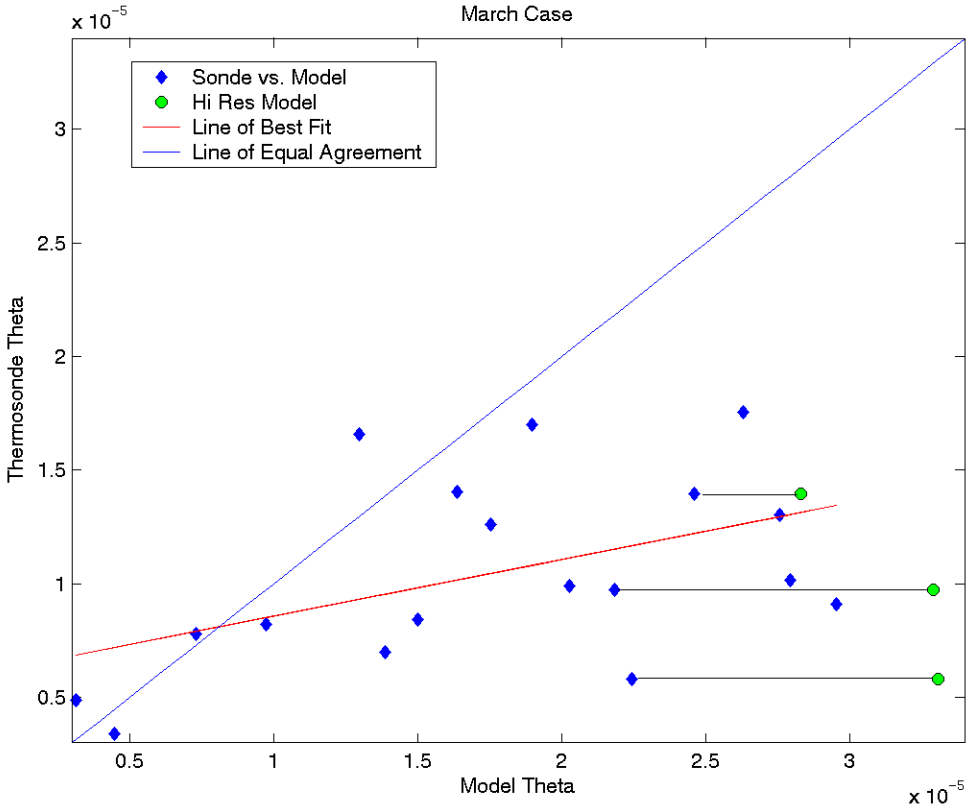

Figure 44. Hi-resolution COAMPS results for March 2001.

Thermosonde Number	Thermosonde θ_o	Model θ_o	Hi-Res θ_o (x1.0e-004)
6	0.1757	0.2632	
7	0.1301	0.2759	
8	0.0912	0.2955	
9	0.0780	0.0733	
11	0.0341	0.0449	
12	0.0490	0.0316	
13	0.0992	0.2030	
14	0.1700	0.1897	
15	0.1406	0.1638	
16	0.1656	0.1298	
17	0.0823	0.0974	
18	0.0844	0.1501	
19	0.1017	0.2795	
20	0.1260	0.1756	
21	0.0699	0.1387	
22	0.1396	0.2463	**0.2833**
23	0.0581	0.2245	**0.3307**
24	0.0976	0.2185	**0.3290**

Table 6. Higher resolution isoplanatic angle results for March 2002.

VI. CONCLUSIONS AND RECOMMENDATIONS

The quantitative results for October seemed to show that there was improvement in forecasting turbulence in two of the four cases, model runs corresponding to *Thermosondes 7 and 10*; the model *Thermosonde 10* showing drastic improvement. One case, corresponding to *Thermosonde 6*, showed no forecast improvement but did increase the amount of modeled turbulence. Finally, the model corresponding to *Thermosonde 5,* increased the optical turbulence and decreased the forecast quality.

The quantitative results for March all indicate that increasing the resolution lead to increasing the turbulence modeled, deviating farther from the thermosonde calculated optical turbulence than the low resolution values.

Considering the synoptic patterns affecting each of these cases, one factor that may have attributed to the different results is the type of jet over the point of interest. In the October case, an offshoot of the STJ is affecting the mesoscale, while the PFJ is interacting with the STJ over California in the March case. The different driving mechanisms, height levels, and interaction can all be affecting the model structure.

Although these findings are inconclusive, they do indicate that increasing the vertical resolution is one small part of the larger puzzle. When weighing the increased computational cost caused by increasing the vertical resolution verses the value added, this study seems to indicate that the cost may be too high. More

likely, improving parameterization relationships may have a greater impact at this time.

Other areas that could be studied include; the cloud ice parameterization and its affects on the calculation of optical turbulence, deviations in the moisture content being modeled at and above the tropopause as compared to actual measurements, and the eddy diffusivity to altitude relationship. Additionally, a manuscript in preparation by Miller and Walters due for publication in 2004 suggest that the TKE-Free Method could yield better results in a high-shear environment, therefore a detailed comparative analysis between the TKE and TKE Free Methods for the same time periods would be useful and enlightening.

LIST OF REFERENCES

Beniston, M., 1998: *From Turbulence to Climate*. Springer,328 pp.

Bougeault, P., C. D. Hui, B. Fleury, and H. J. Laurent, 1995: Investigation of seeing by means of an atmospheric mesoscale numerical simulation, *Appl. Opt.*, **34**, 3481-3488.

Deardorff, J. W., 1980: Stratocumulus-capped mixed layers derived from a three-dimensional model, *Bound. Layer Meteor.,***18**, 495-527.

Ellrod, G., cited 2004: Clear Air Turbulence. [Available at http://orbit-net.nesdis.noaa.gov/arad/fpdt/CAT.html.]

Fried, D. L., 1982: Anisoplanatism in adaptive optics, *J. Opt. Soc. Amer. A.*, **72**, 52-61.

Gal-Chen, T. and R. C. J. Somerville, 1975: On the use of a coordinate transformation for the solution of the Navier-Stokes equations, *J. Computational Phys.*, **17**, 209-228.

Hodur, R. M., 1997: The Naval Research Laboratory's Coupled Ocean/Atmosphere Mesoscale Prediction System (COAMPS), *Mon. Wea. Rev.*, **125**, 1414-1430.

Kolmogorov, A. N., 1941: The local structure of turbulence in incompressible viscous fluid for very large Reynolds numbers, *Doklady Akad. Nauk. USSR*, **30**, 301.

Kondo, J., O. Kanechika, and N. Yasuda, 1978: Heat and momentum transfers under strong stability in the atmospheric surface layer, *J. Atmos. Sci.*, **35**, 1012-1021.

Klemp, J. B., and R. B. Wilhelmson, 1978: The Simulation of Three-Dimensional Convective Storm Dynamics**,** *J. Atmos. Sci.*, **35**, 1070–1096.

Kyle, T.G., 1993: Turbulence and Optics. *Atmospheric Transmission, Emission and Scattering,* Los Alamos National Laboratory, Butterworth-Heinemann, 140-155.

Lee, J. T., and R. Crane, 1994: Aeronautical Meteorology. *McGraw-Hill Encyclopedia of Science and Technology*, *8th Ed.*, 151-154.

Mahalov, A., and B. Nicolaenko, cited 2004: Clear air and optical turbulence in a jet stream in the airborne laser context.
[http://www.navo.hpc.mil/Navigator/Spring03_Feature3.html.]

Mellor, G. L., 1973: Analytic prediction of stratified planetary surface layers, *J. Atmos. Sci.,* **30**, 1061-1069.

_____, and T. Yamada, 1974: A hierarchy of turbulence closure models for planetary boundary layers, *J. Atmos. Sci*., **31**, 1791-1292.

_____, and T. Yamada, 1982: Development of a turbulent closure model for geophysical fluid problems,' *Rev. Geophysics and Space Physics*, 20, 851-875.

Meteorological Office College, 1996: Turbulence and Gust. *Source Book to the Forecasters' Reference*, The Met. Office, 1-12.

Miller, D. K., D. L. Walters, A. Slaviv, 2001: Evaluation of turbulent mixing length parameterization applied to the case of an approaching upper-troposheric trough. Preprints of the Ninth Conference on Mesoscale Processes, Ft. Lauderdale, FL.

Nuss, W. A., and D. F. Titley, 1994: Use of multiquadric interpolation for meteorological objective analysis, *Mon. Wea. Rev.,* **122**, 1611-1632.

Rosendal, H., cited 2004: Clear air turbulence and the cut-off low. [http://members.aol.com/Rosendalhe/clearair.htm]

Tjernstrom, M., 1993: Turbulence length scales in stably stratified free shear flow analyzed from slant aircraft profiles. *J. Appl. Meteor.,* **32**, 948-963.

Walters, D. L., 1995: Measurement of optical turbulence with higher-order structure functions, *Appl. Opt.,* **34**, 1591-1597.

_____, and L.W. Bradford, 1997: Measurements of r_o. and θ_o : two decades and 18 sites, *Appl. Opt.,* **36**, 7876-7886.

_____, and D. K. Miller, 1999: Evolution of an upper-tropospheric turbulence event – Comparison of observations to numerical simulations. Preprints of the 13th Symposium on Boundary Layers and Turbulence, Dallas, TX.

Warner, T. T., Peterson, R. A., and Treadon, R. E., 1997: A tutorial on lateral boundary conditions as a basic and potentially serious limitation to regional numerical weather prediction. *B. of the Amer. Meteor. Soc.,* **78**, 2599–2617.

Wolfe, W. F., and G. J. Zissis, 1978. Propagation Through Atmospheric Turbulence. *The Infrared Handbook*, Office of Naval Research, Department of the Navy, Washington , DC, 1-49.

APPENDIX A. NCEP CHARTS

NCEP/MCP charts shown in this section were taken from the Pacific Region Synoptic analysis archived by Naval Postgraduate School's Meteorology Department. It was included to provide 00Z and 12Z analysis for the period from 18OCT01 to 25OCT01 and 01MAR02 to 07MAR02. Where this was not possible, the closest archived analysis was used.

1. October 2001

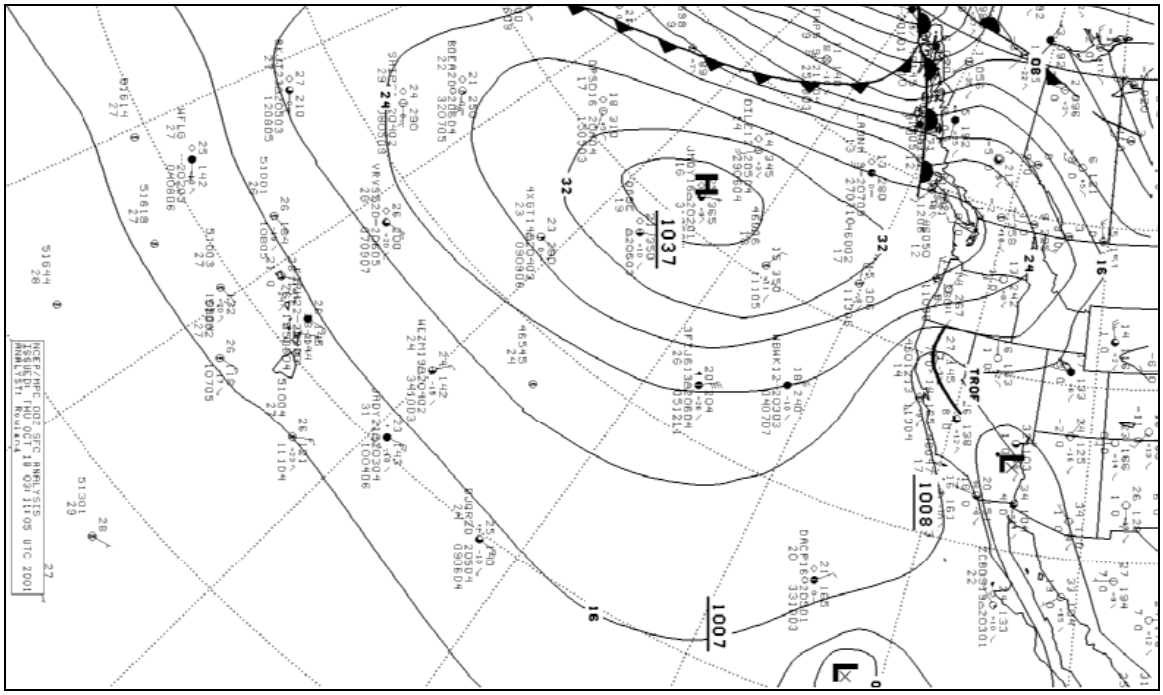

Figure 45. NCEP/MPC 00Z Surface Analysis, 18OCT01.

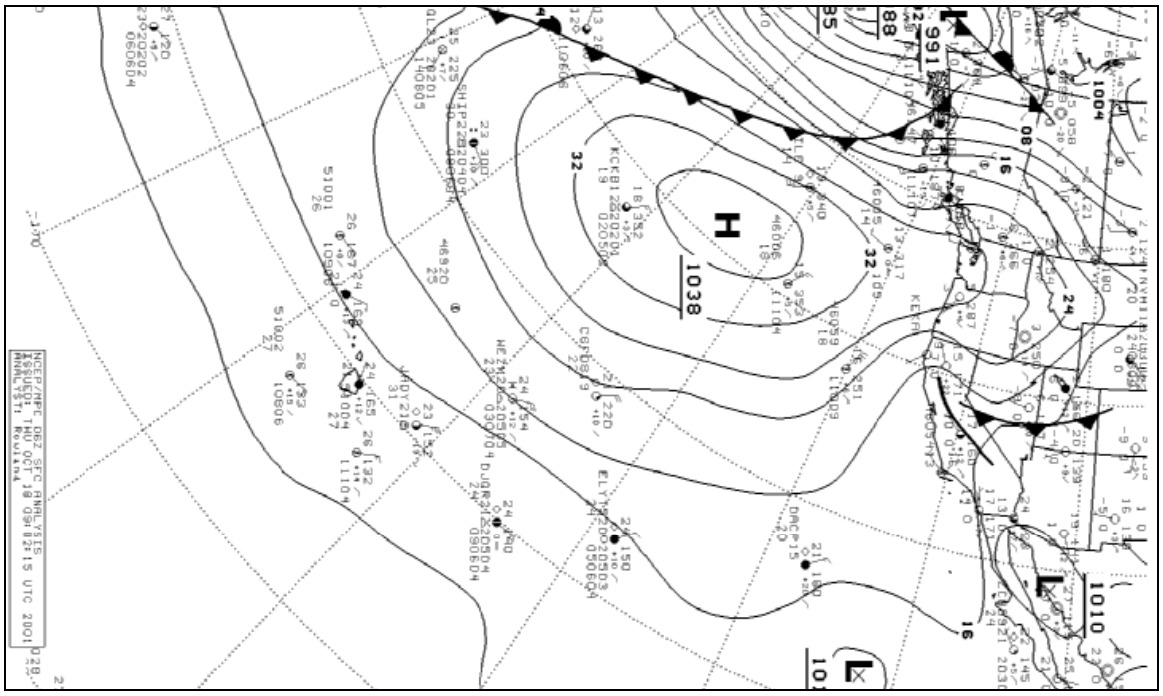

Figure 46. NCEP/MPC 06Z Surface Analysis, 18OCT01.

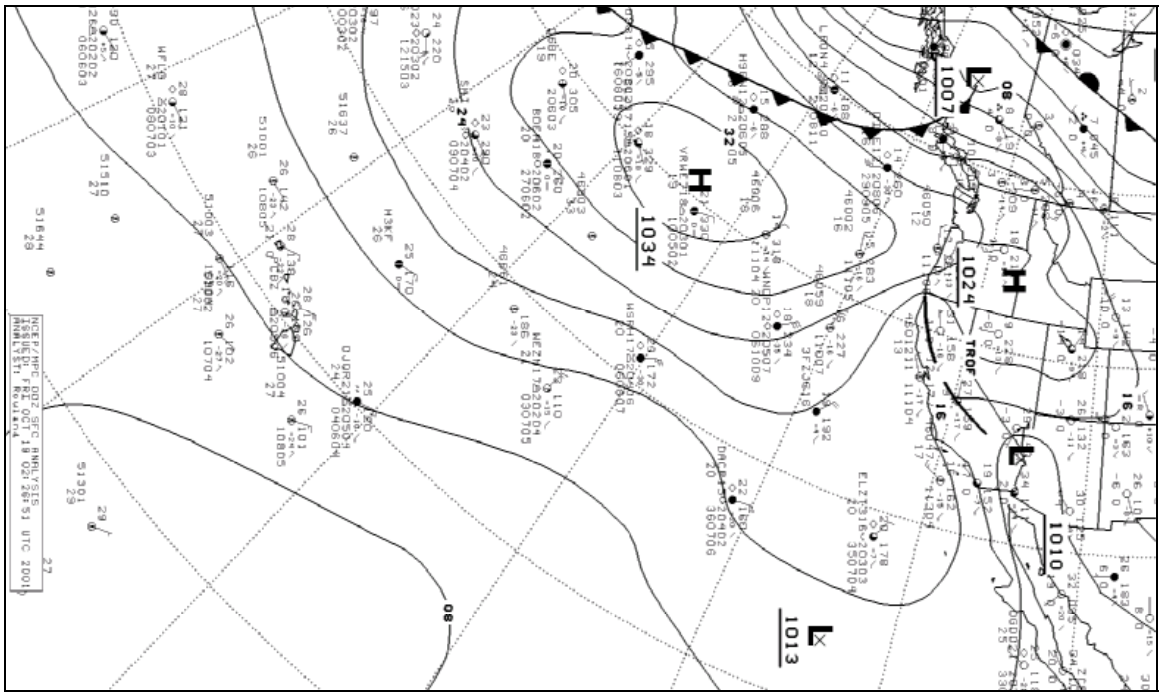

Figure 47. NCEP/MPC 00Z Surface Analysis, 19OCT01.

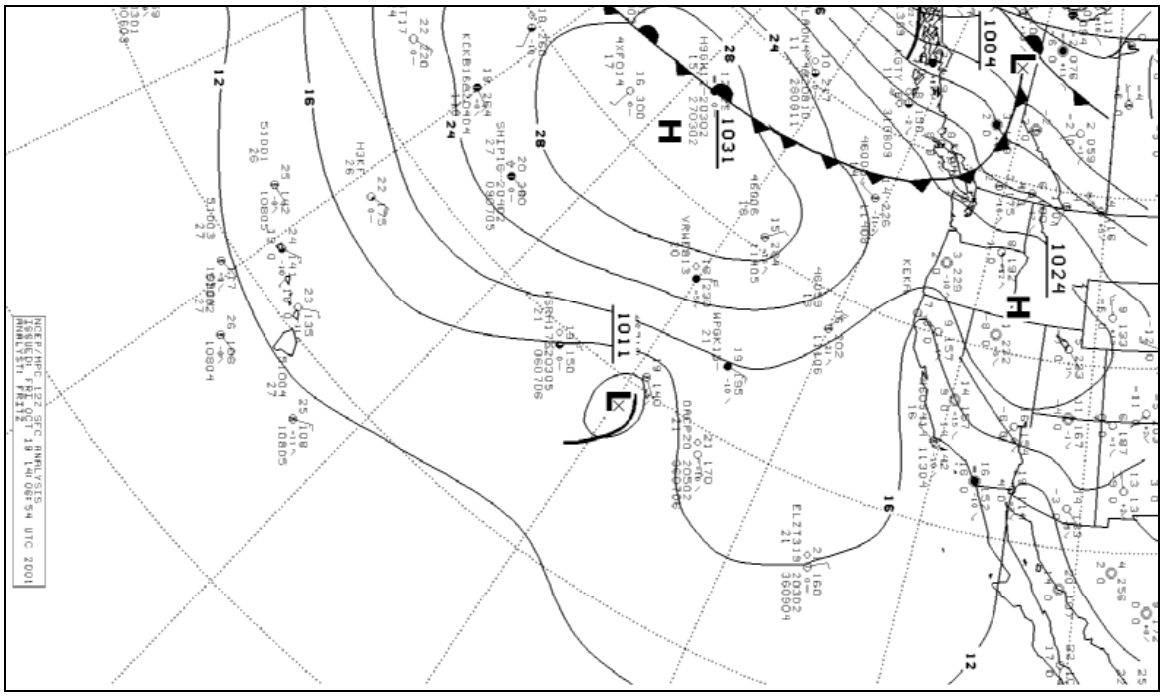

Figure 48. NCEP/MPC 12Z Surface Analysis, 19OCT01.

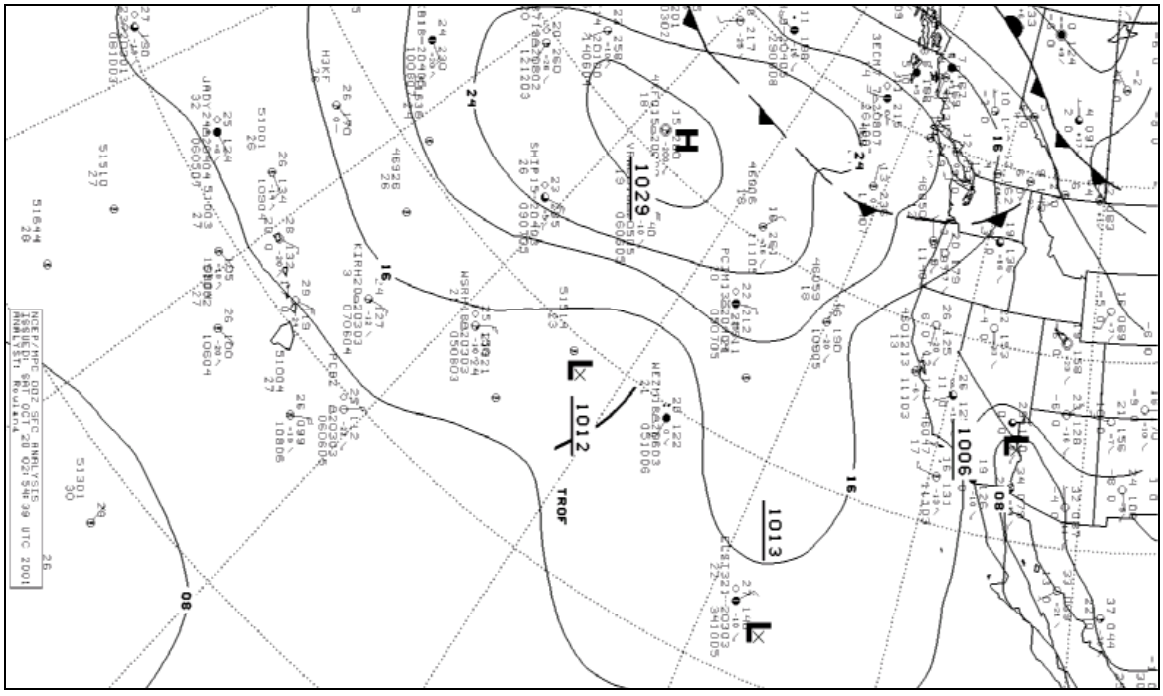

Figure 49. NCEP/MPC 00Z Surface Analysis, 20OCT01.

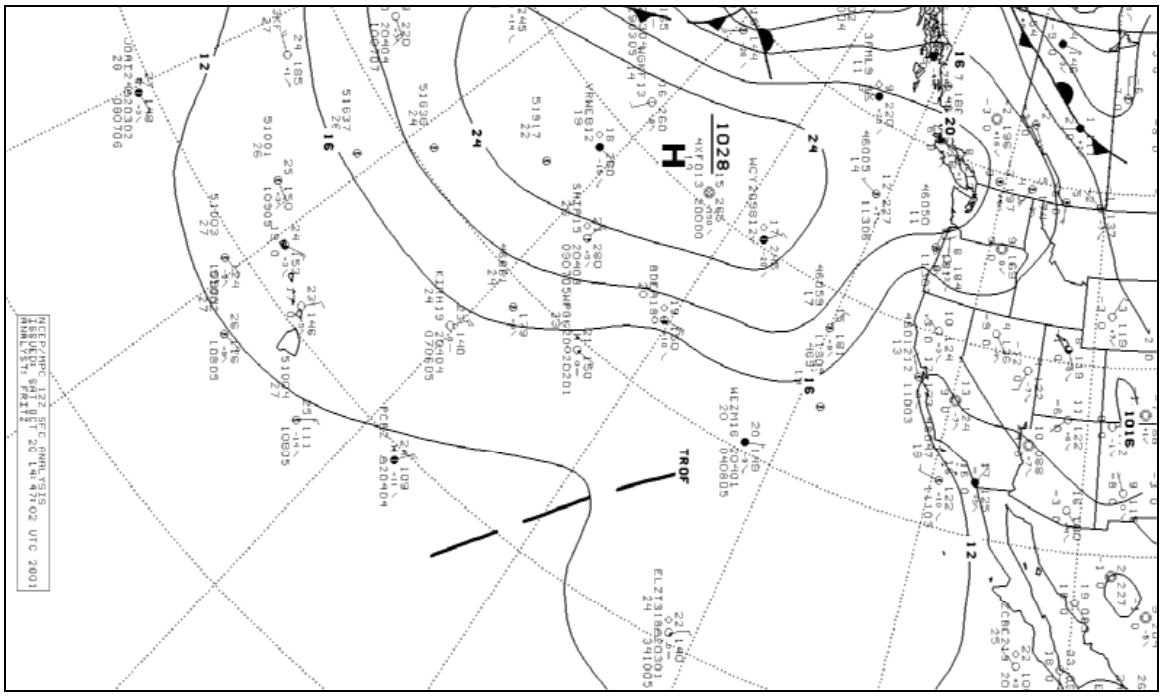

Figure 50. NCEP/MPC 12Z Surface Analysis, 20OCT01.

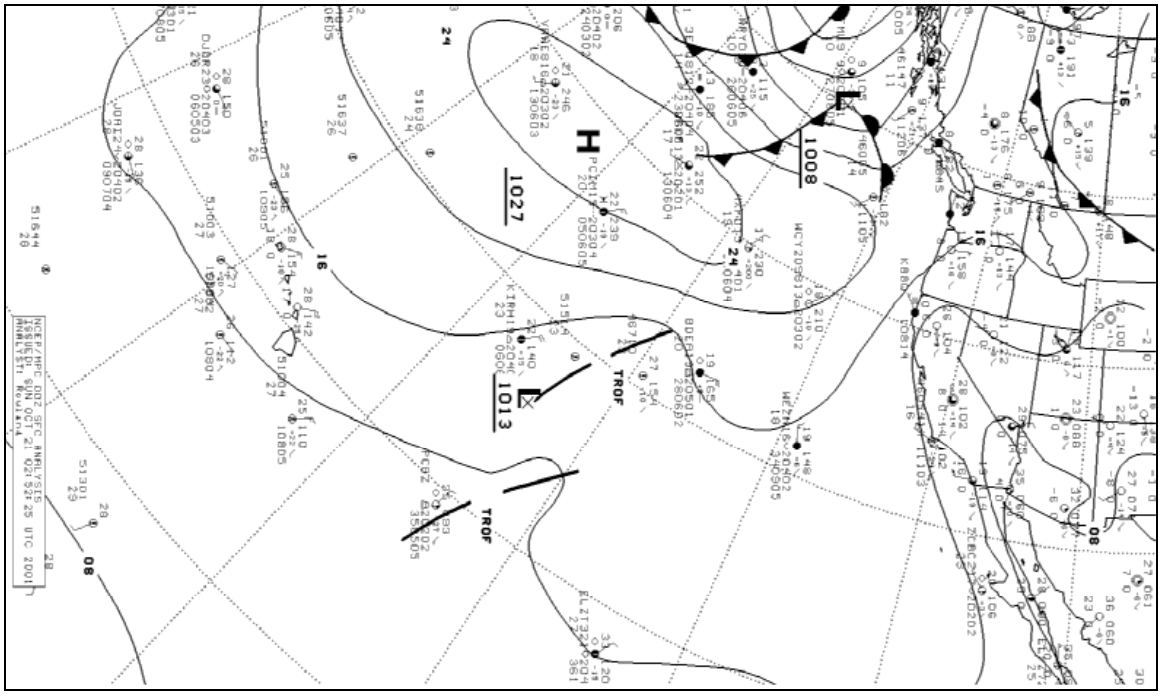

Figure 51. NCEP/MPC 00Z Surface Analysis, 21OCT01.

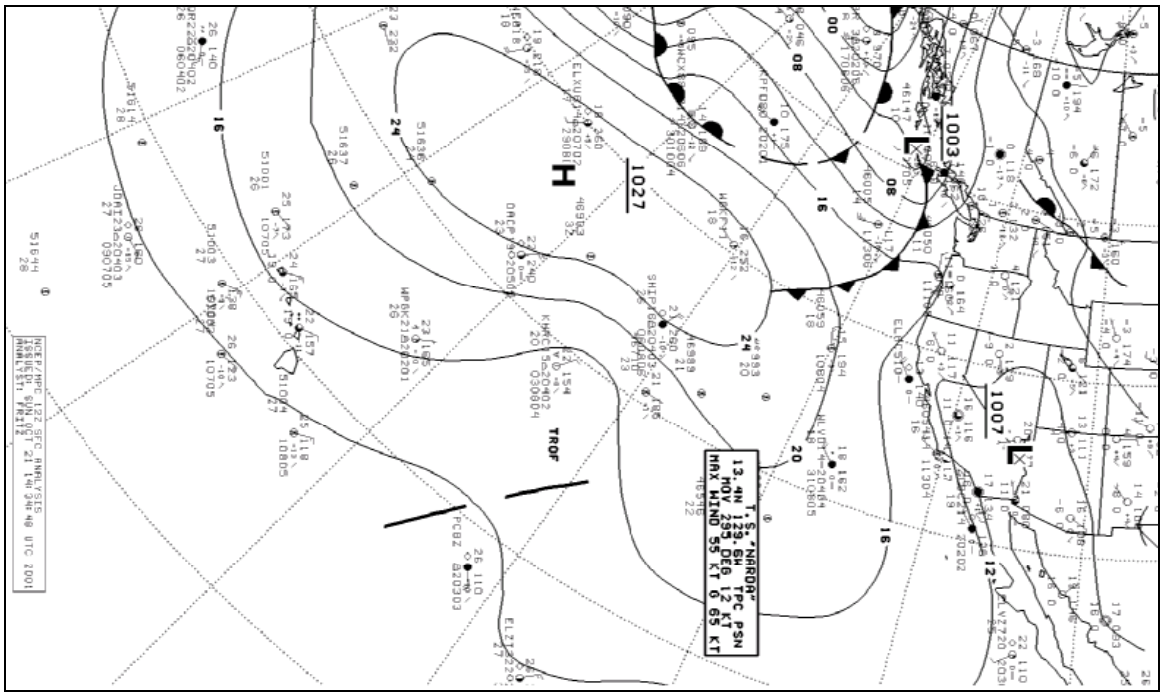

Figure 52. NCEP/MPC 12Z Surface Analysis, 21OCT01.

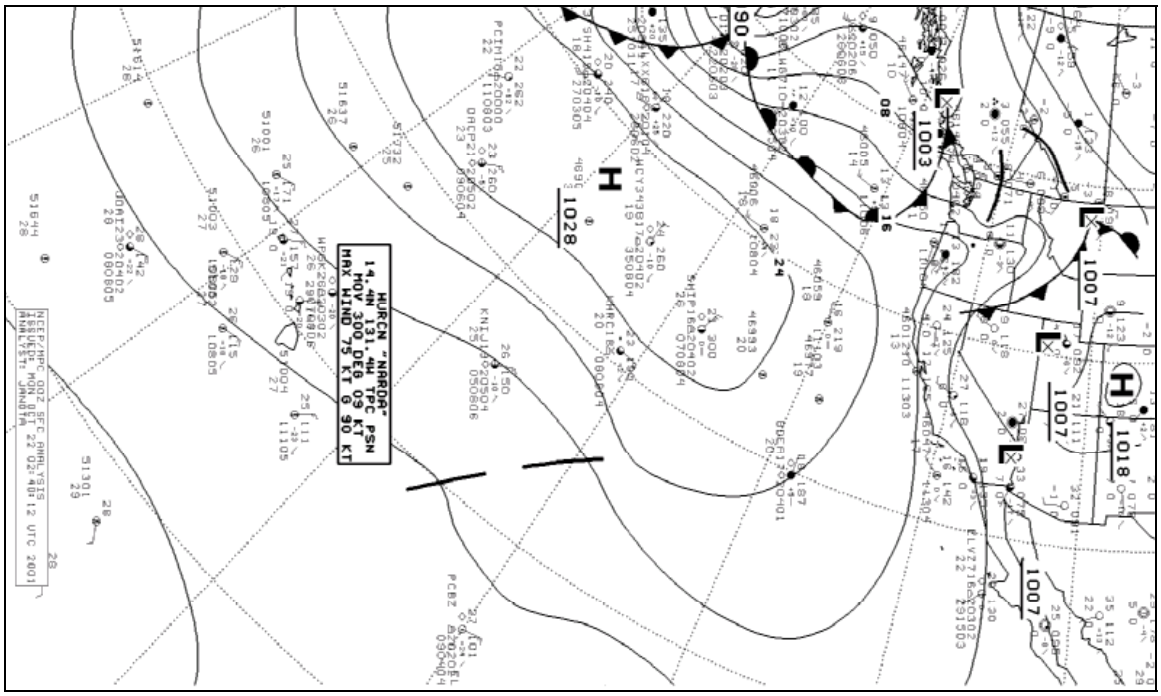

Figure 53. NCEP/MPC 00Z Surface Analysis, 22OCT01.

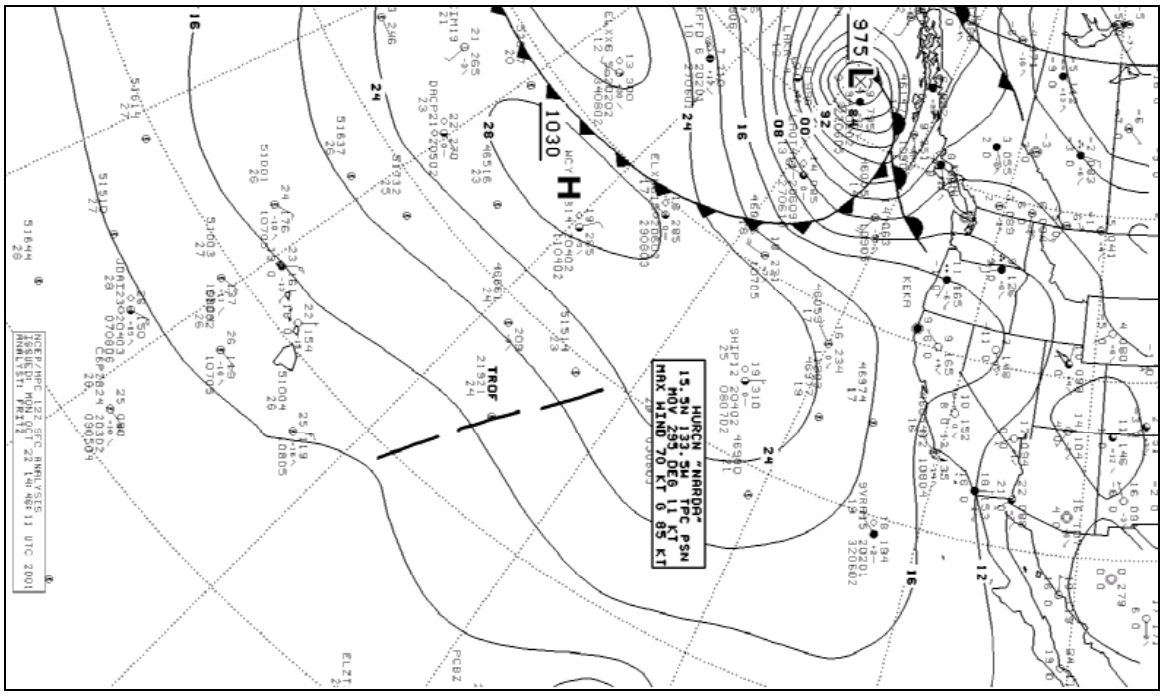

Figure 54. NCEP/MPC 12Z Surface Analysis, 22OCT01.

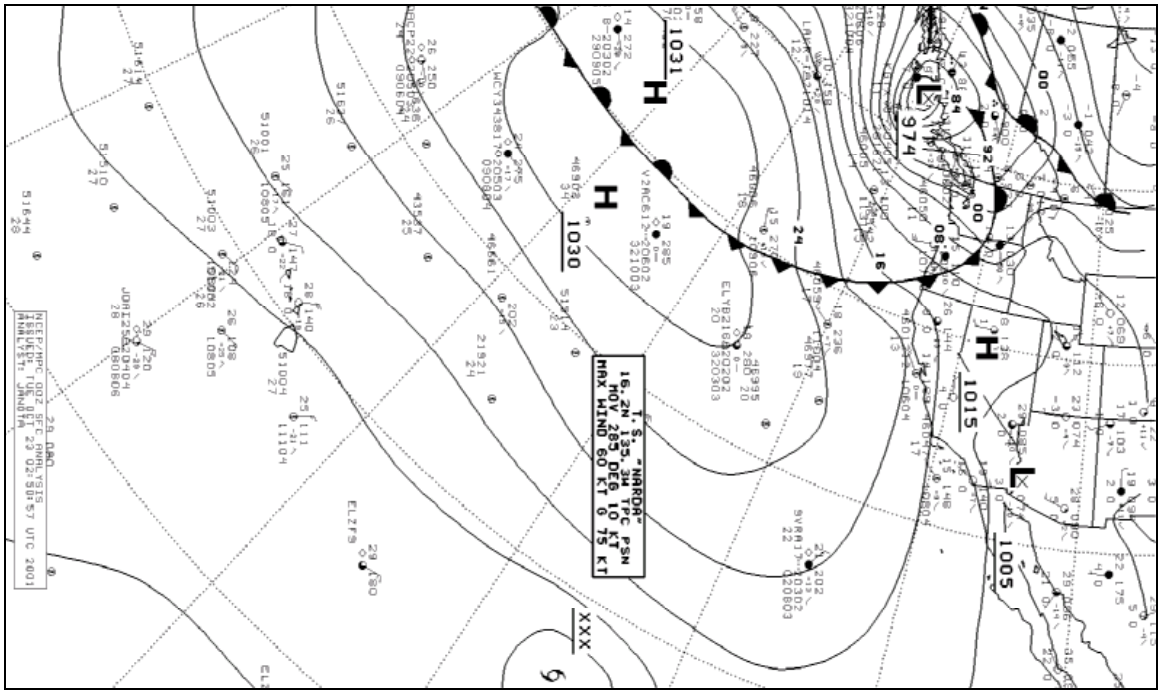

Figure 55. NCEP/MPC 00Z Surface Analysis, 23OCT01.

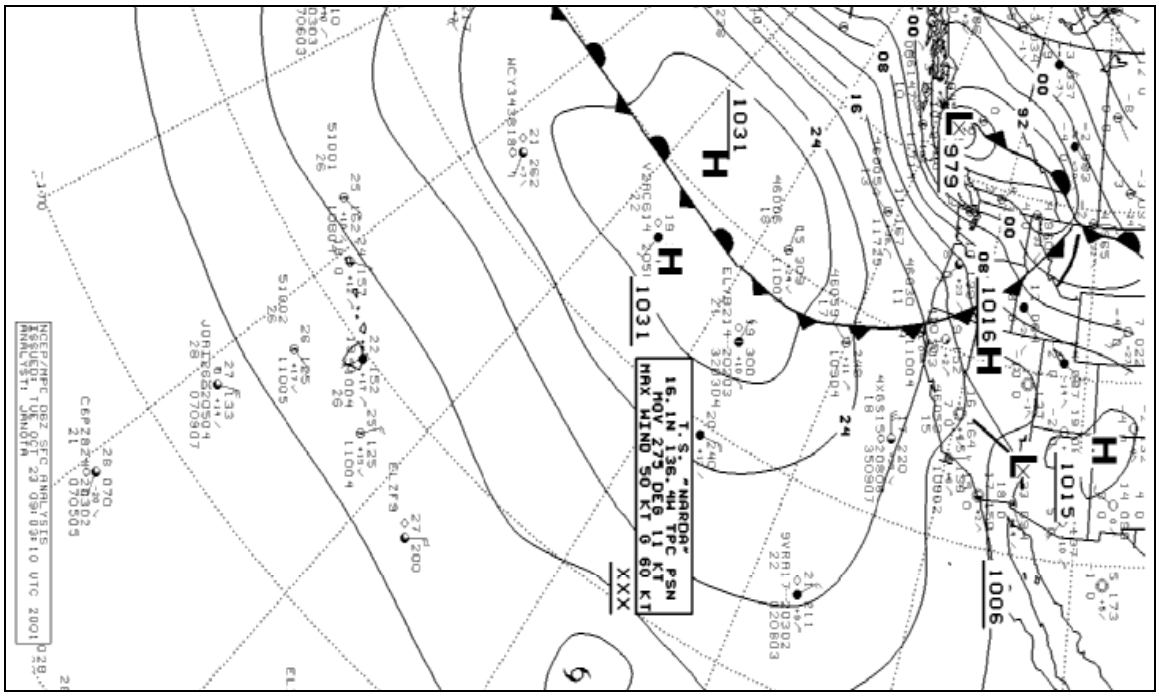

Figure 56. NCEP/MPC 06Z Surface Analysis, 23OCT01.

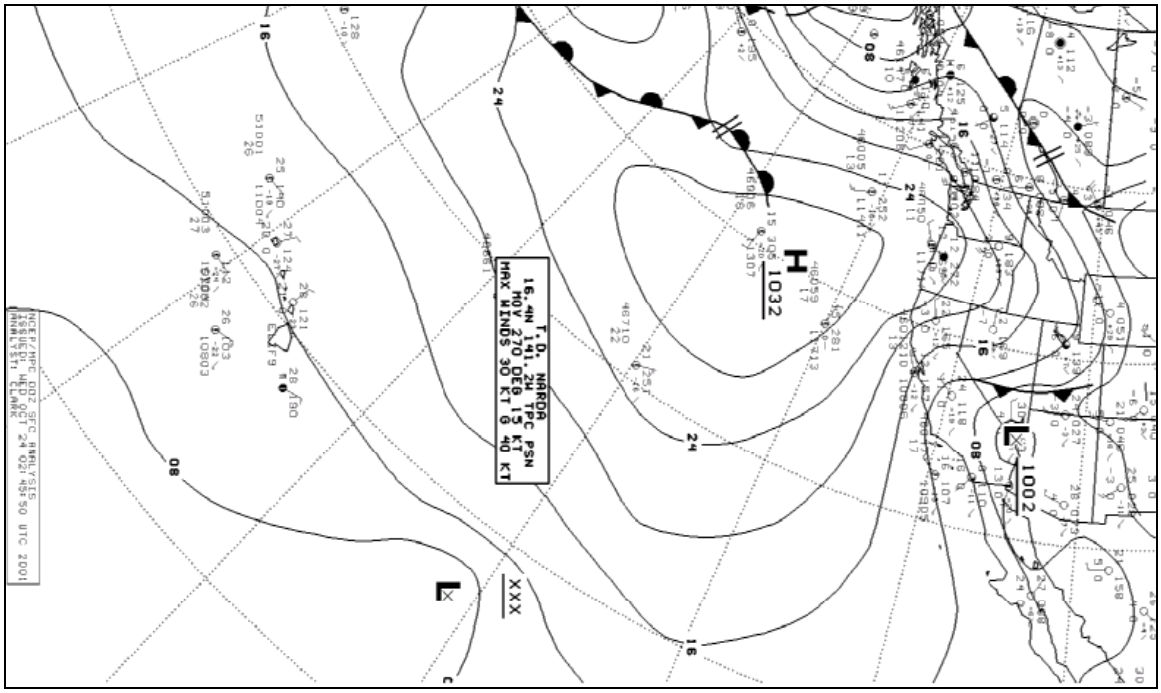

Figure 57. NCEP/MPC 00Z Surface Analysis, 24OCT01.

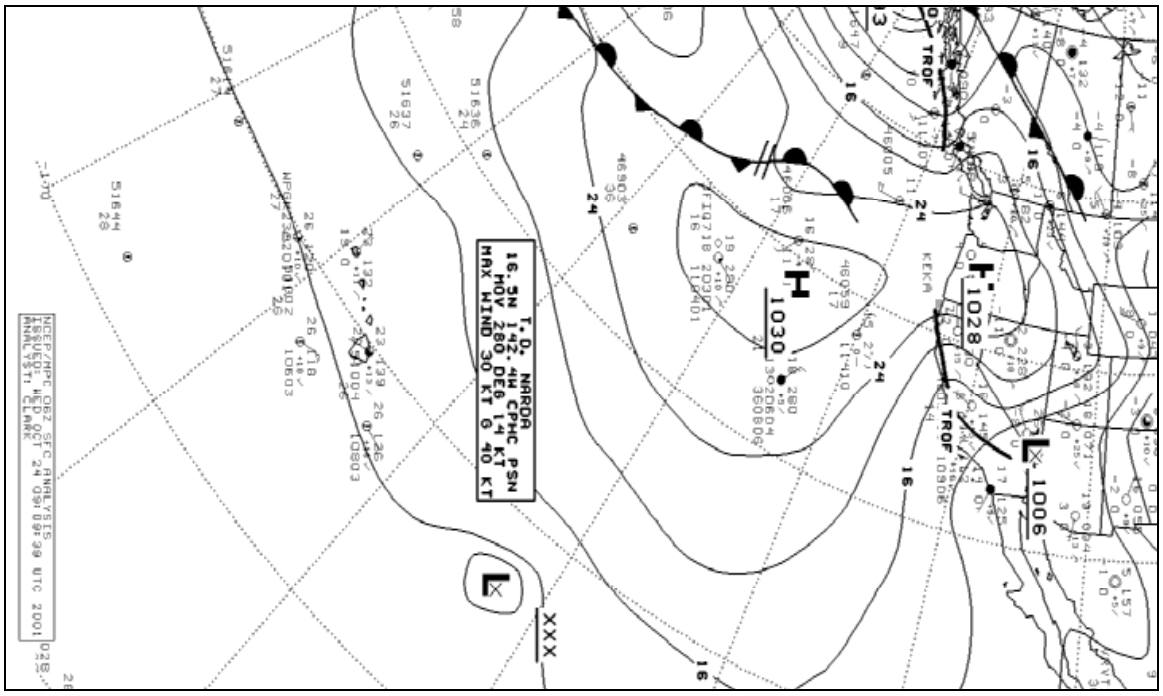

Figure 58. NCEP/MPC 06Z Surface Analysis, 24OCT01.

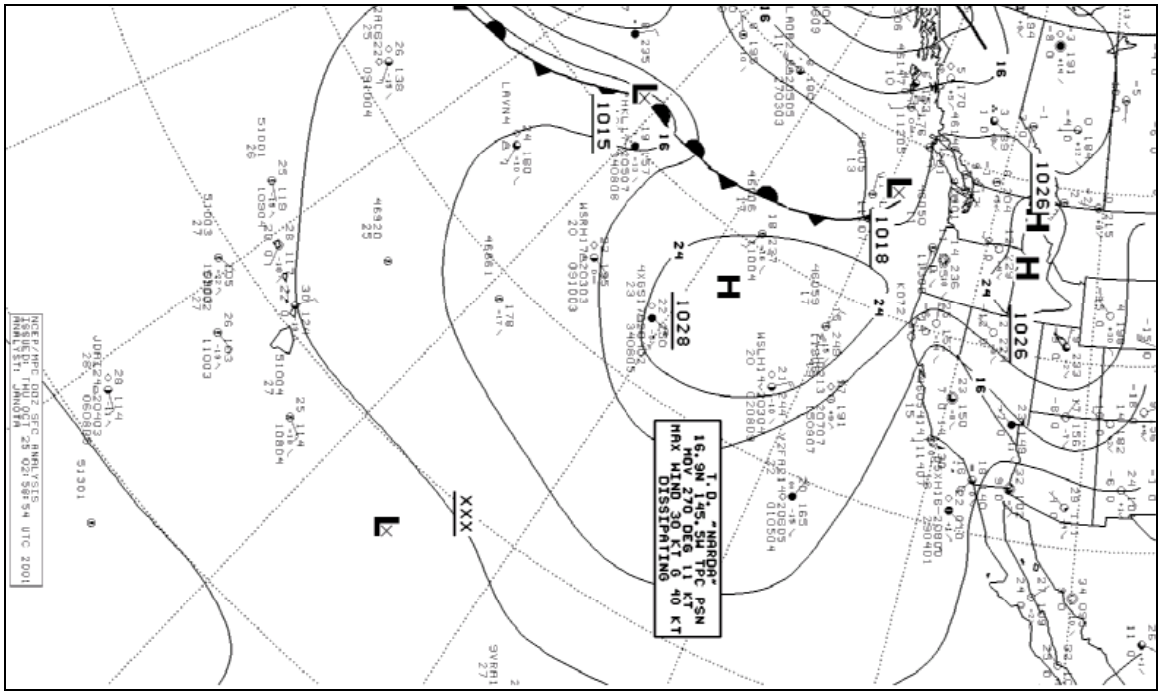

Figure 59. NCEP/MPC 00Z Surface Analysis, 25OCT01.

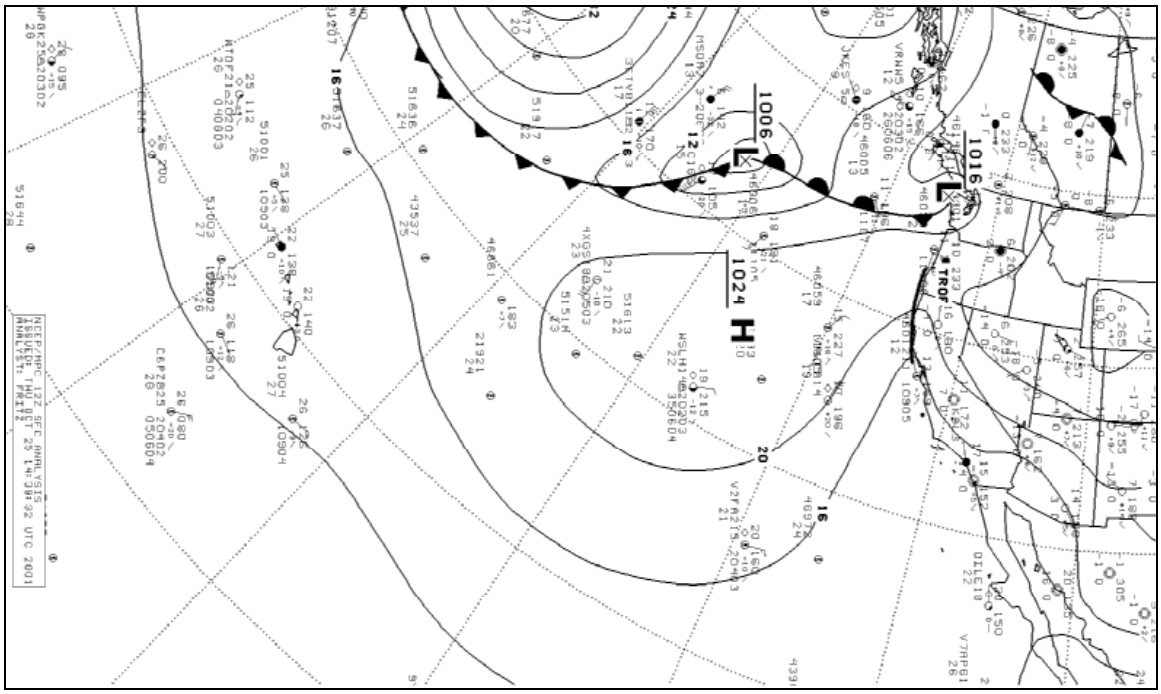

Figure 60. NCEP/MPC 12Z Surface Analysis, 25OCT01.

2. March 2002

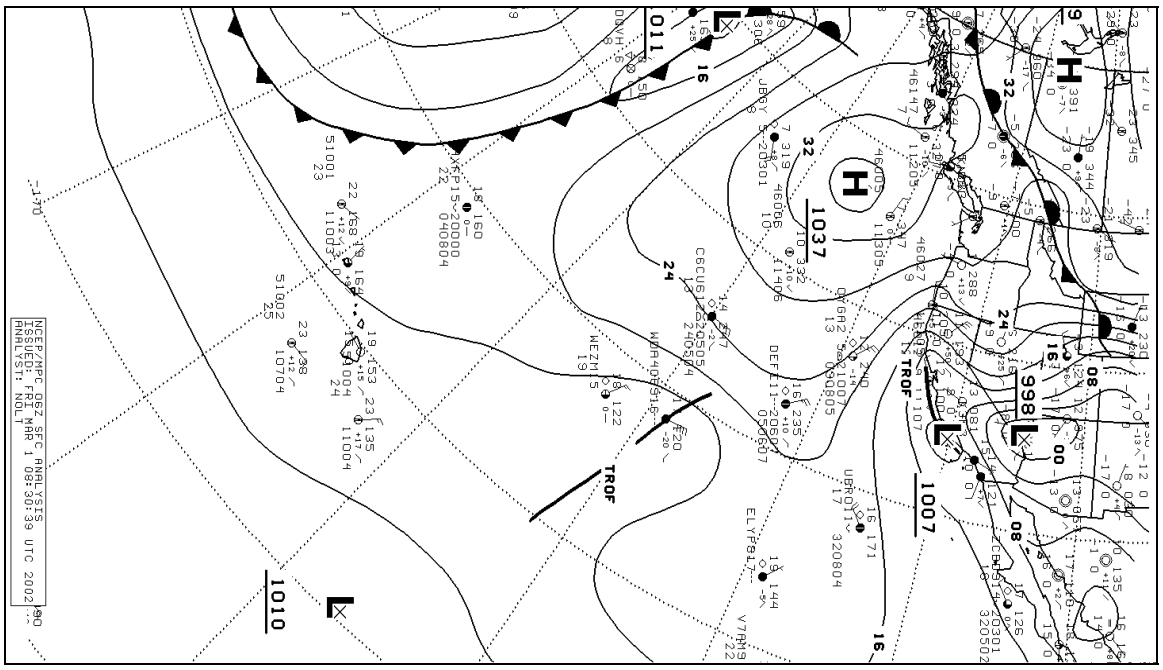

Figure 61. NCEP/MPC 06Z Surface Analysis, 01MAR02.

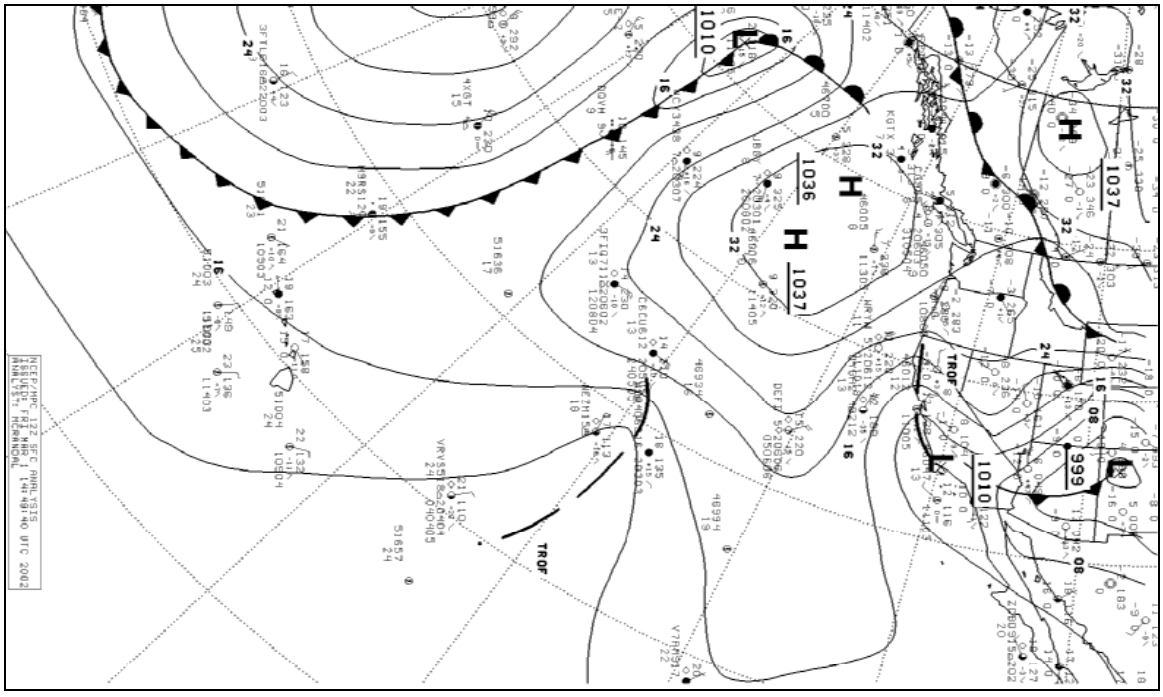

Figure 62. NCEP/MPC 12Z Surface Analysis, 01MAR02.

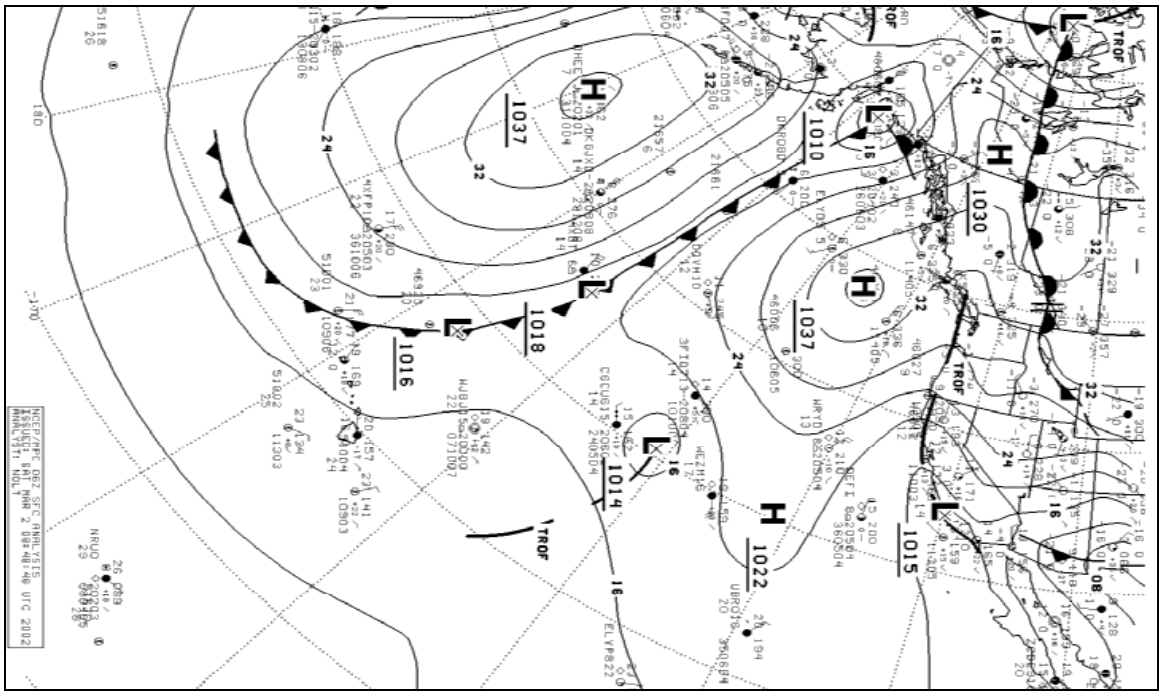

Figure 63. NCEP/MPC 06Z Surface Analysis, 02MAR02.

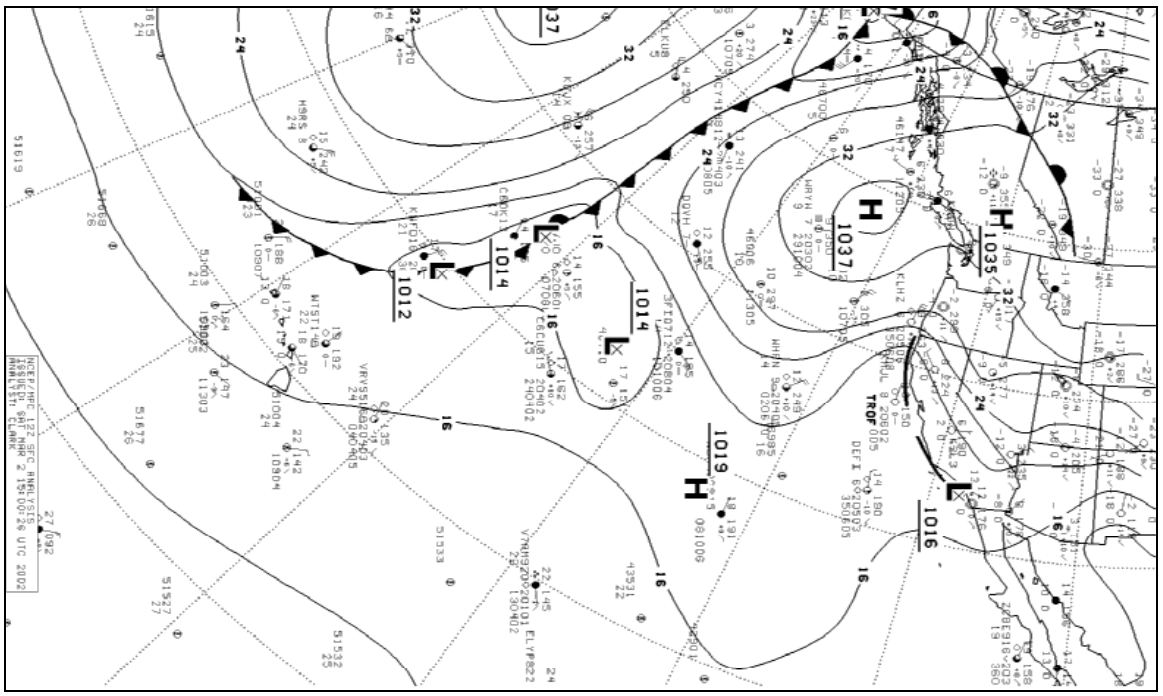

Figure 64. NCEP/MPC 12Z Surface Analysis, 02MAR02.

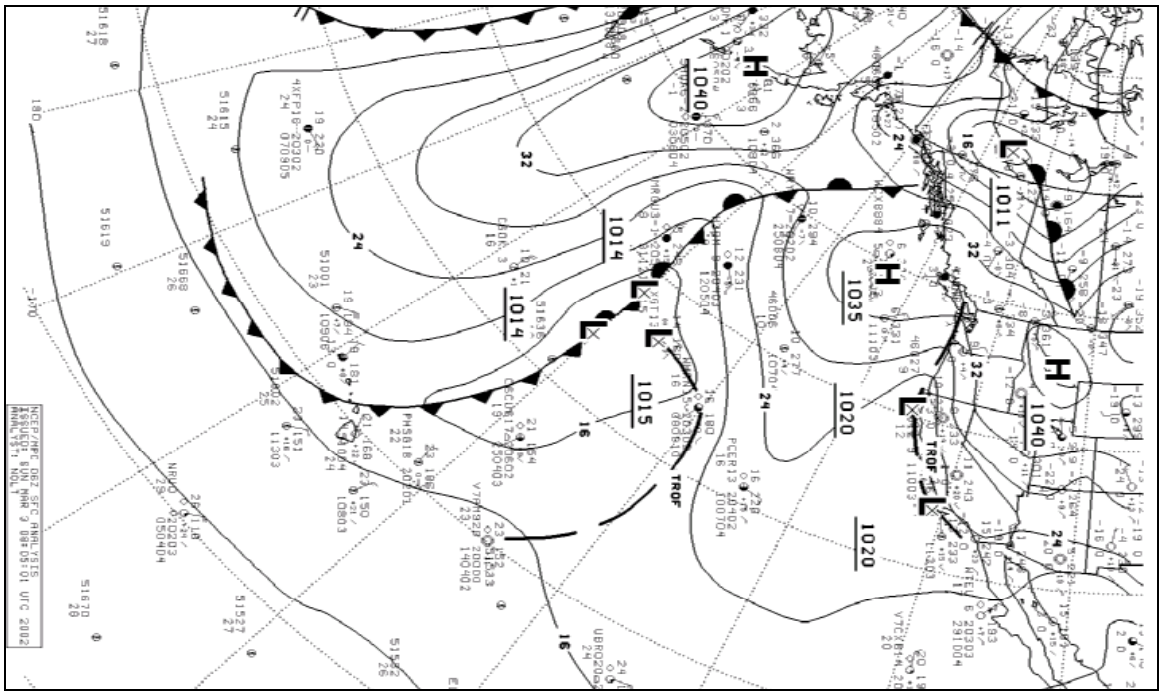

Figure 65. NCEP/MPC 06Z Surface Analysis, 03MAR02.

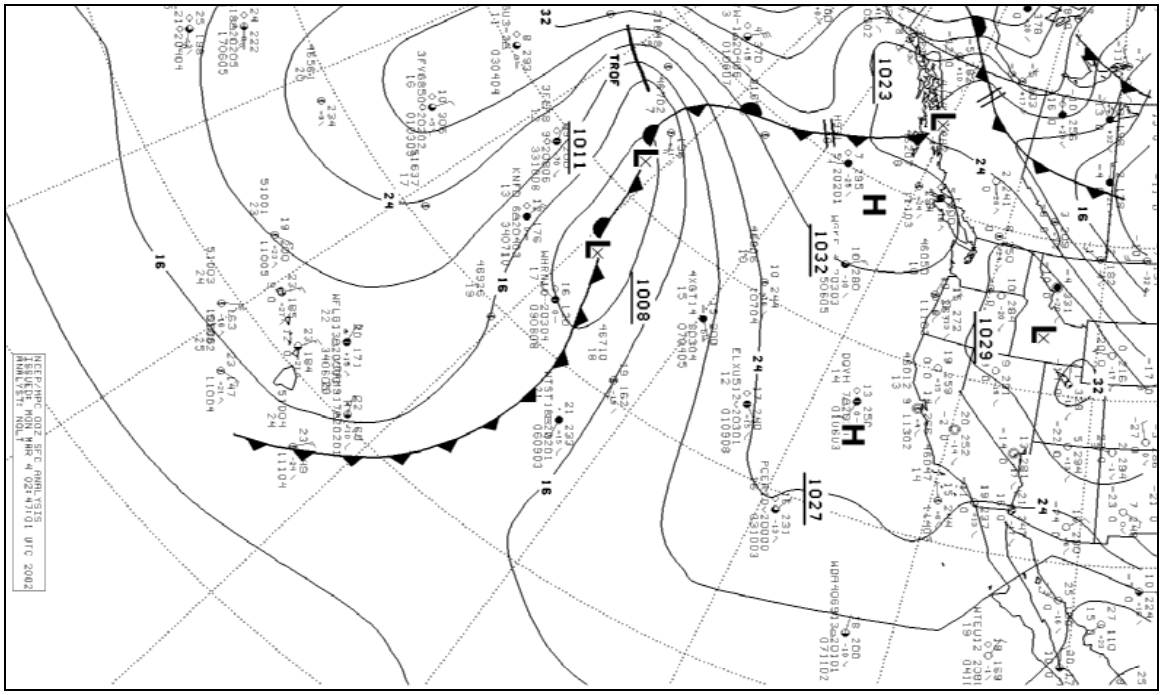

Figure 66. NCEP/MPC 00Z Surface Analysis, 04MAR02.

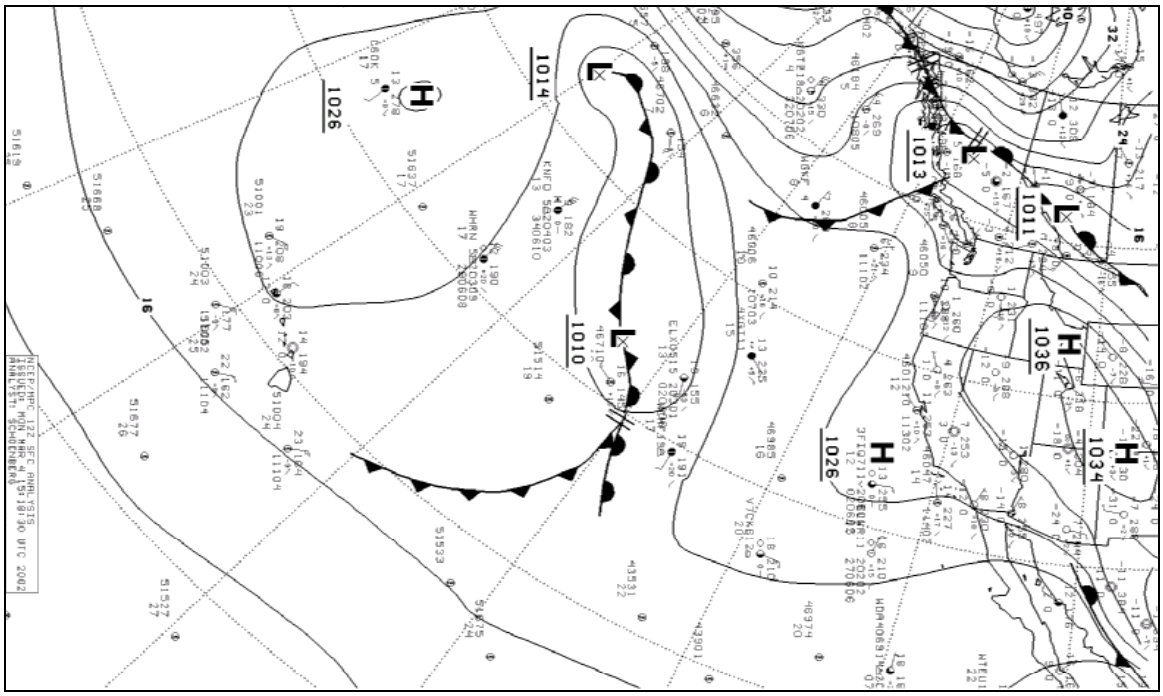

Figure 67. NCEP/MPC 12Z Surface Analysis, 04MAR02.

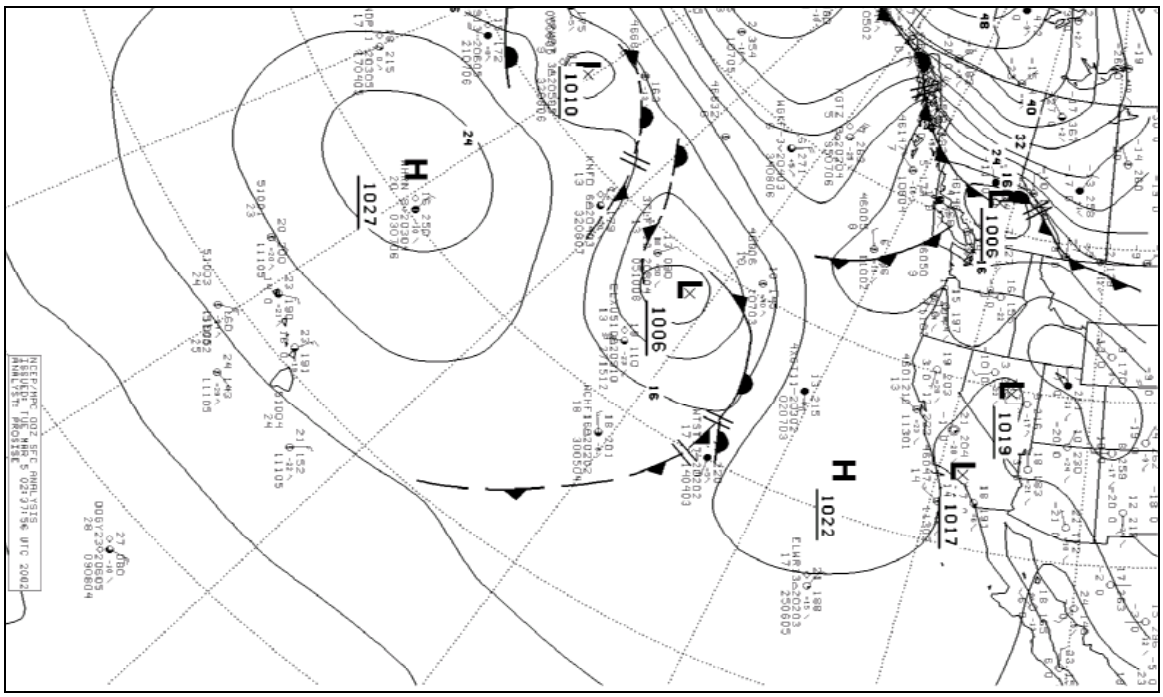

Figure 68. NCEP/MPC 00Z Surface Analysis, 05MAR02.

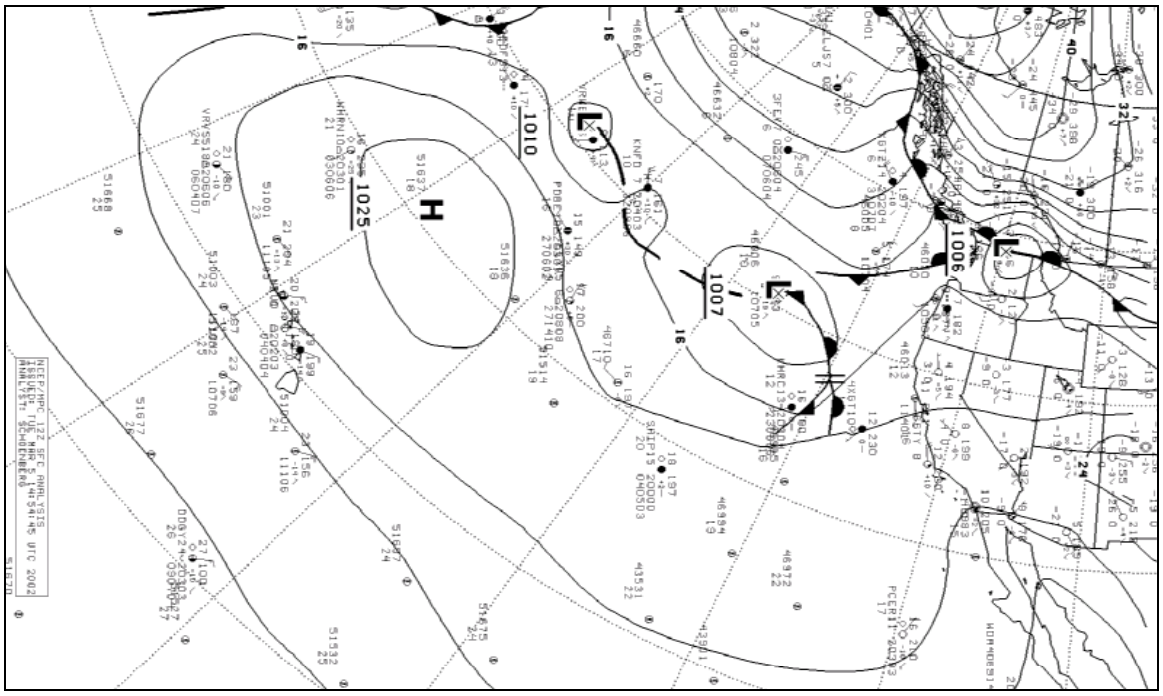

Figure 69. NCEP/MPC 12Z Surface Analysis, 05MAR02.

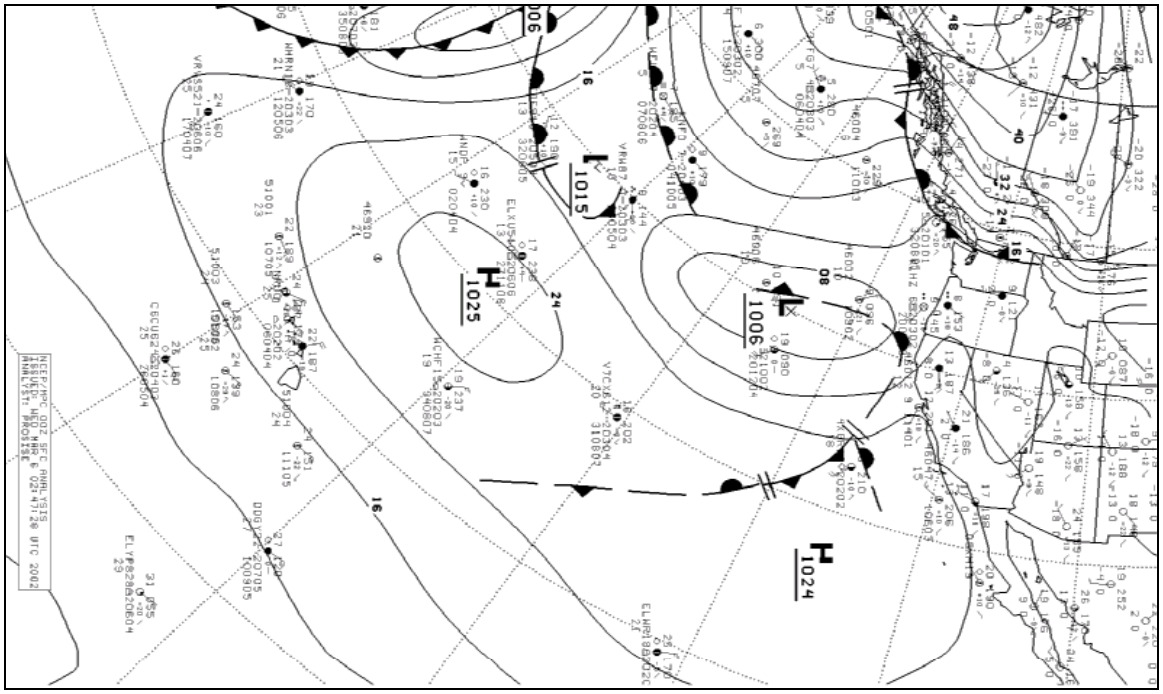

Figure 70. NCEP/MPC 00Z Surface Analysis, 06MAR02.

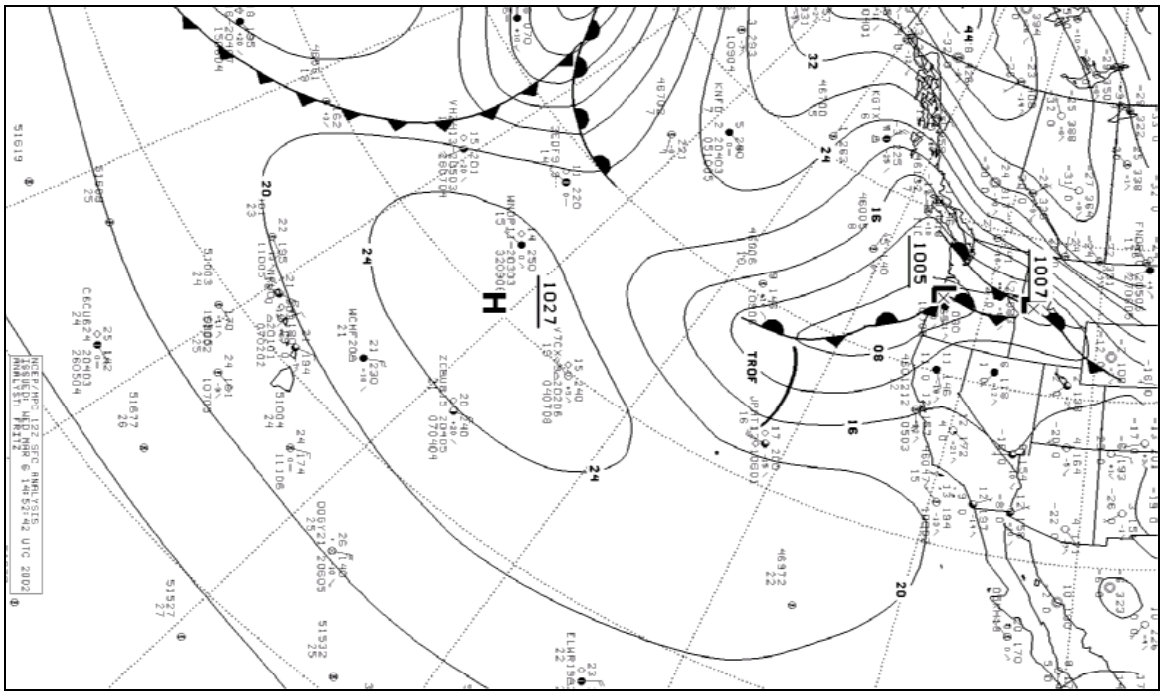

Figure 71. NCEP/MPC 12Z Surface Analysis, 06MAR02.

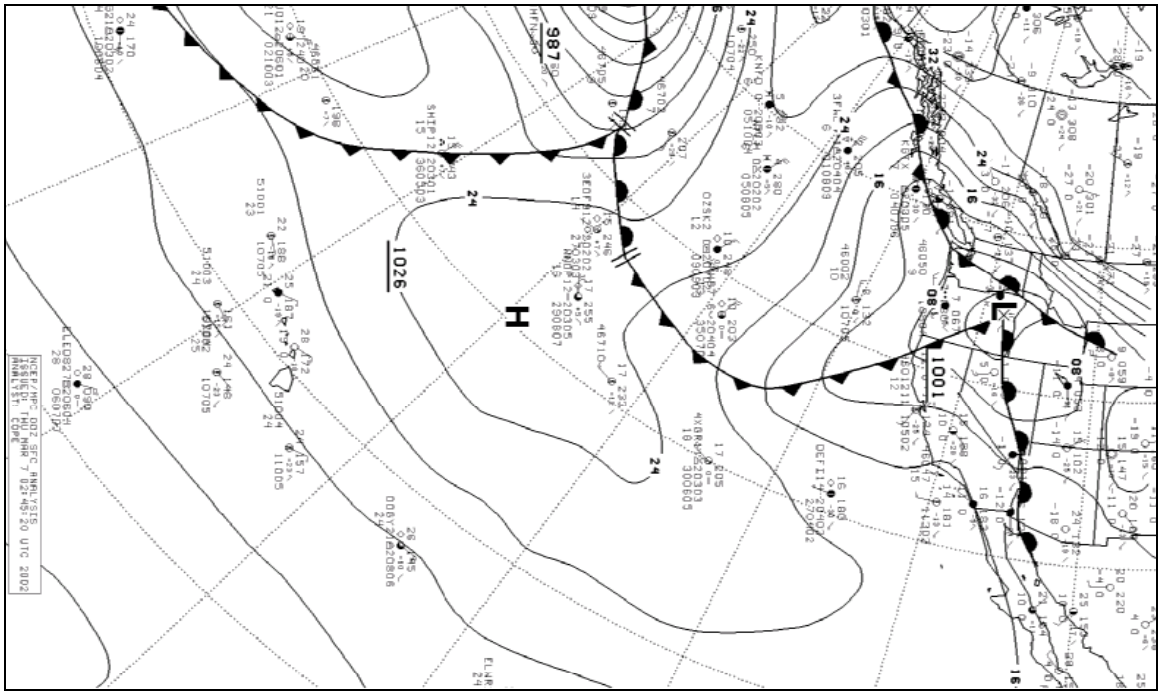

Figure 72. NCEP/MPC 00Z Surface Analysis, 07MAR02.

THIS PAGE INTENTIONALLY LEFT BLANK

APPENDIX B. SATELLITE IMAGERY

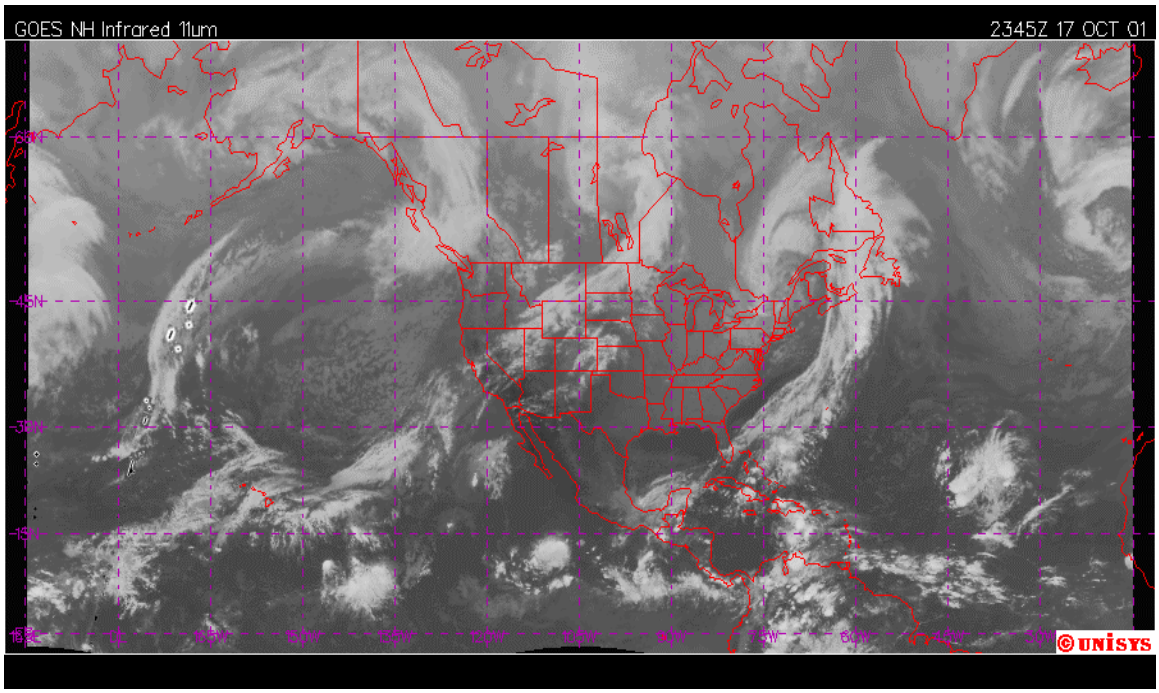

Figure 73. GOES IR Composite 00Z, 18OCT01.

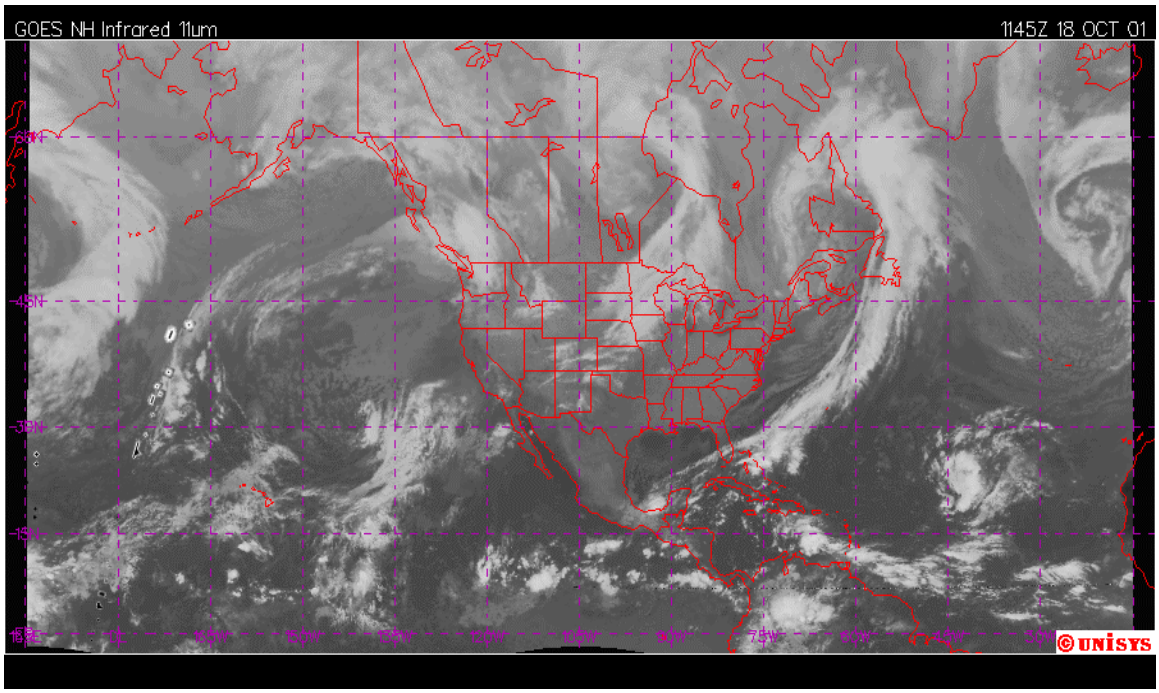

Figure 74. GOES IR Composite 12Z, 18OCT01.

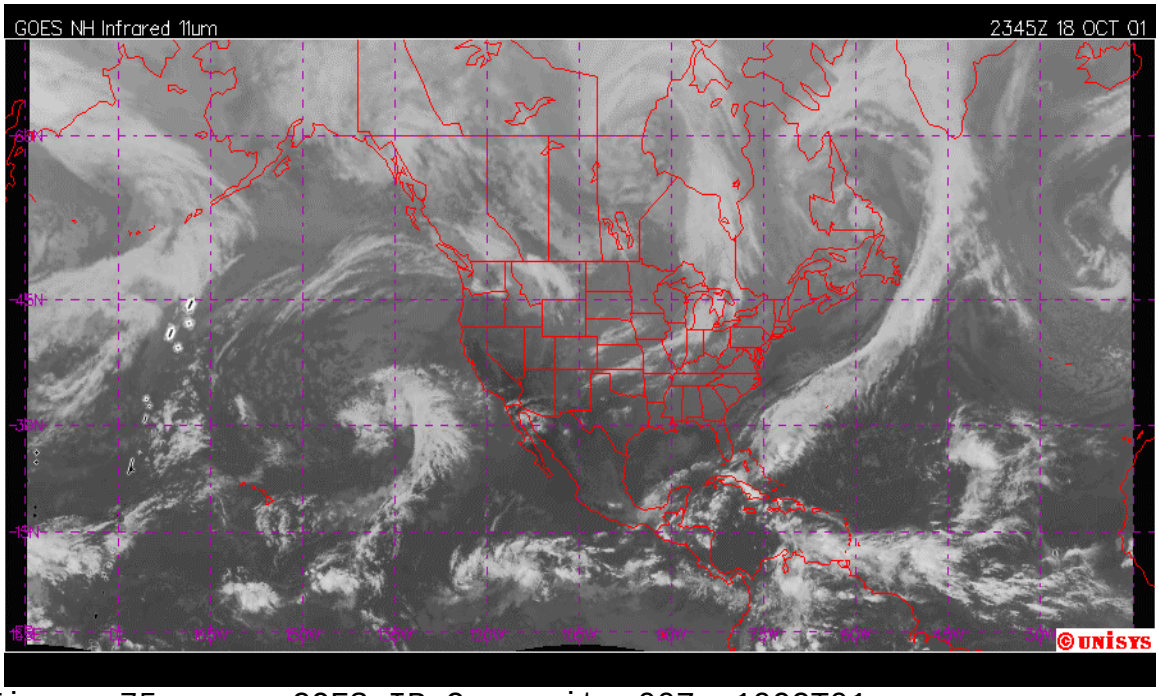

Figure 75. GOES IR Composite 00Z, 19OCT01.

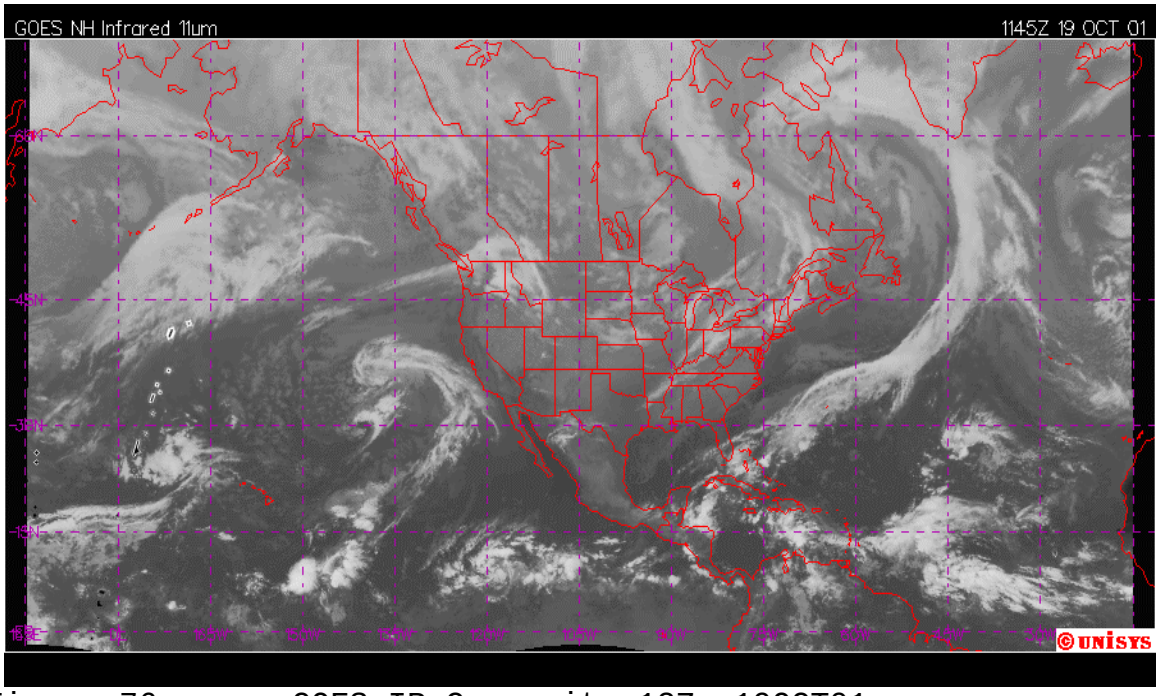

Figure 76. GOES IR Composite 12Z, 19OCT01.

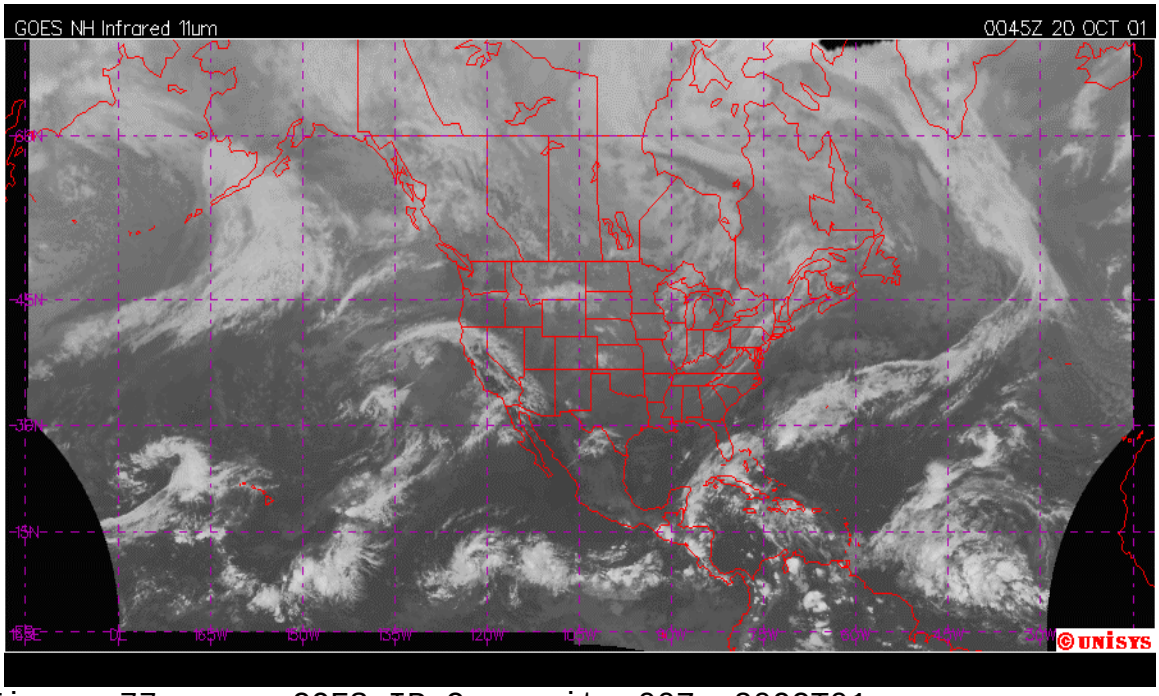

Figure 77. GOES IR Composite 00Z, 20OCT01.

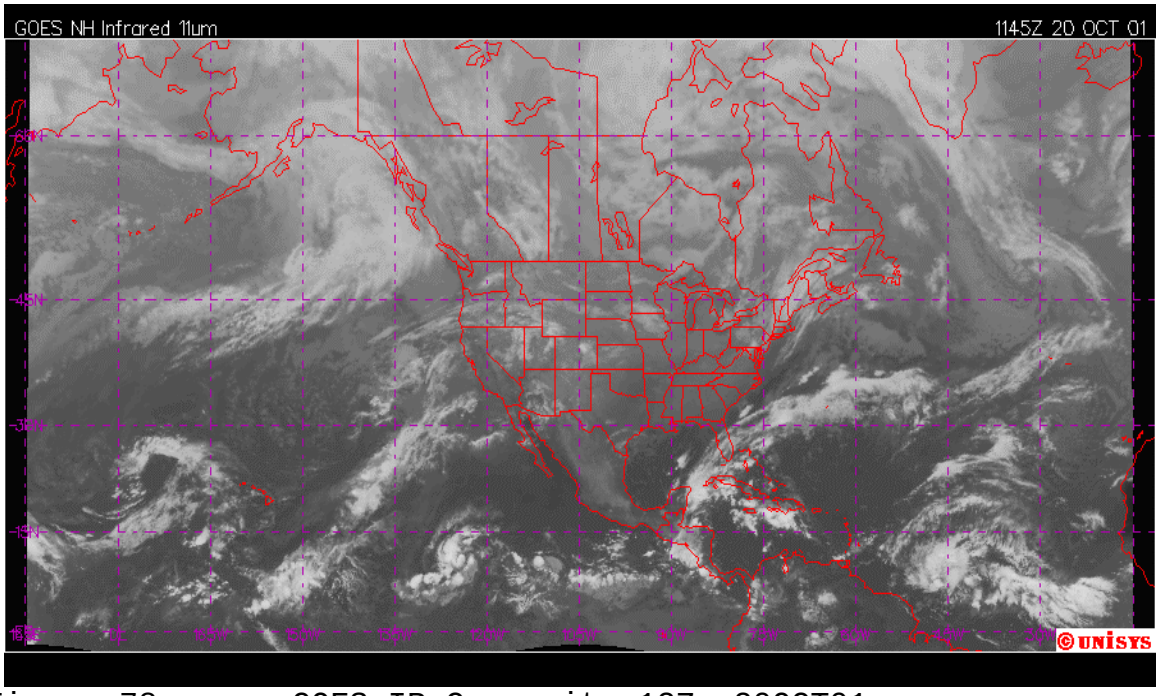

Figure 78. GOES IR Composite 12Z, 20OCT01.

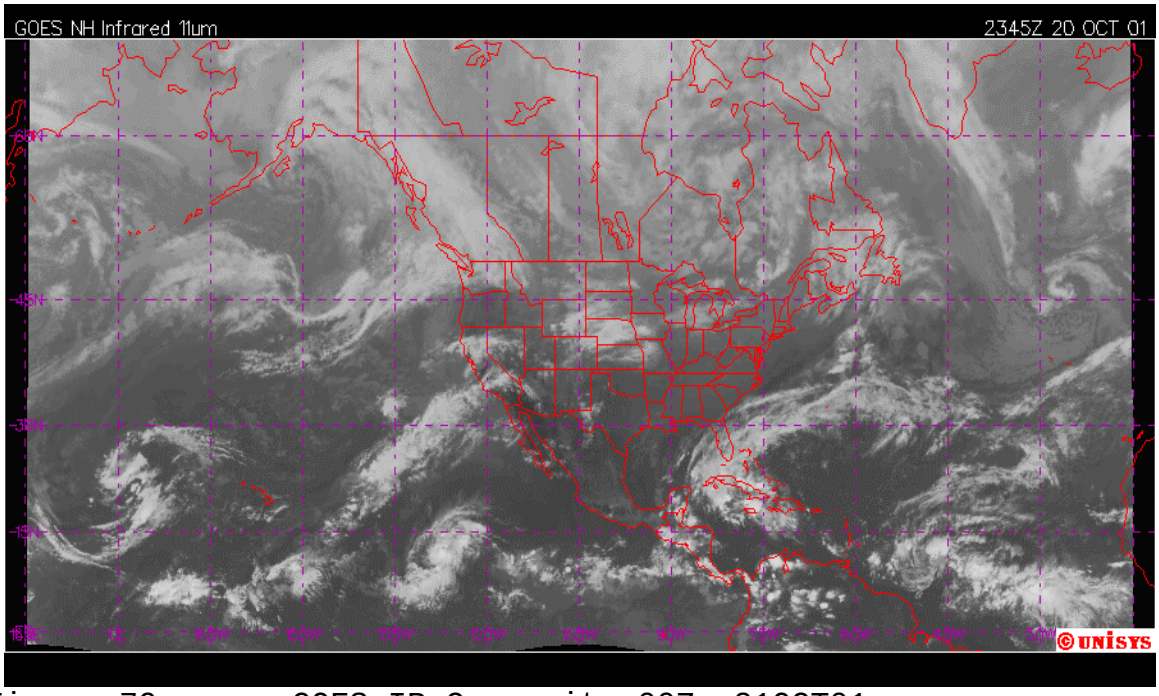

Figure 79. GOES IR Composite 00Z, 21OCT01.

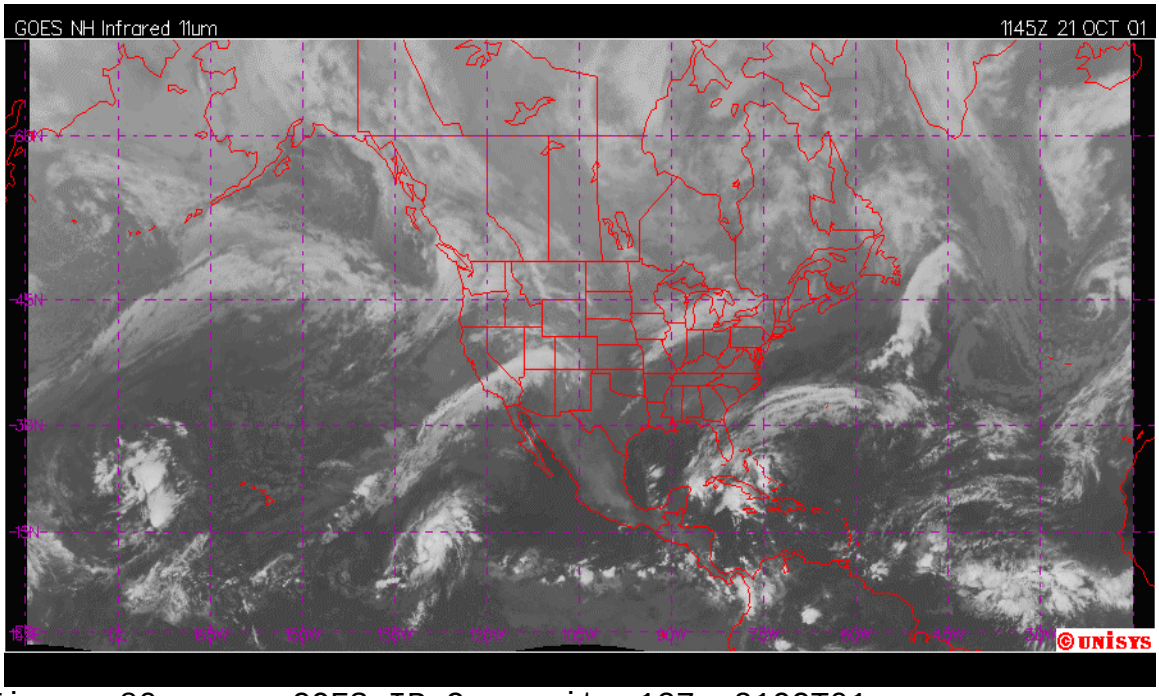

Figure 80. GOES IR Composite 12Z, 21OCT01.

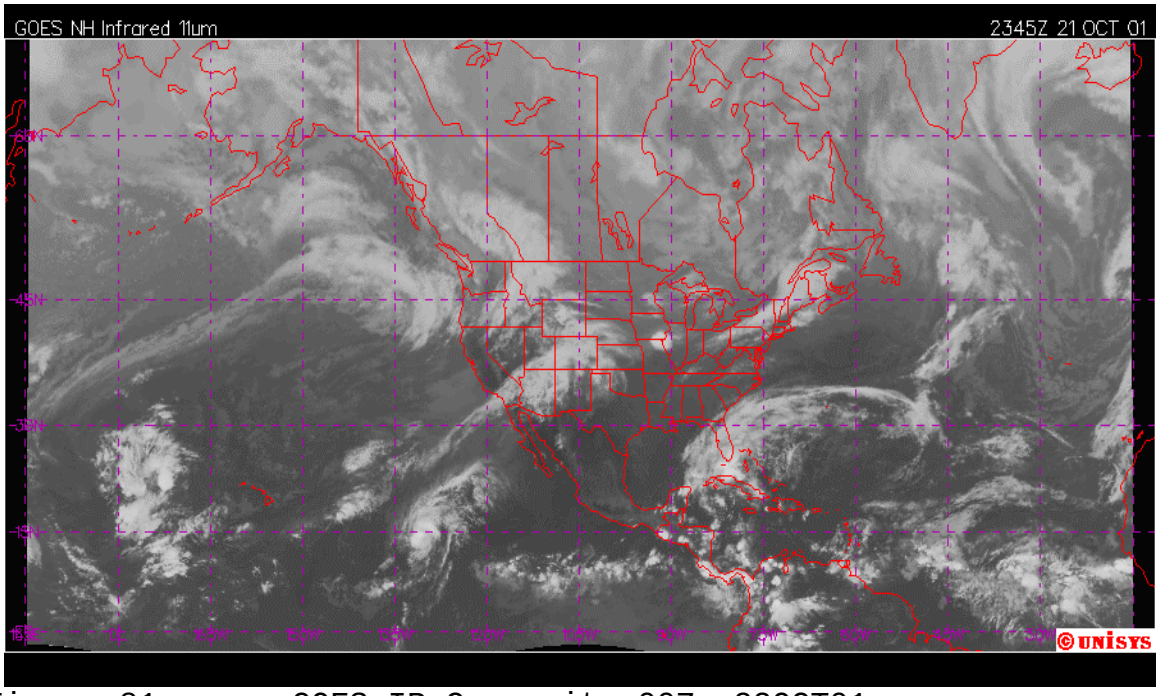

Figure 81. GOES IR Composite 00Z, 22OCT01.

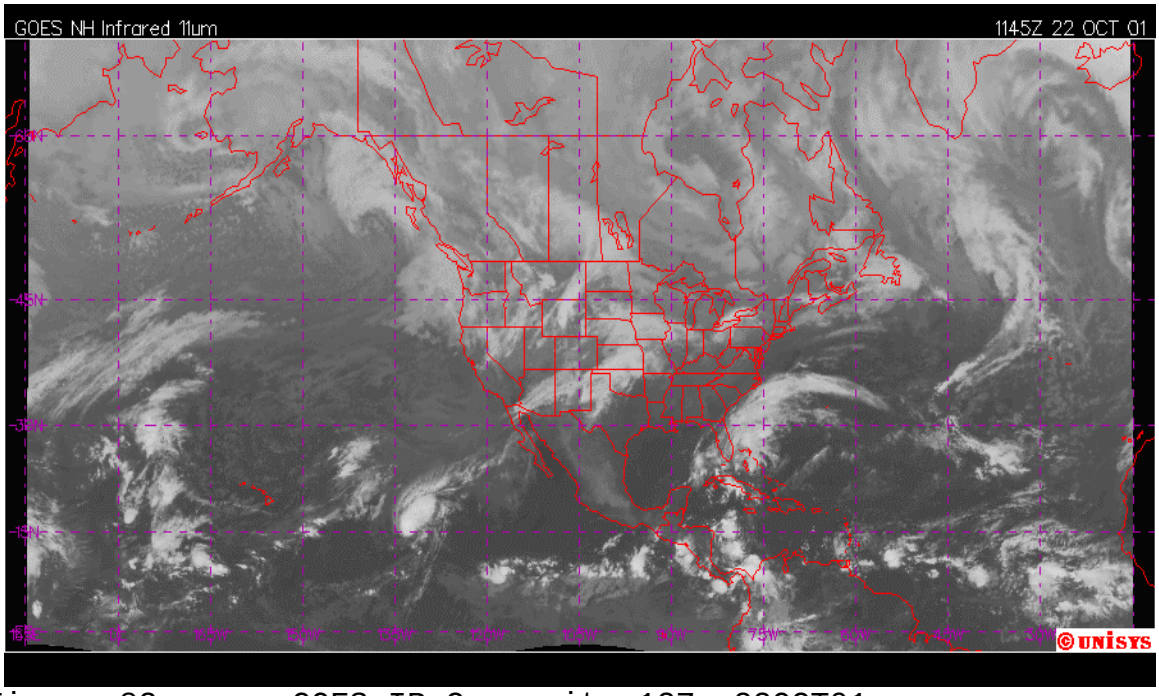

Figure 82. GOES IR Composite 12Z, 22OCT01.

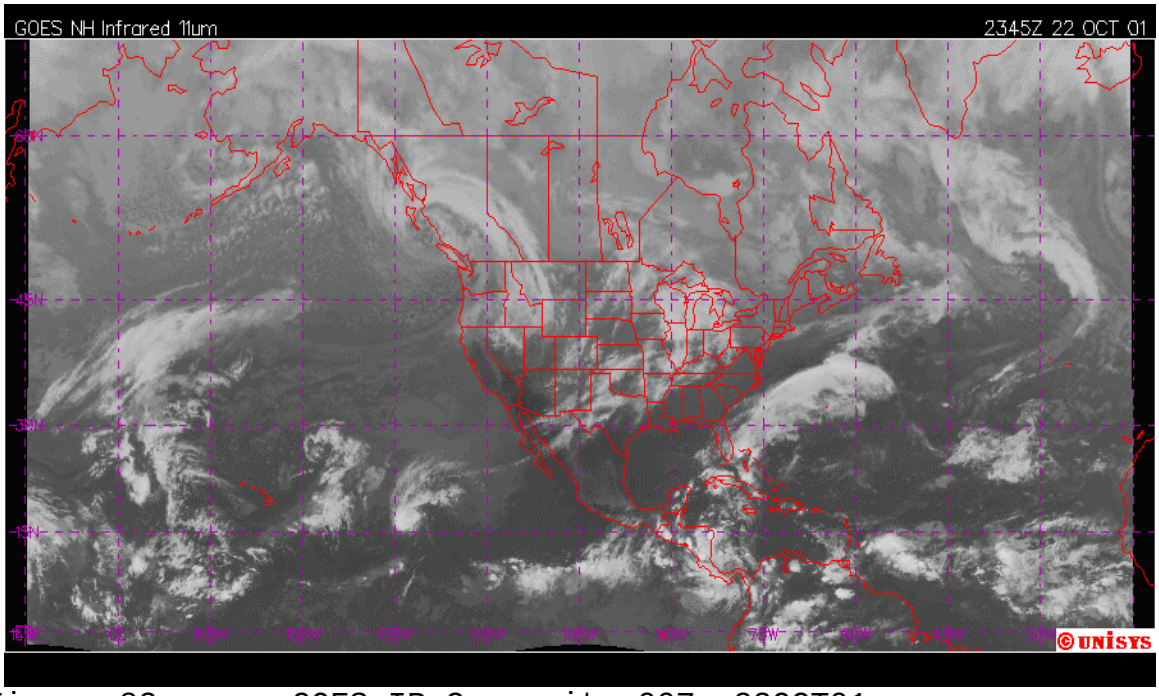

Figure 83. GOES IR Composite 00Z, 23OCT01.

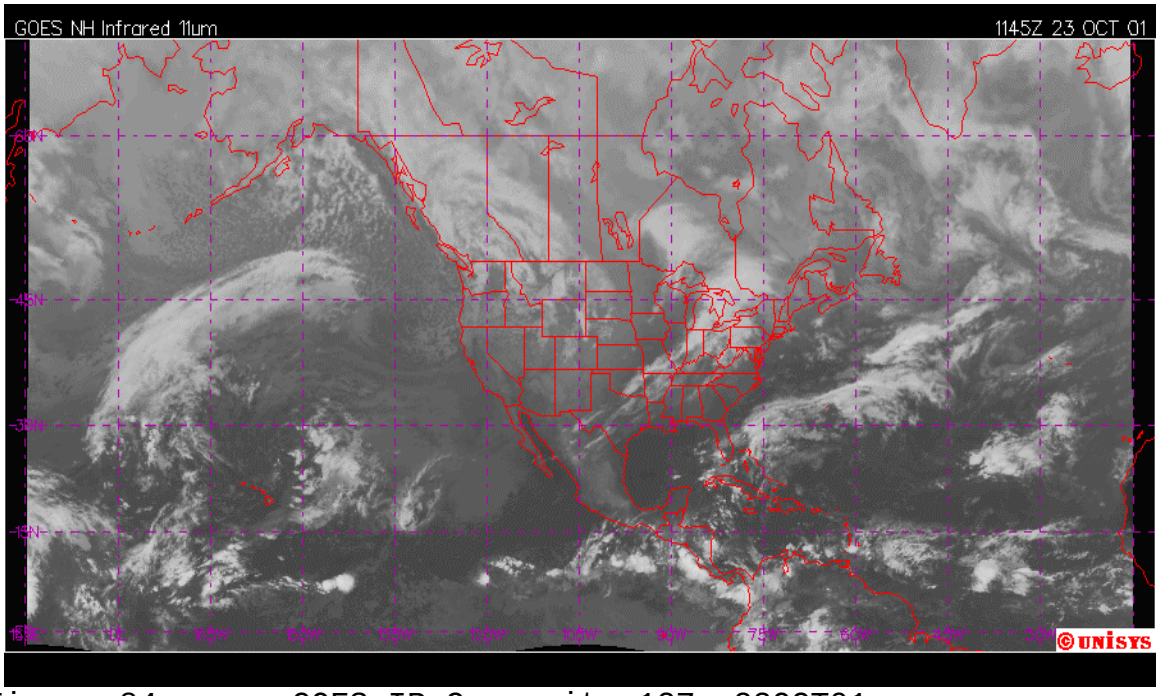

Figure 84. GOES IR Composite 12Z, 23OCT01.

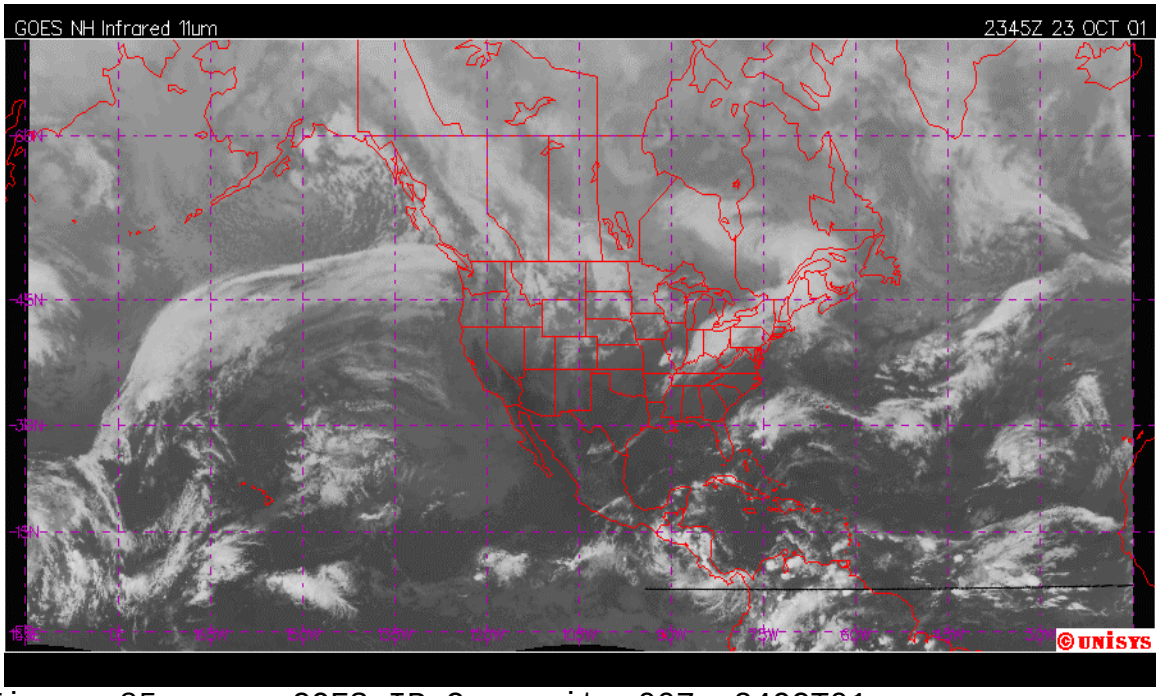

Figure 85. GOES IR Composite 00Z, 24OCT01.

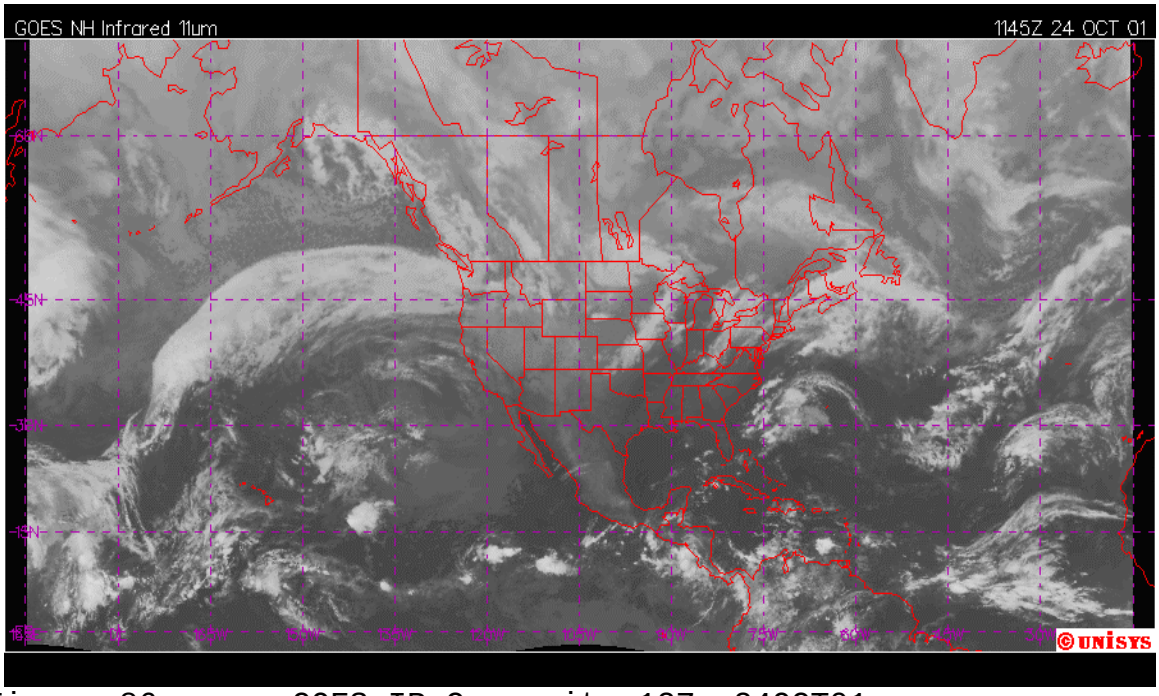

Figure 86. GOES IR Composite 12Z, 24OCT01.

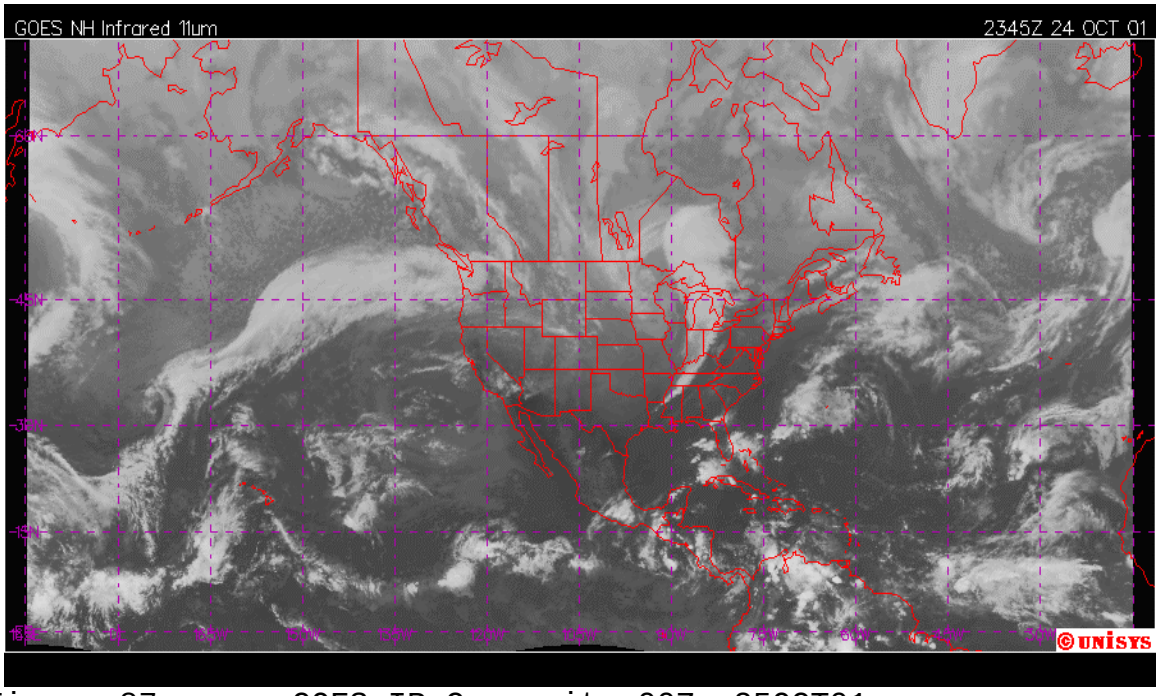

Figure 87. GOES IR Composite 00Z, 25OCT01.

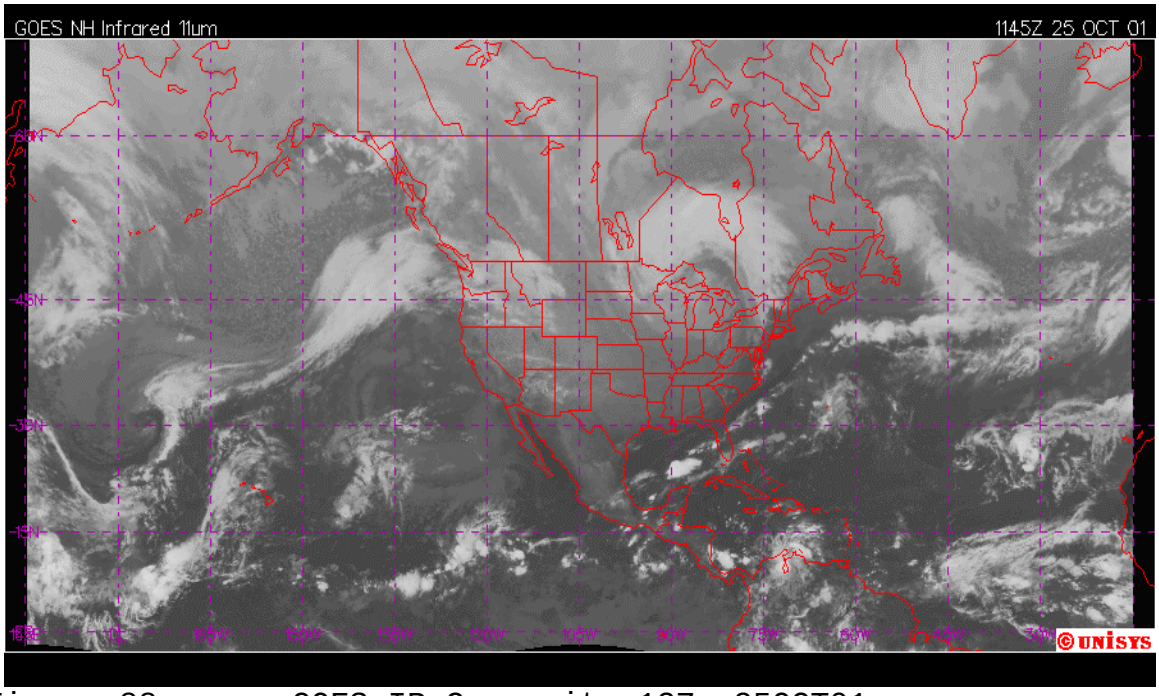

Figure 88. GOES IR Composite 12Z, 25OCT01.

APPENDIX C. COAMPS 81 KM RESOLUTION MODEL

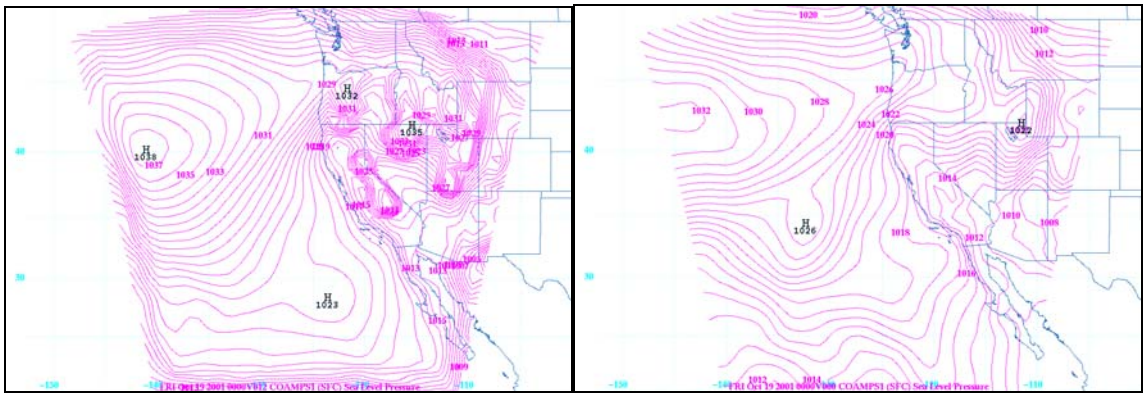

Figure 89. COAMPS forecast (left) and analysis (right) valid for 00Z, 19OCT01.

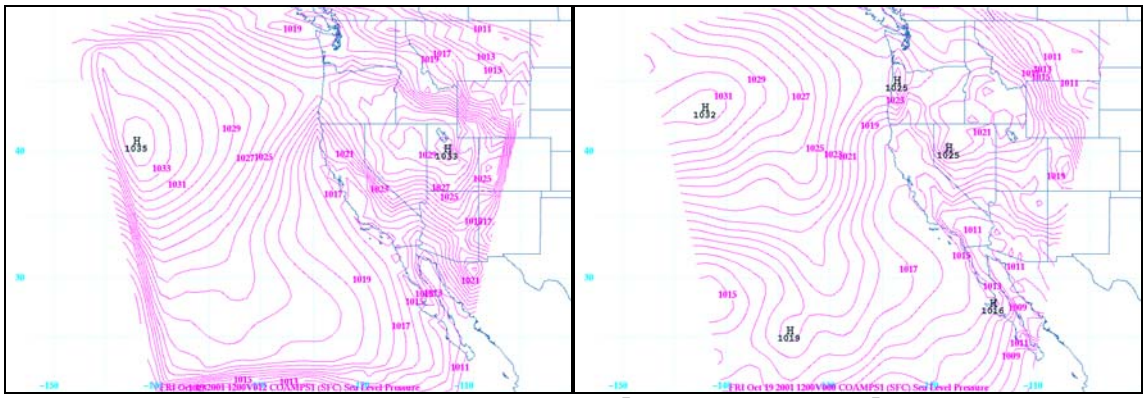

Figure 90. COAMPS forecast (left) and analysis (right) valid for 12Z, 19OCT01.

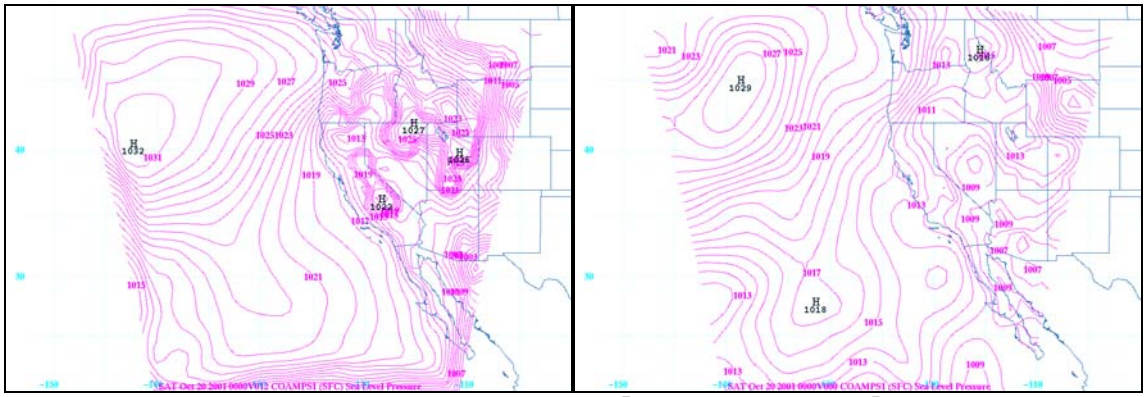

Figure 91. COAMPS forecast (left) and analysis (right) valid for 00Z, 20OCT01.

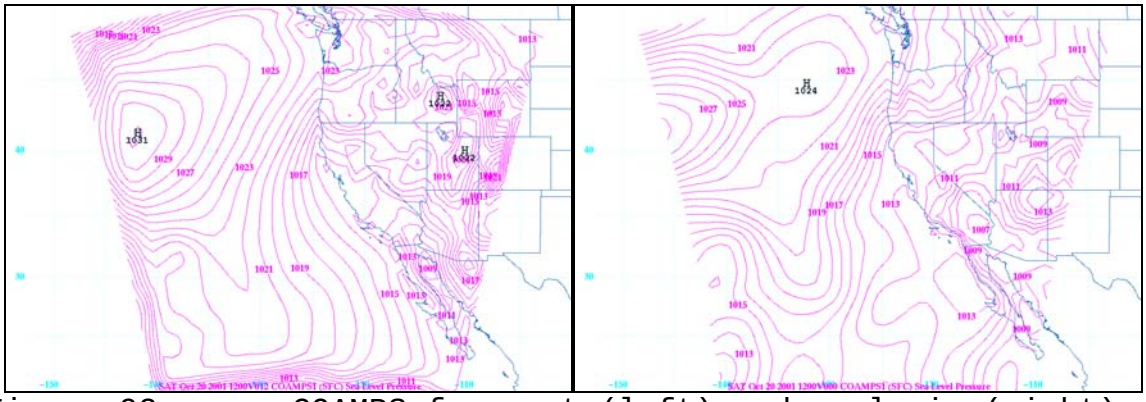

Figure 92. COAMPS forecast (left) and analysis (right) valid for 12Z, 20OCT01.

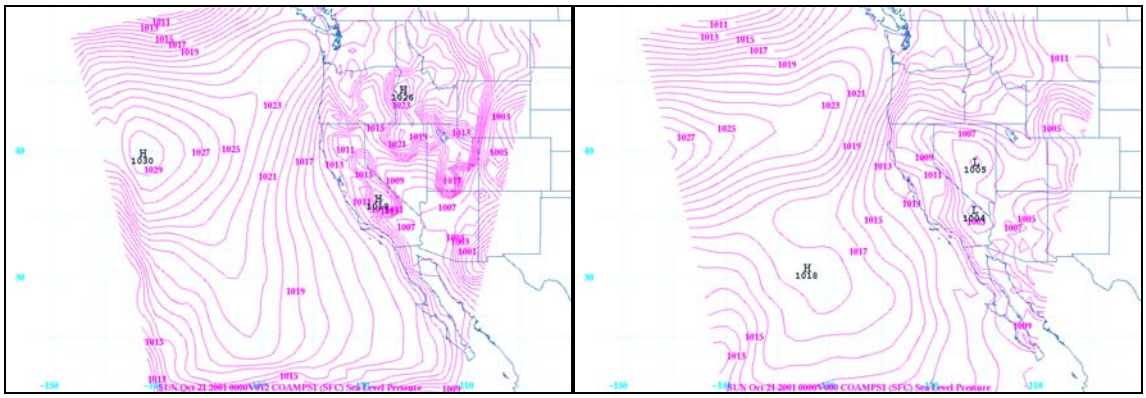

Figure 93. COAMPS forecast (left) and analysis (right) valid for 00Z, 21OCT01.

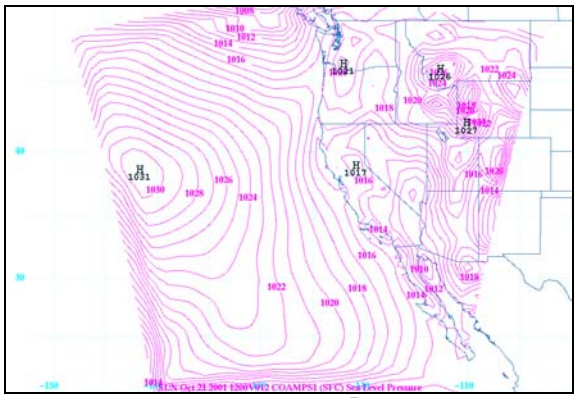

Figure 94. COAMPS forecast valid for 12Z, 21OCT01.

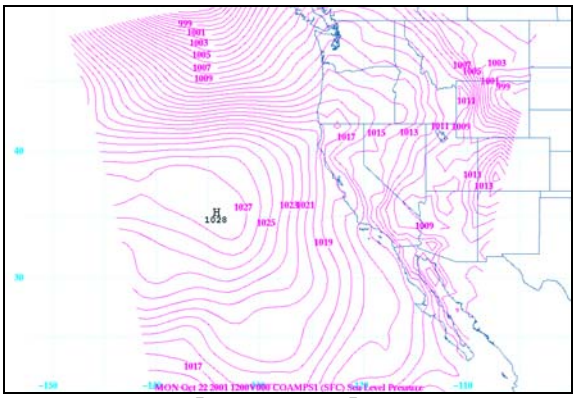

Figure 95. COAMPS analysis valid for 12Z, 22OCT01.

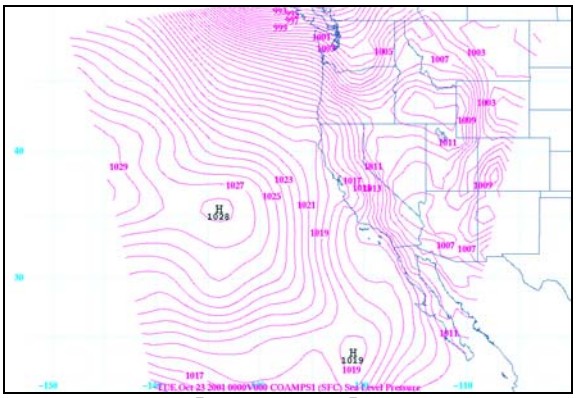

Figure 96. COAMPS analysis valid for 00Z, 23OCT01.

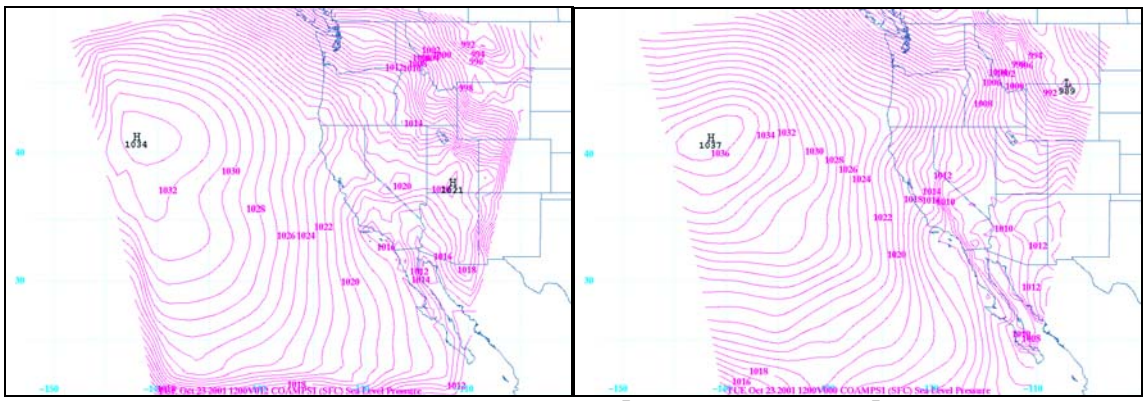

Figure 97. COAMPS forecast (left) and analysis (right) valid for 12Z, 23OCT01.

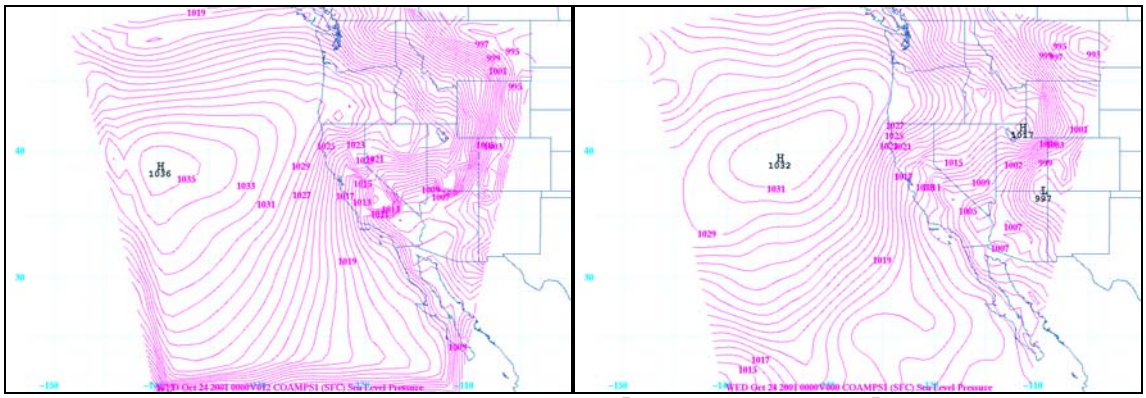

Figure 98. COAMPS forecast (left) and analysis (right) valid for 00Z, 24OCT01.

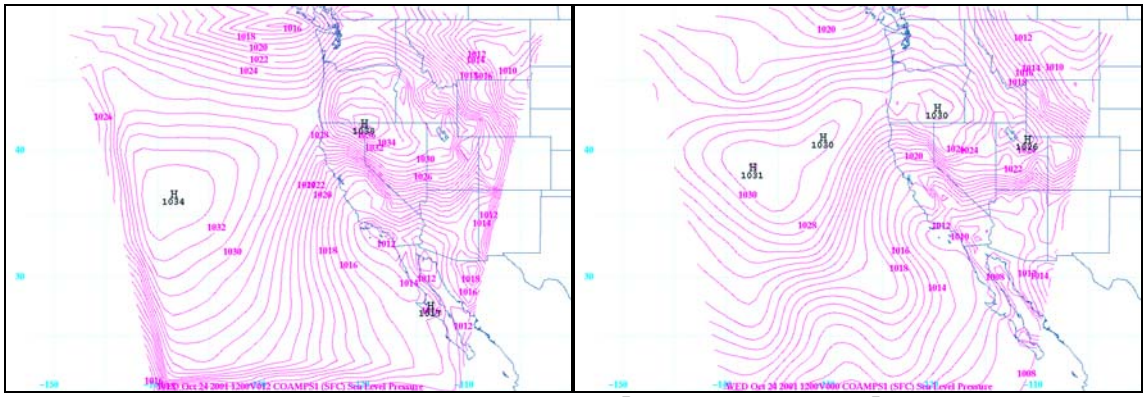

Figure 99. COAMPS forecast (left) and analysis (right) valid for 12Z, 24OCT01.

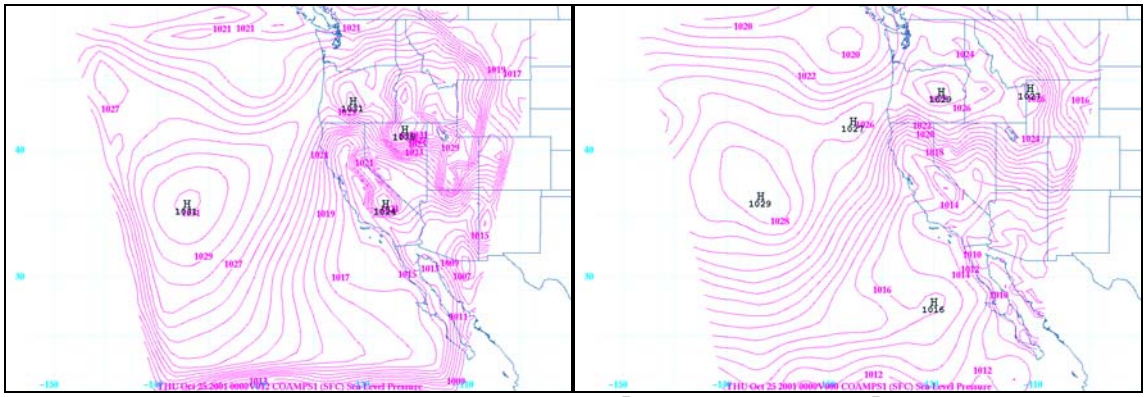

Figure 100. COAMPS forecast (left) and analysis (right) valid for 00Z, 25OCT01.

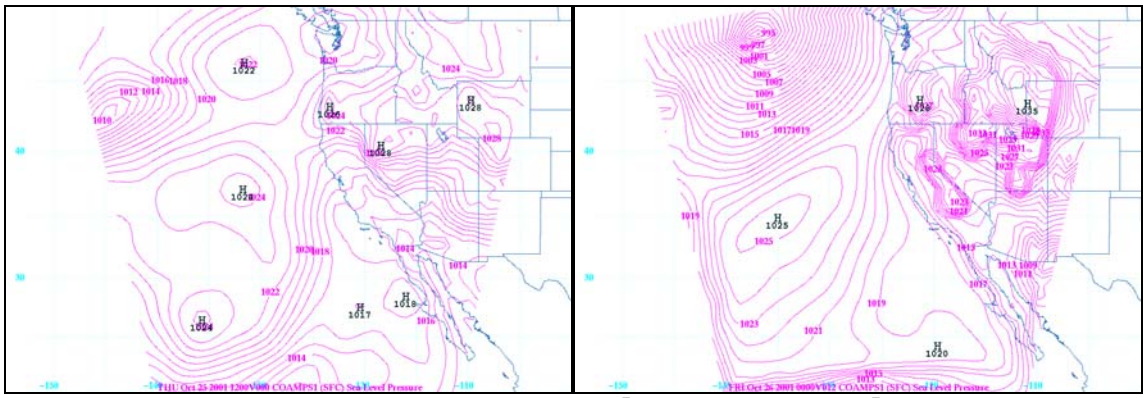

Figure 101. COAMPS forecast (left) and analysis (right) valid for 12Z, 25OCT01.

THIS PAGE INTENTIONALLY LEFT BLANK

APPENDIX D. AVN JET LEVEL ANALYSIS

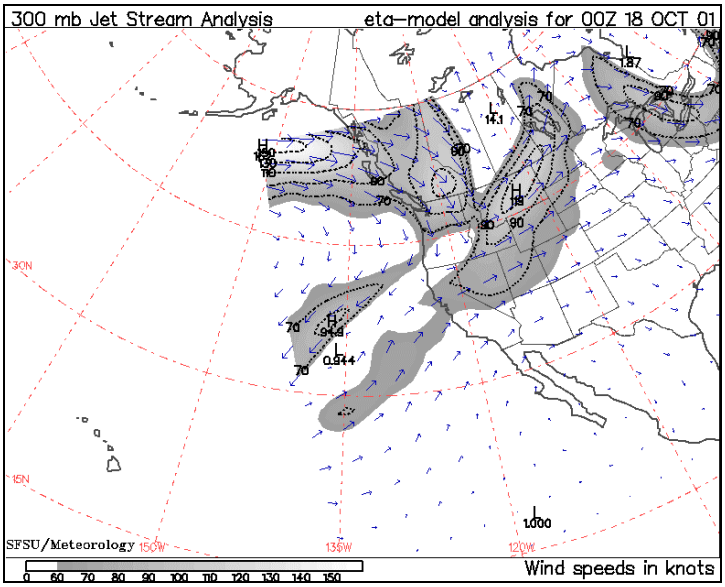

Figure 102. AVN Jet Stream Analysis 00Z, 18OCT01.

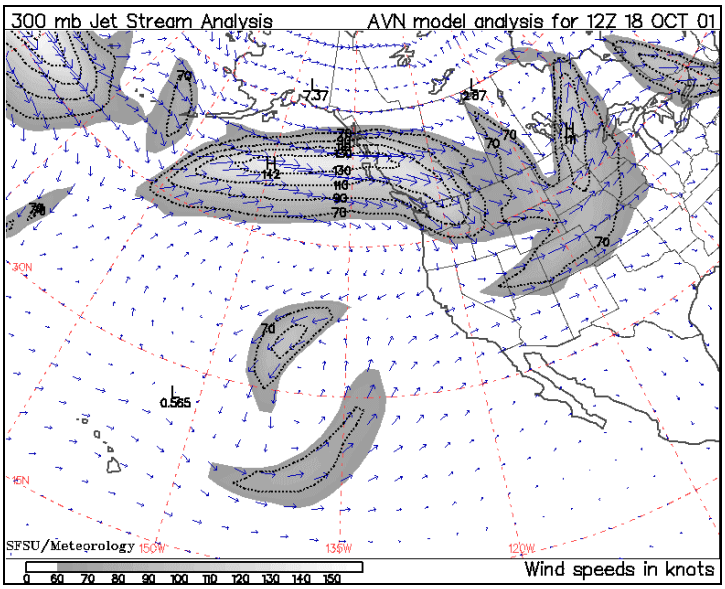

Figure 103. AVN Jet Stream Analysis 12Z, 18OCT01.

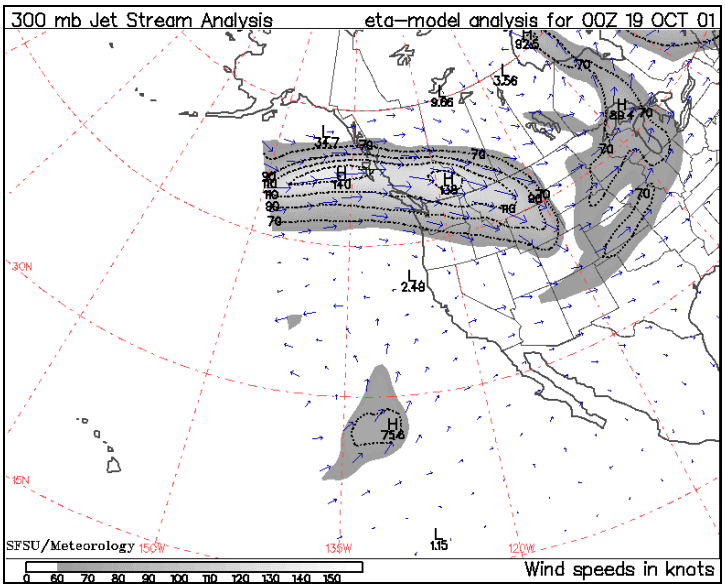

Figure 104. AVN Jet Stream Analysis 00Z, 19OCT01.

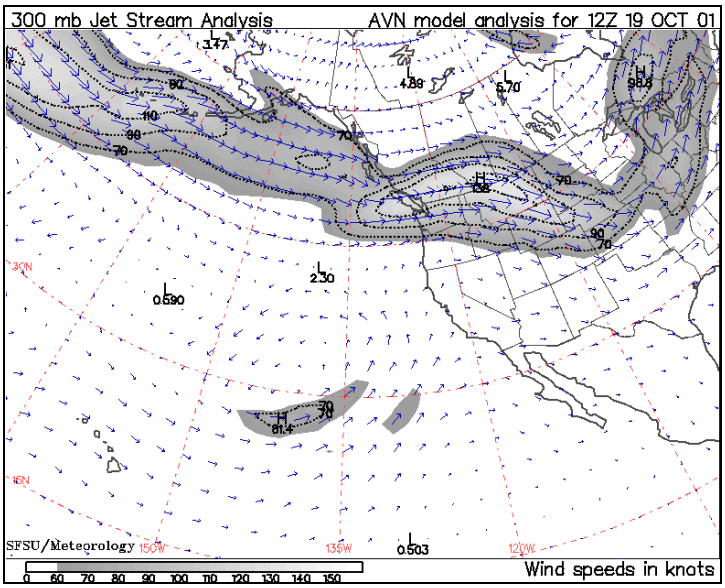

Figure 105. AVN Jet Stream Analysis 12Z, 19OCT01.

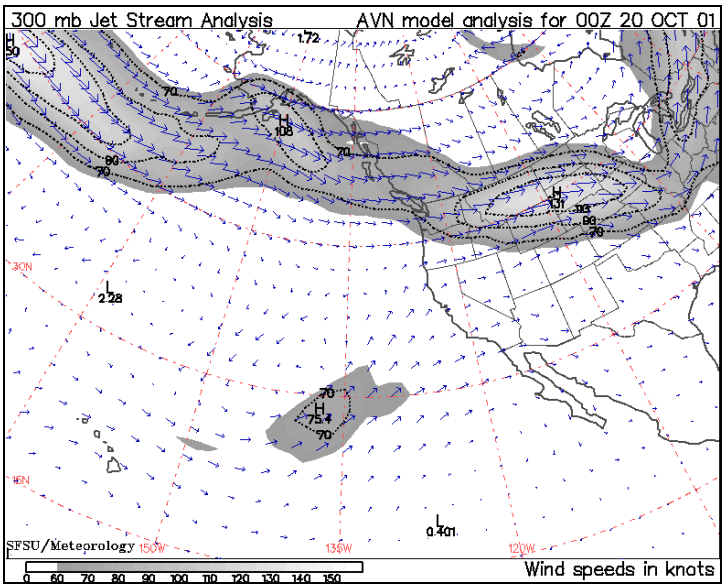

Figure 106. AVN Jet Stream Analysis 00Z, 20OCT01.

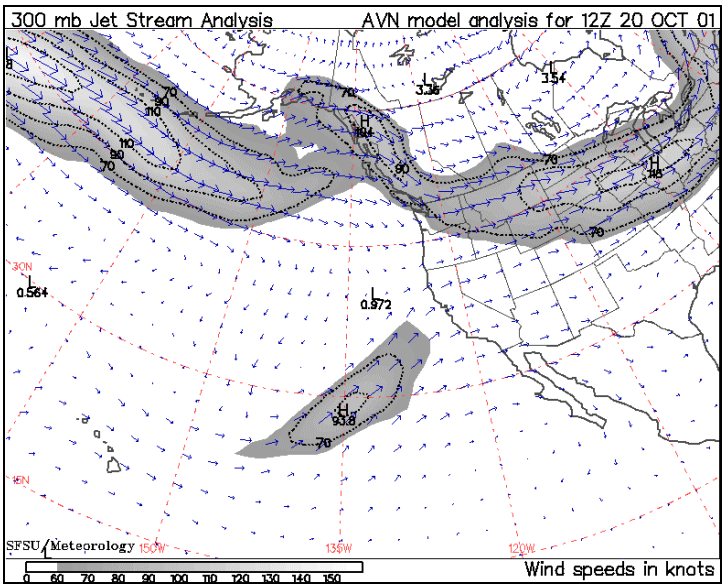

Figure 107. AVN Jet Stream Analysis 12Z, 20OCT01.

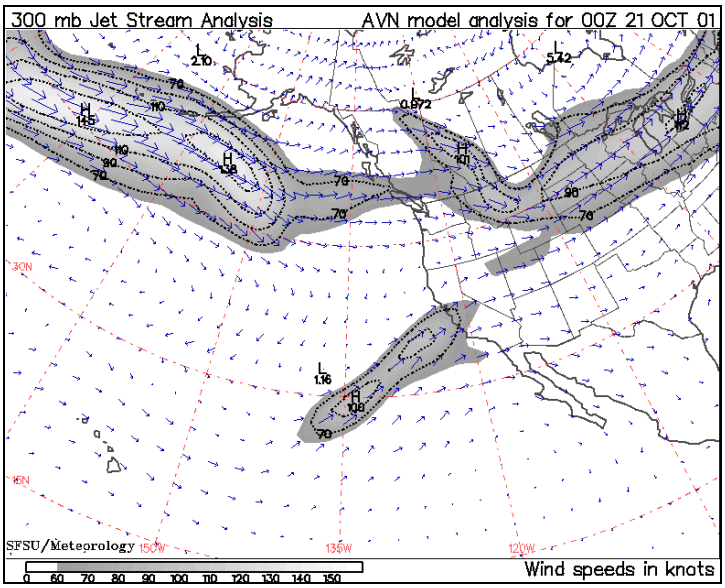

Figure 108. AVN Jet Stream Analysis 00Z, 21OCT01.

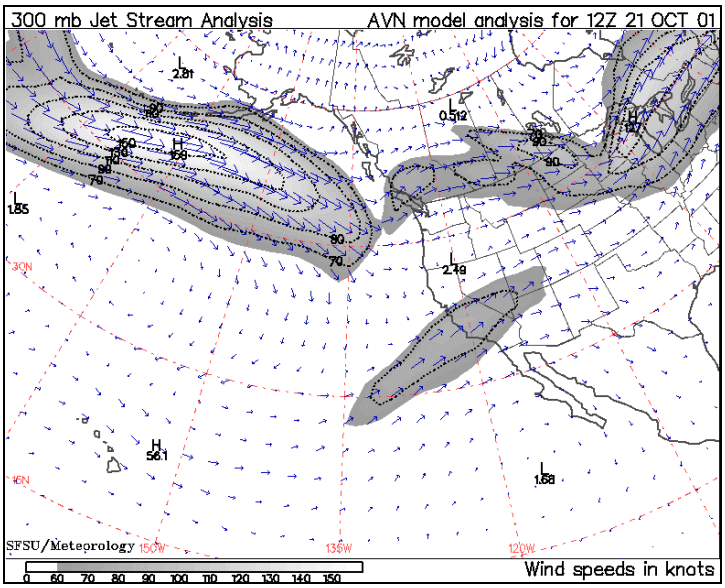

Figure 109. AVN Jet Stream Analysis 12Z, 21OCT01.

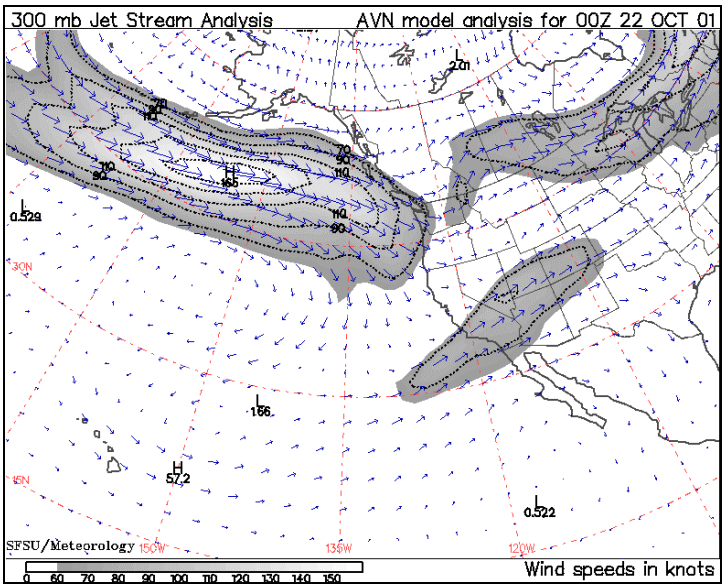

Figure 110. AVN Jet Stream Analysis 00Z, 22OCT01.

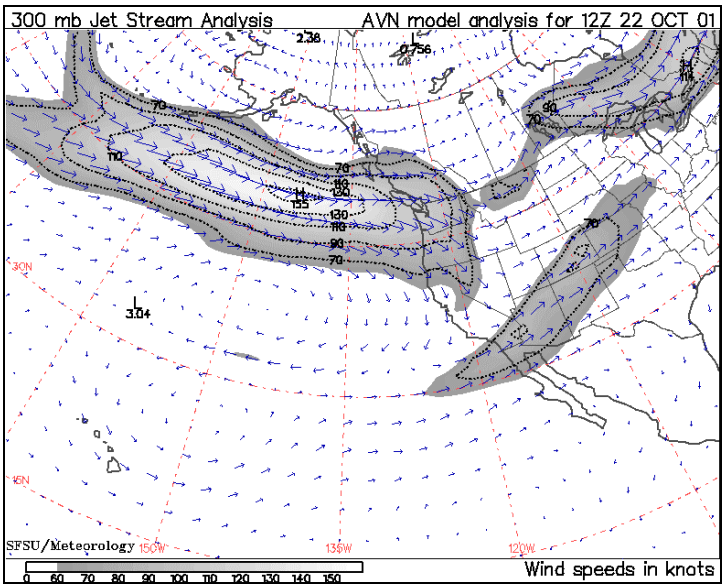

Figure 111. AVN Jet Stream Analysis 12Z, 22OCT01.

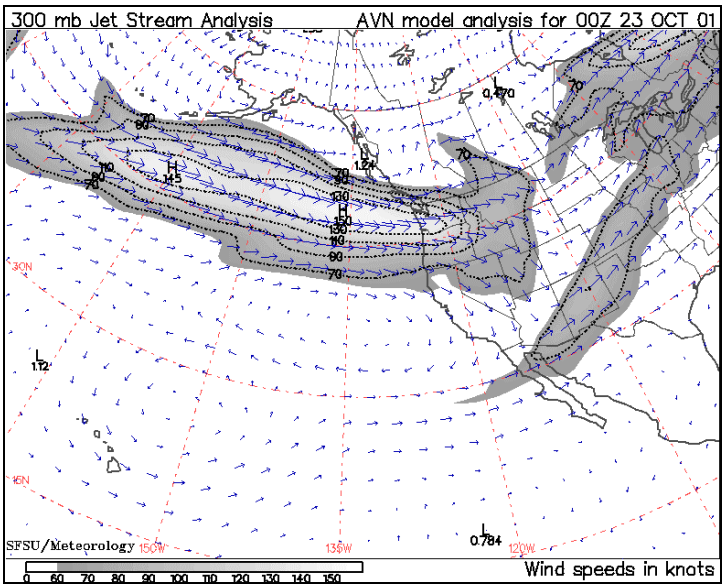

Figure 112. AVN Jet Stream Analysis 00Z, 23OCT01.

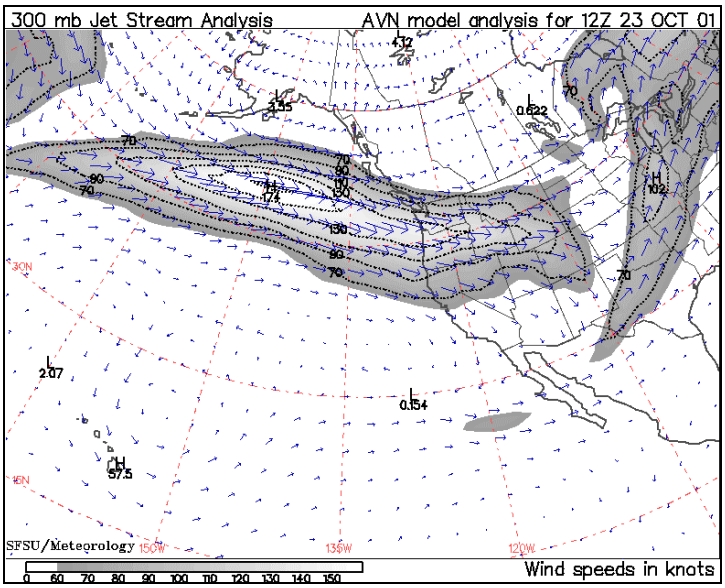

Figure 113. AVN Jet Stream Analysis 12Z, 23OCT01.

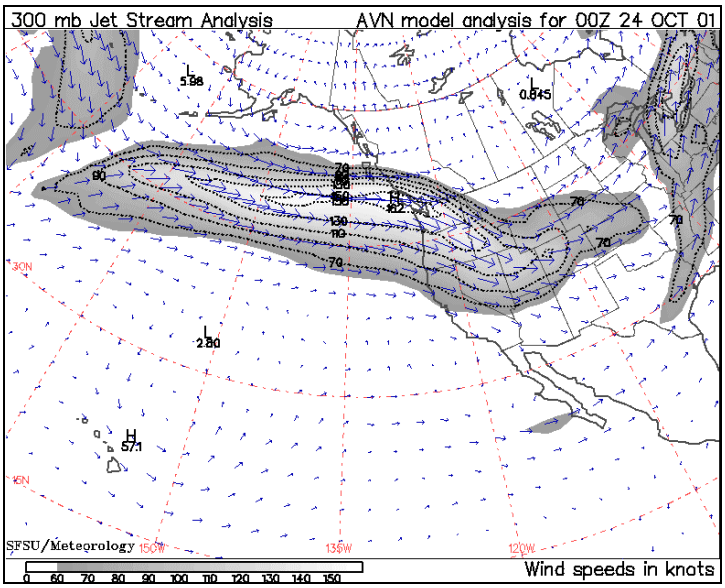

Figure 114. AVN Jet Stream Analysis 00Z, 24OCT01.

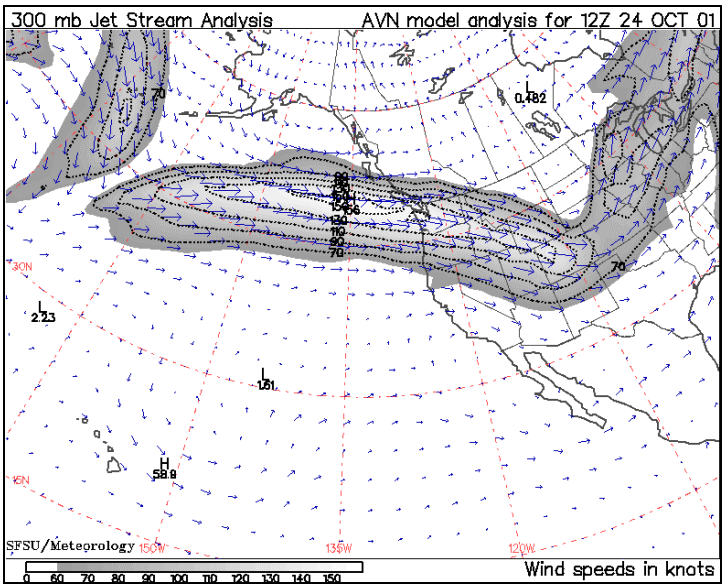

Figure 115. AVN Jet Stream Analysis 12Z, 24OCT01.

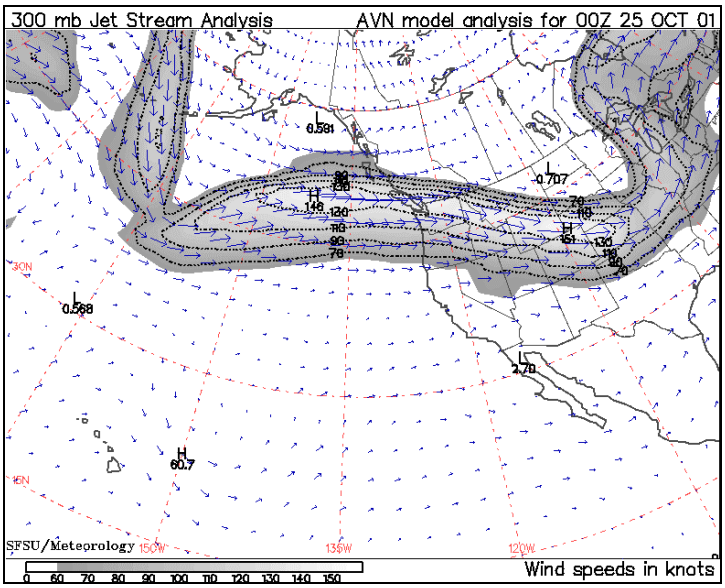

Figure 116. AVN Jet Stream Analysis 00Z, 25OCT01.

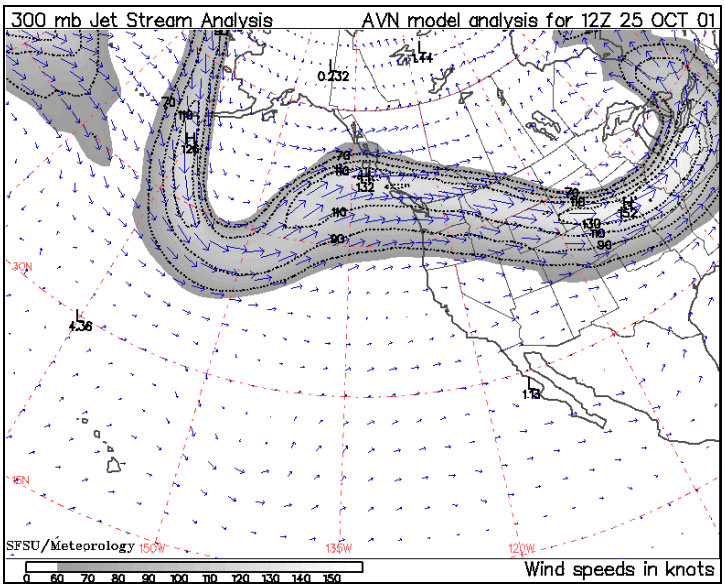

Figure 117. AVN Jet Stream Analysis 12Z, 25OCT01.

APPENDIX E. COAMPS JET LEVEL MODEL

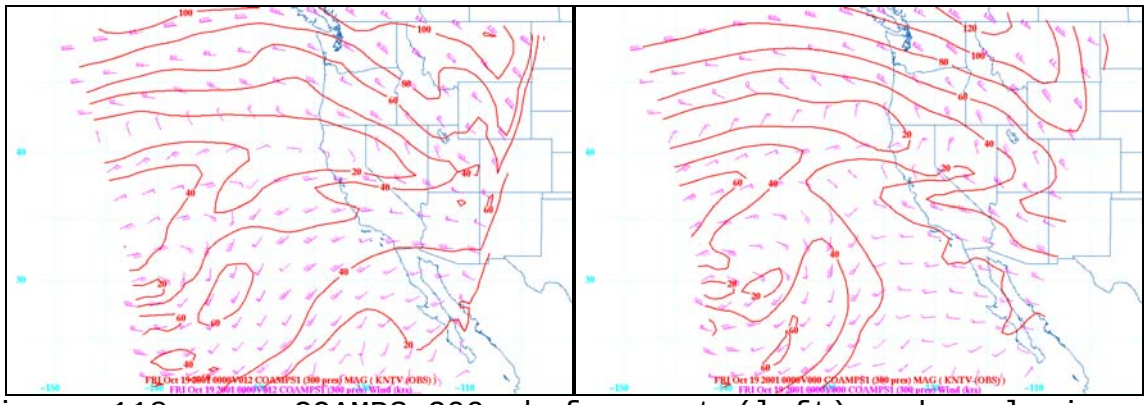

Figure 118. COAMPS 300 mb forecast (left) and analysis (right) valid for 00Z, 19OCT01.

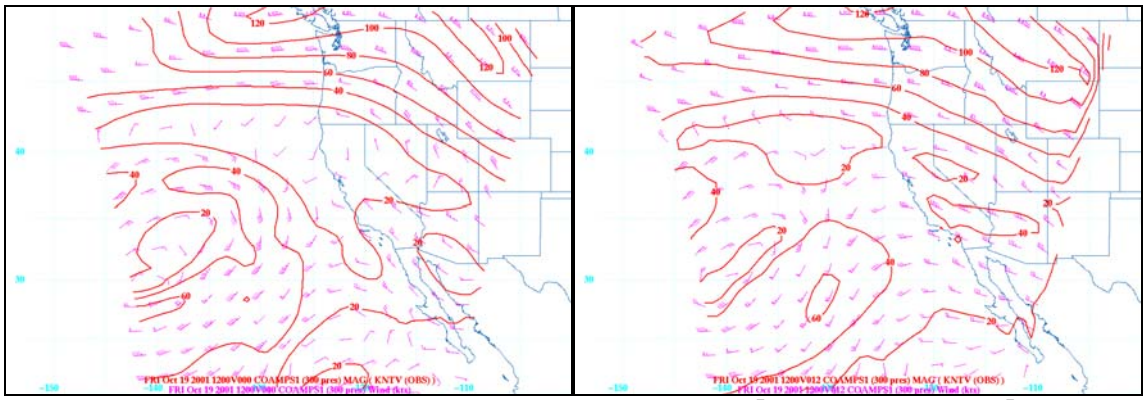

Figure 119. COAMPS 300 mb forecast (left) and analysis (right) valid for 12Z, 19OCT01.

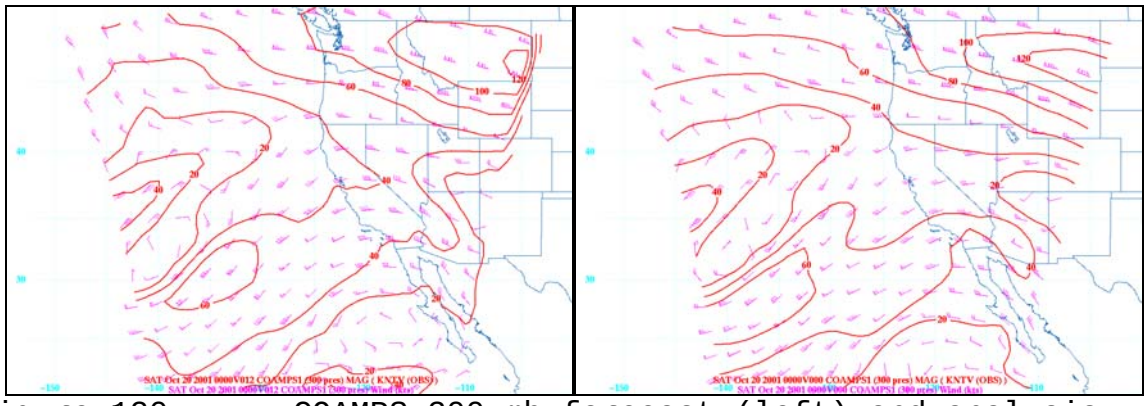

Figure 120. COAMPS 300 mb forecast (left) and analysis (right) valid for 00Z, 20OCT01.

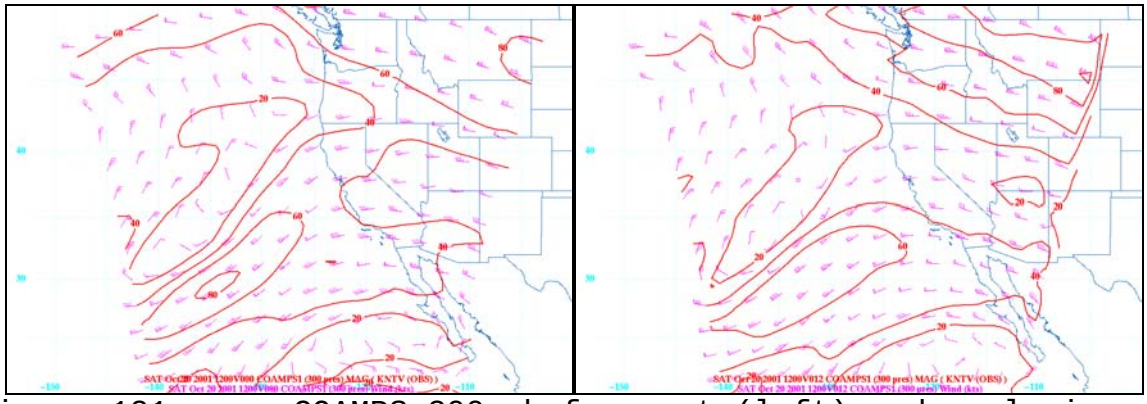

Figure 121. COAMPS 300 mb forecast (left) and analysis (right) valid for 12Z, 20OCT01.

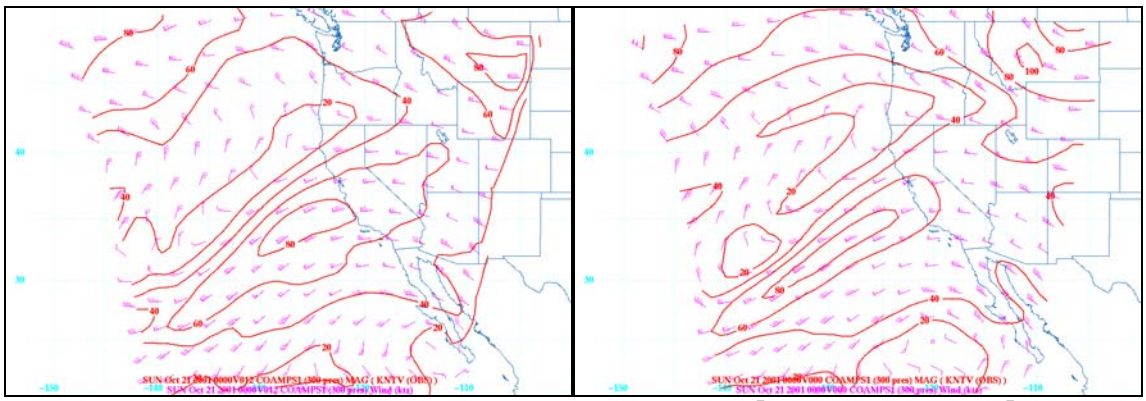

Figure 122. COAMPS 300 mb forecast (left) and analysis (right) valid for 00Z, 21OCT01.

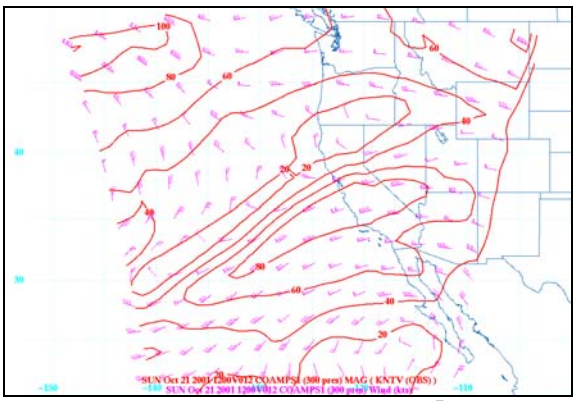

Figure 123. COAMPS 300 mb forecast valid 12Z 21OCT01.

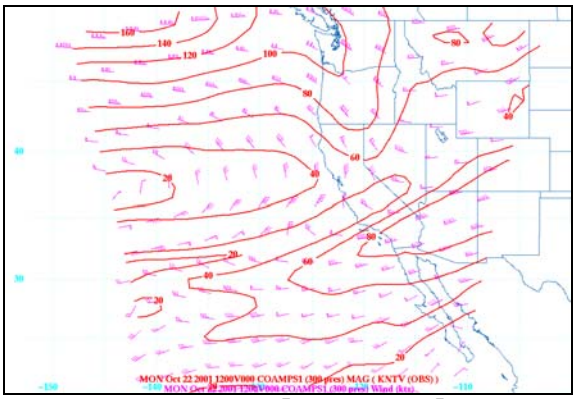

Figure 124. COAMPS 300 mb analysis valid 12Z 22OCT01.

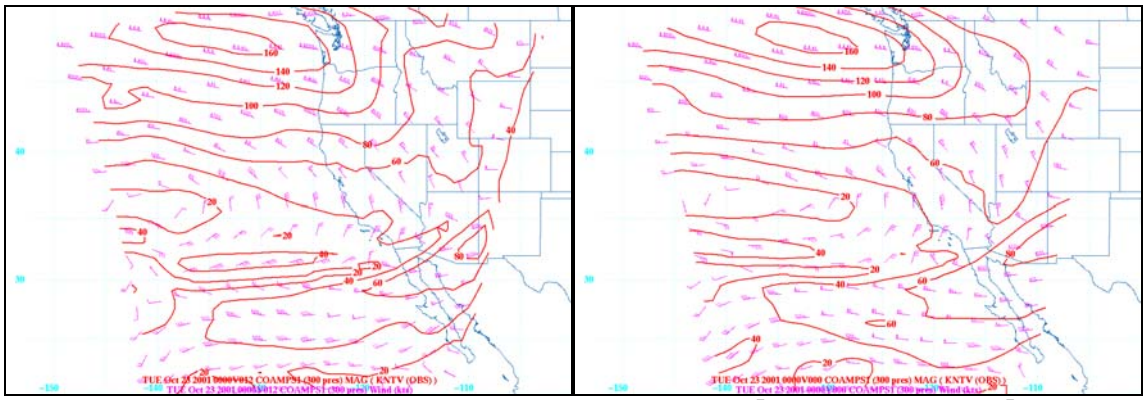

Figure 125. COAMPS 300 mb forecast (left) and analysis (right) valid for 00Z, 23OCT01.

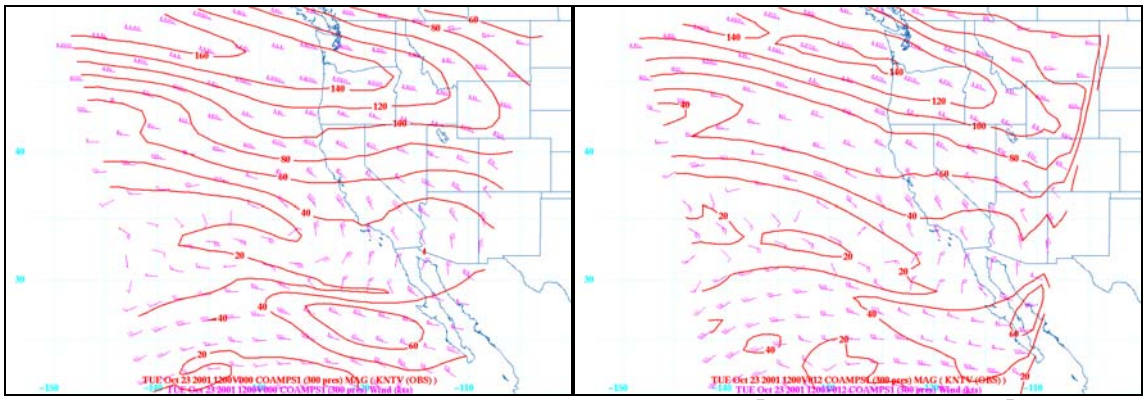

Figure 126. COAMPS 300 mb forecast (left) and analysis (right) valid for 12Z, 23OCT01.

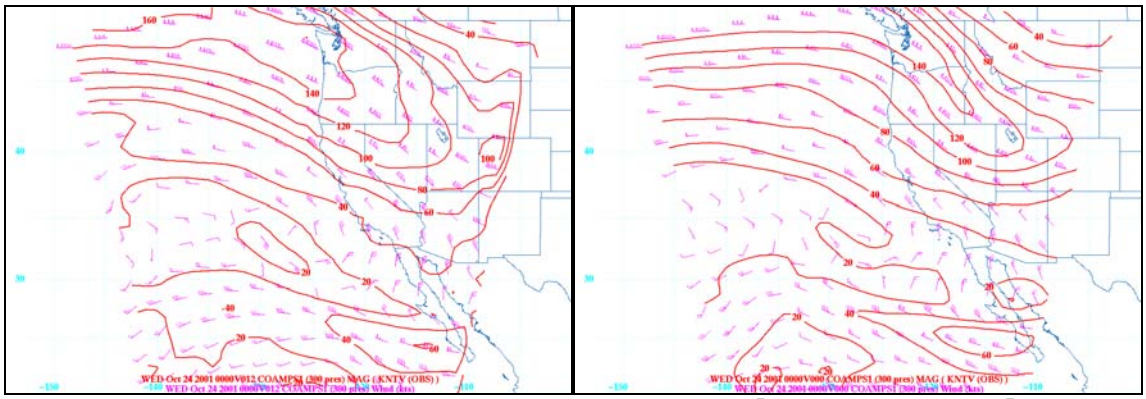

Figure 127. COAMPS 300 mb forecast (left) and analysis (right) valid for 00Z, 24OCT01.

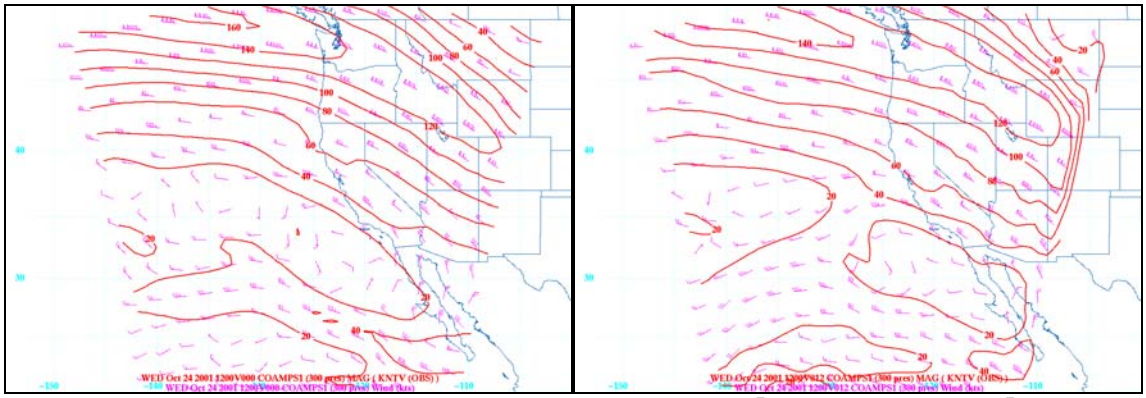

Figure 128. COAMPS 300 mb forecast (left) and analysis (right) valid for 12Z, 24OCT01.

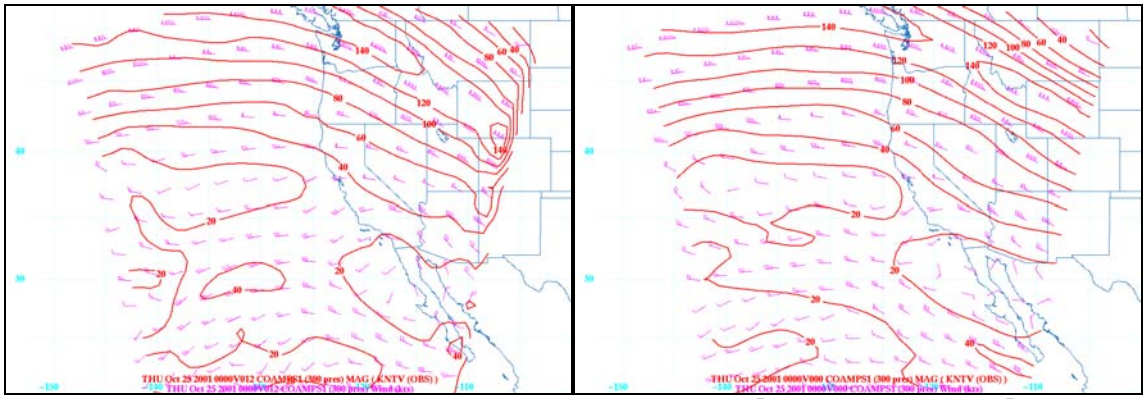

Figure 129. COAMPS 300 mb forecast (left) and analysis (right) valid for 00Z, 25OCT01.

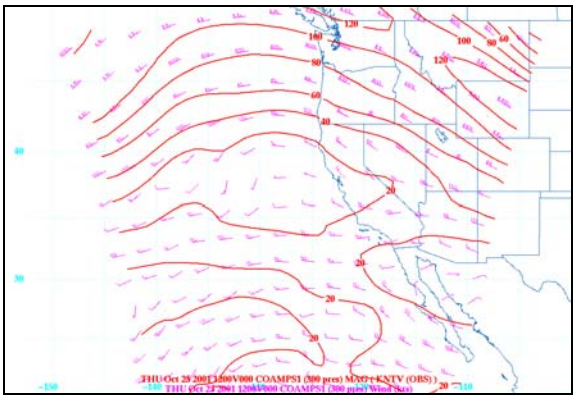

Figure 130. COAMPS 300 mb analysis valid 12Z 25OCT01.

THIS PAGE INTENTIONALLY LEFT BLANK

APPENDIX F. RAWINSONDE PROFILES

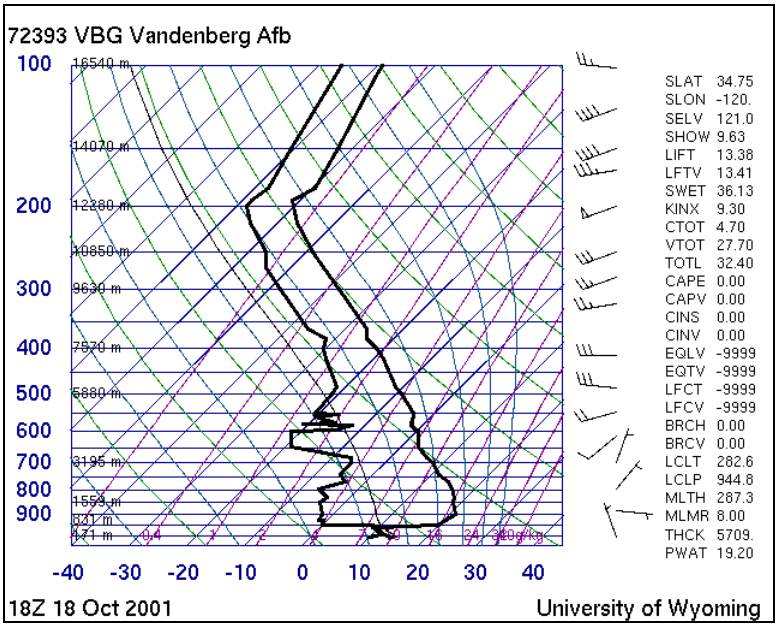

Figure 131. Vandenberg AFB, 18Z 18OCT01.

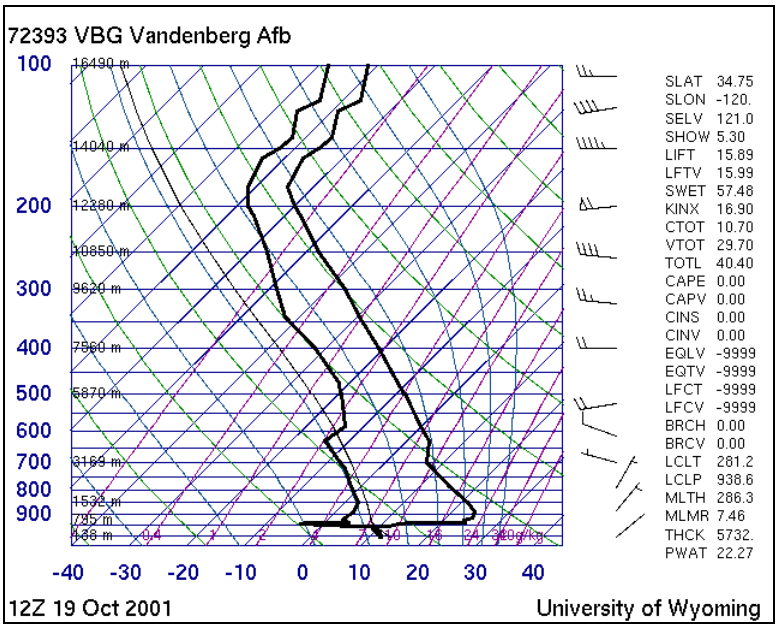

Figure 132. Vandenberg AFB, 12Z 19OCT01.

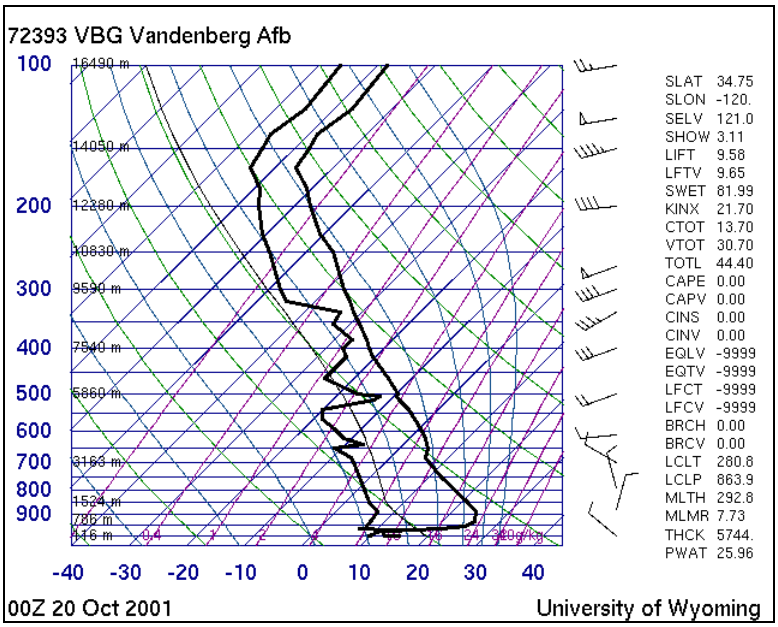

Figure 133. Vandenberg AFB, 00Z 20OCT01.

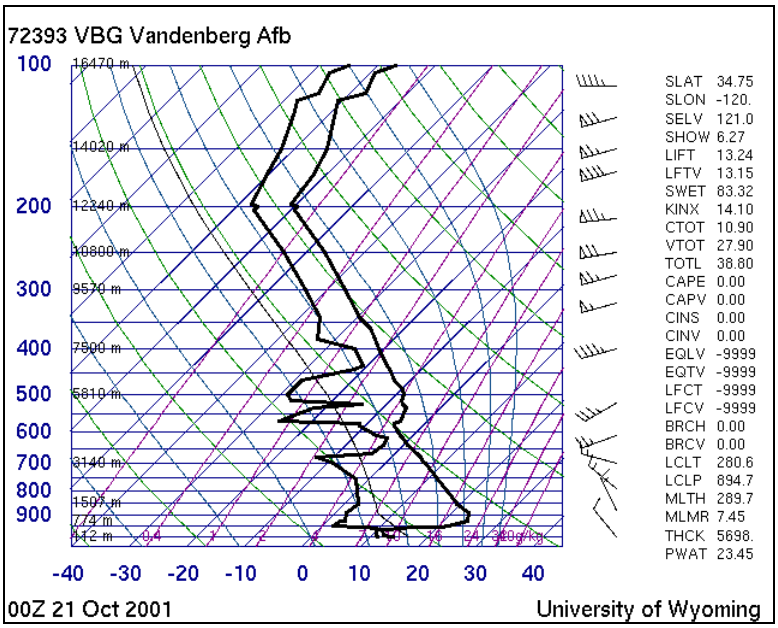

Figure 134. Vandenberg AFB, 00Z 21OCT01.

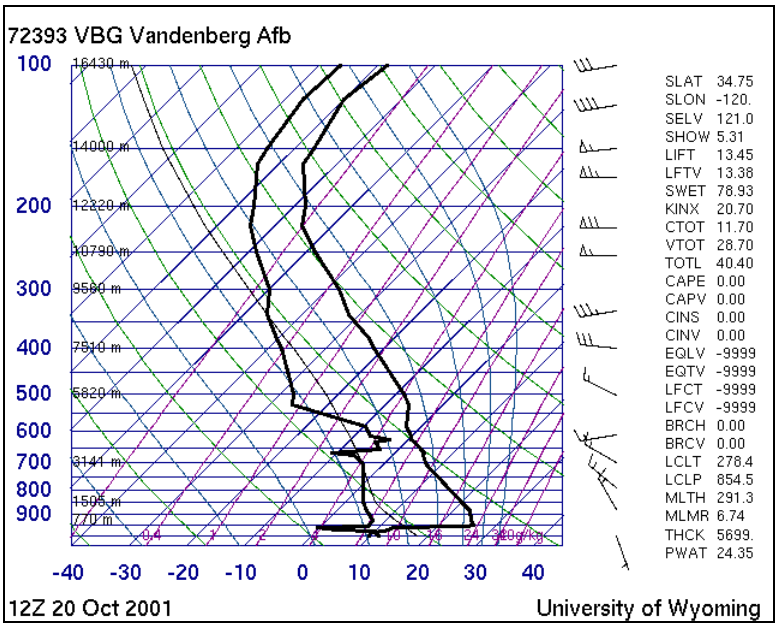

Figure 135. Vandenberg AFB, 12Z 20OCT01.

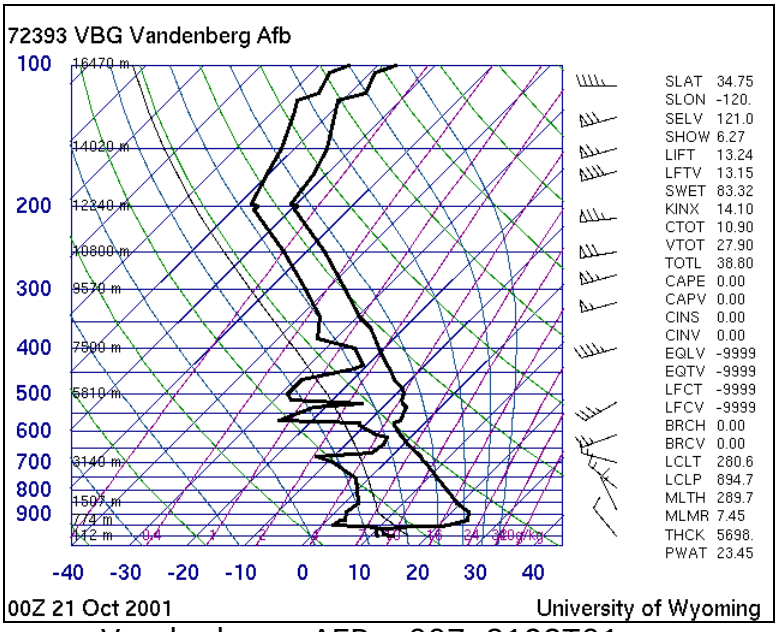

Figure 136. Vandenberg AFB, 00Z 21OCT01.

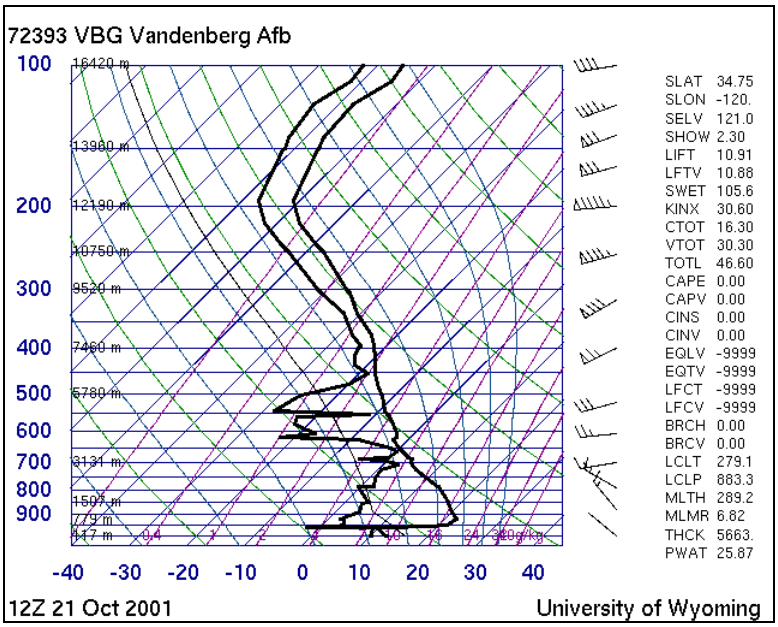

Figure 137. Vandenberg AFB, 12Z 21OCT01.

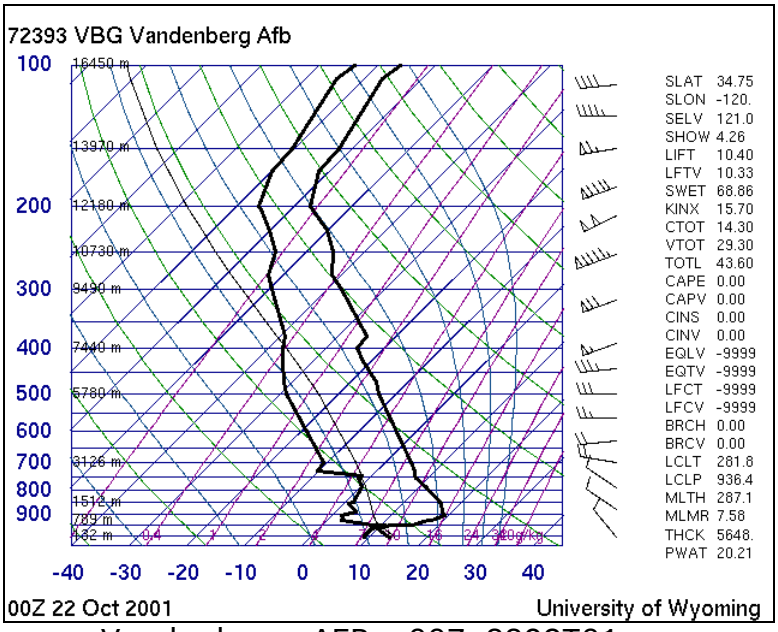

Figure 138. Vandenberg AFB, 00Z 22OCT01.

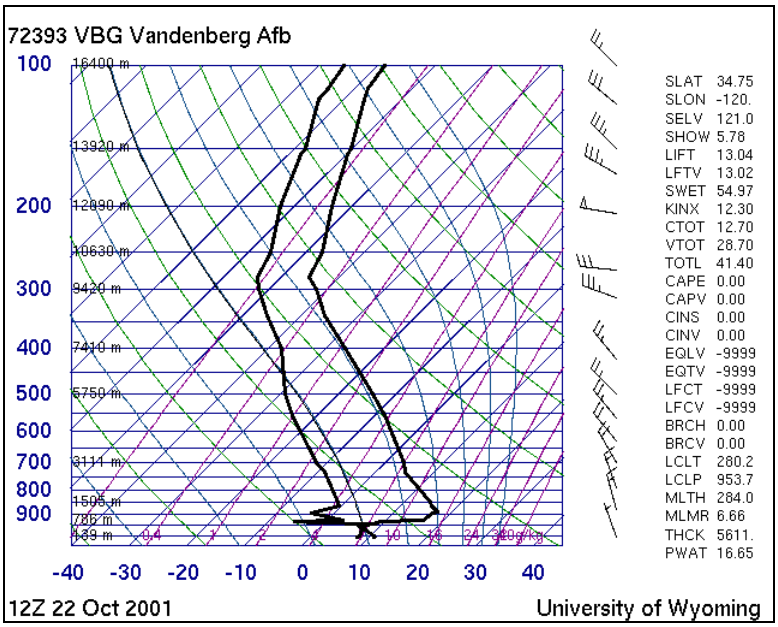

Figure 139. Vandenberg AFB, 12Z 22OCT01.

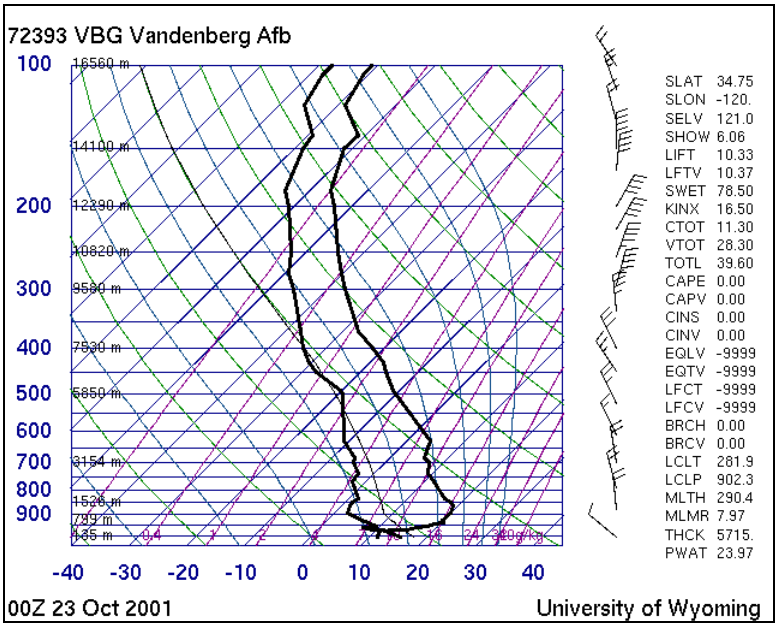

Figure 140. Vandenberg AFB, 00Z 23OCT01.

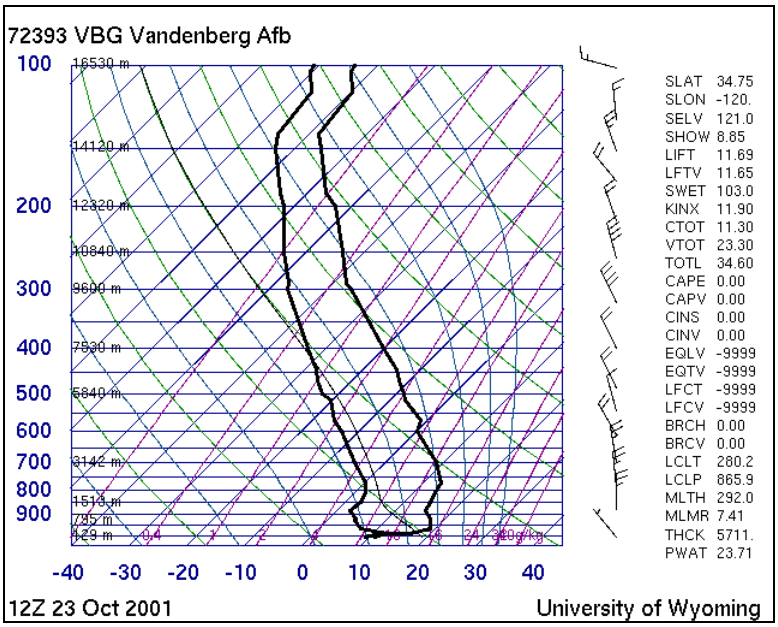

Figure 141. Vandenberg AFB, 12Z 23OCT01.

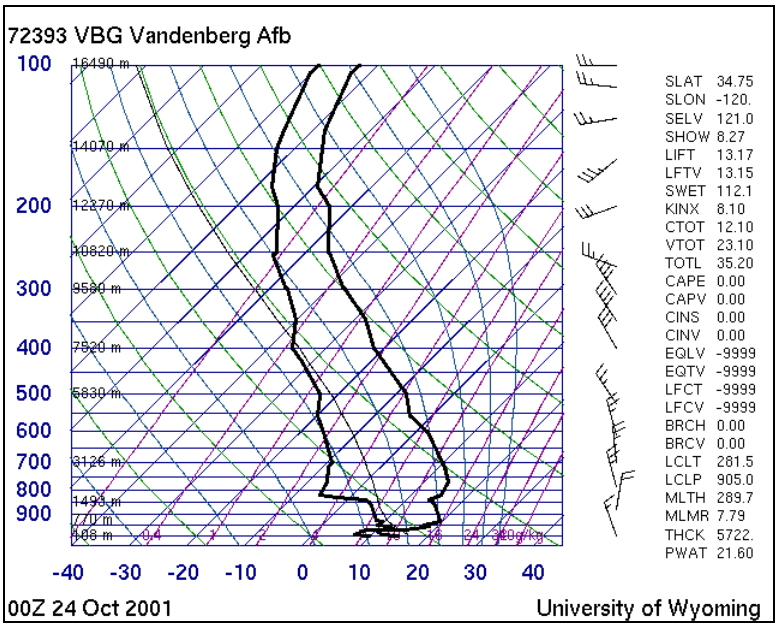

Figure 142. Vandenberg AFB, 00Z 24OCT01.

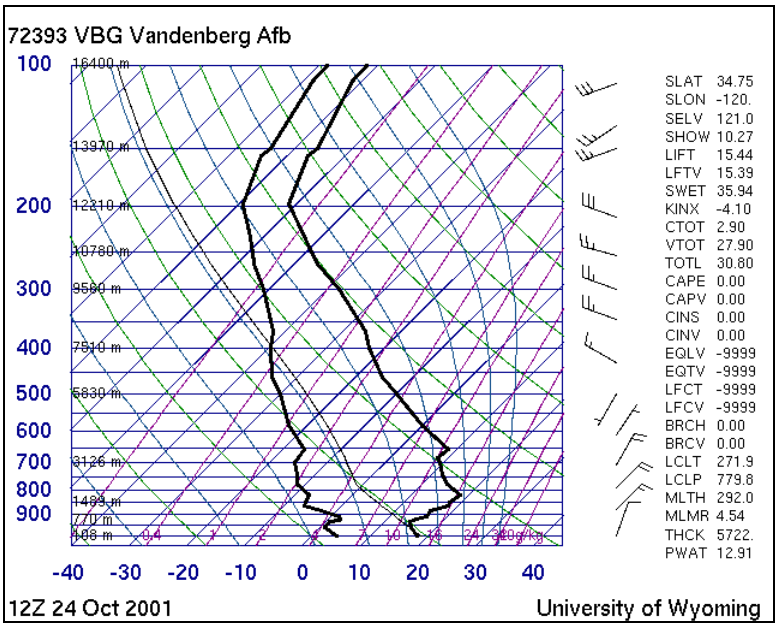

Figure 143. Vandenberg AFB, 12Z 24OCT01.

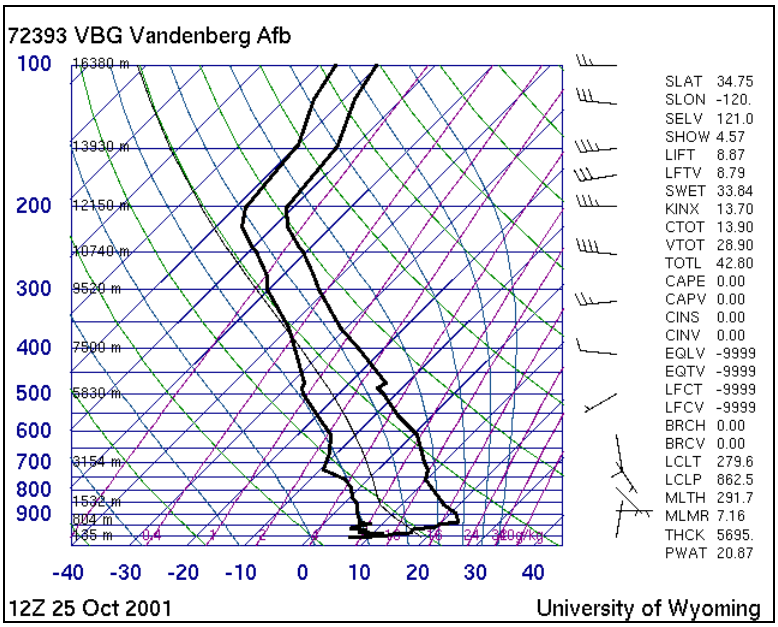

Figure 144. Vandenberg AFB, 12Z 25OCT01.

THIS PAGE INTENTIONALLY LEFT BLANK

APPENDIX G. COAMPS VERTICAL PROFILE FORECASTS

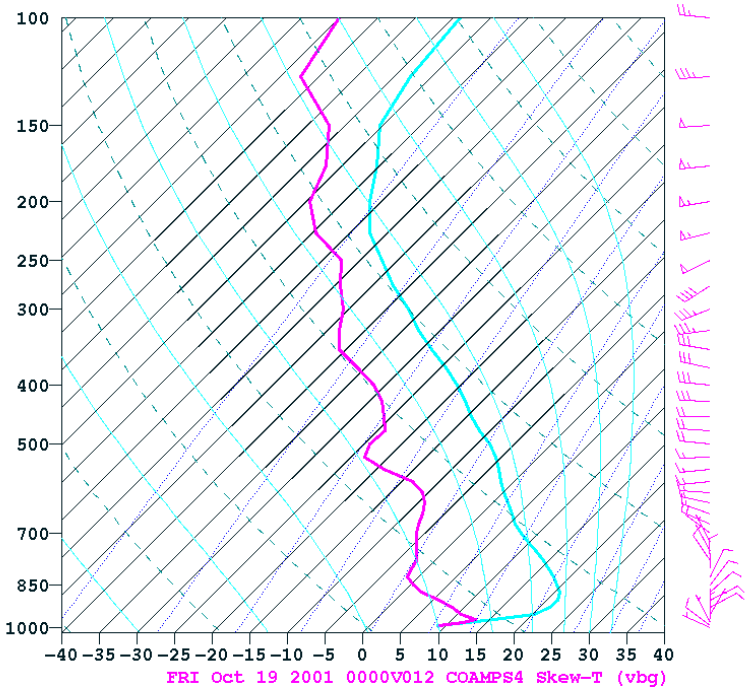

Figure 145. COAMPS forecast for 00Z, 19OCT01.

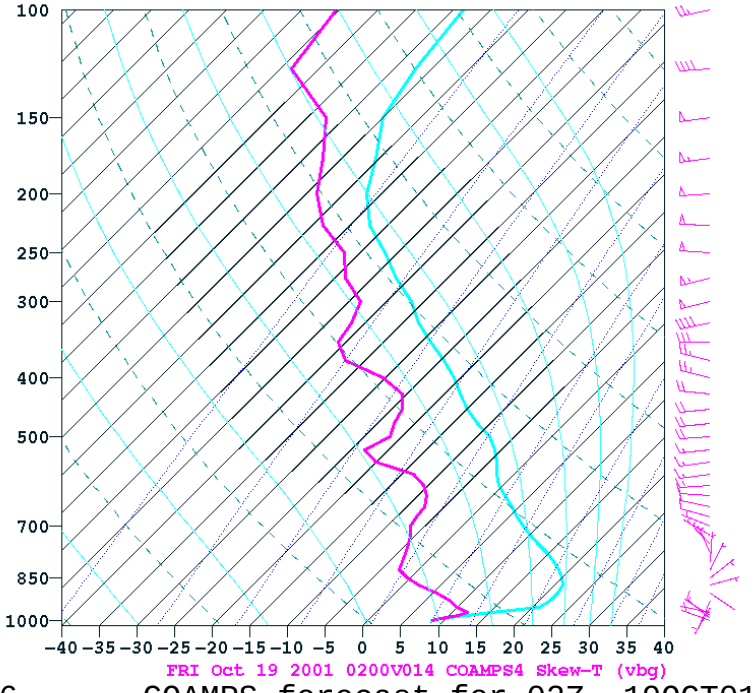

Figure 146. COAMPS forecast for 02Z, 19OCT01.

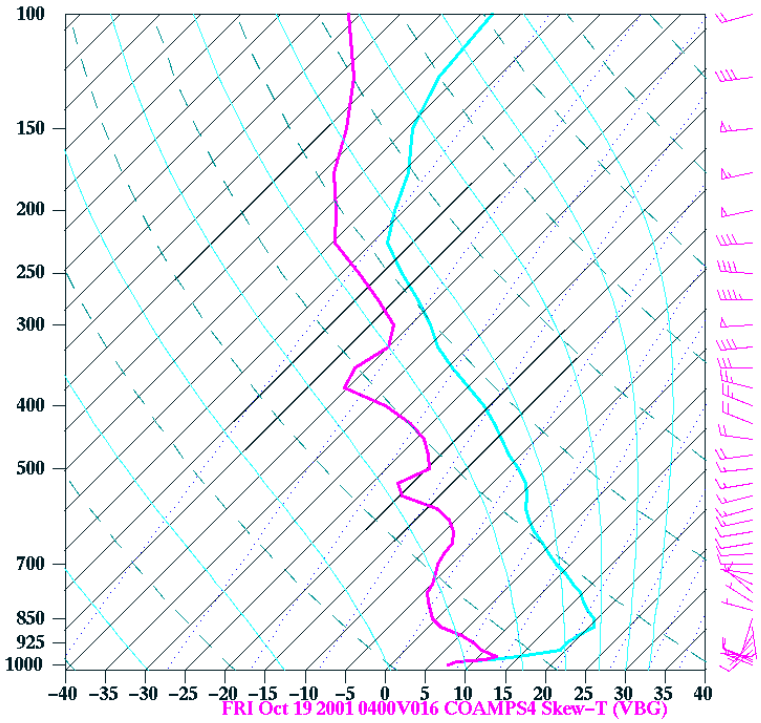

Figure 147. COAMPS forecast for 04Z, 19OCT01.

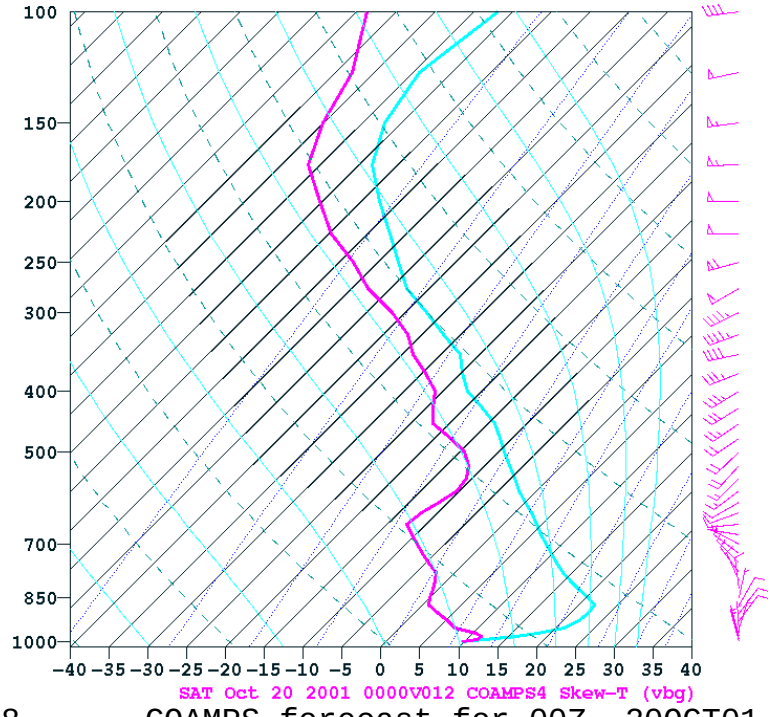

Figure 148. COAMPS forecast for 00Z, 20OCT01.

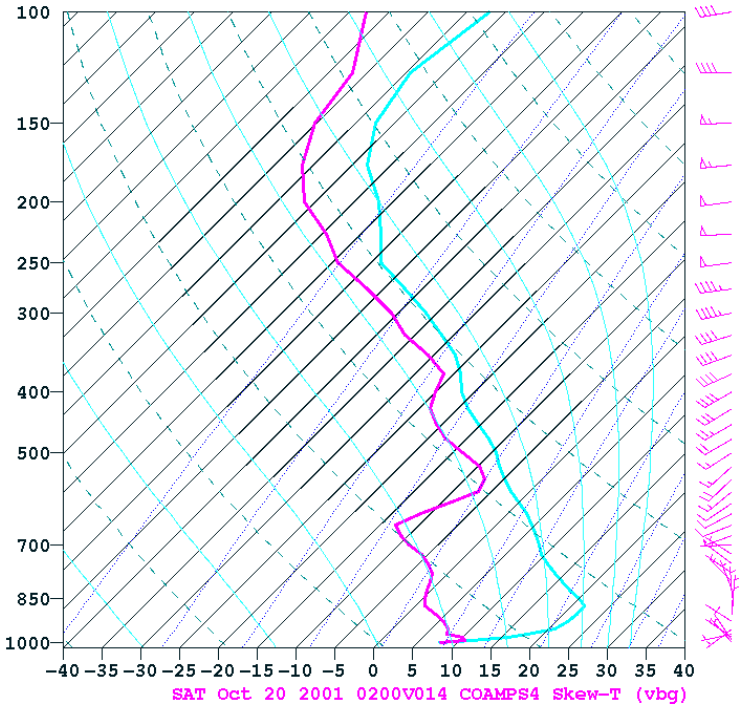

Figure 149. COAMPS forecast for 02Z, 20OCT01.

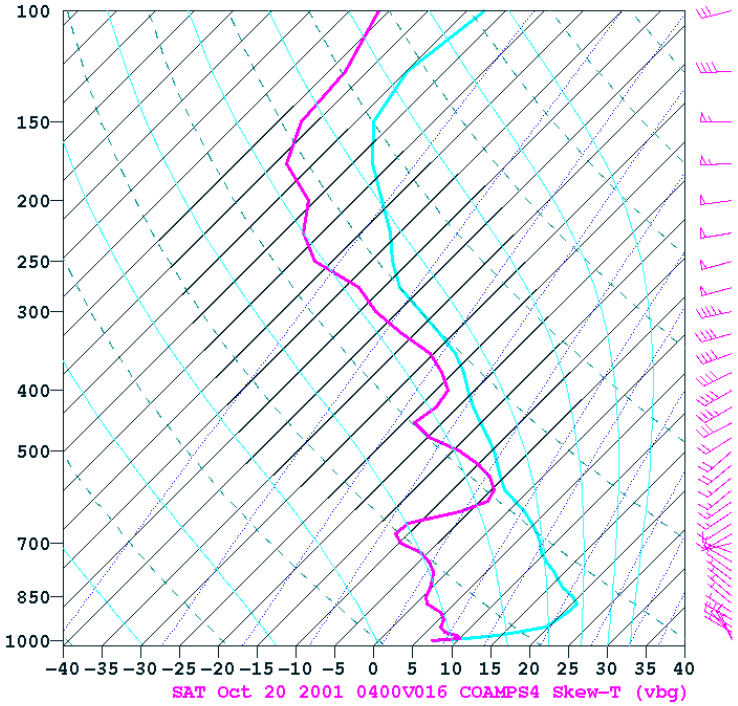

Figure 150. COAMPS forecast for 04Z, 20OCT01.

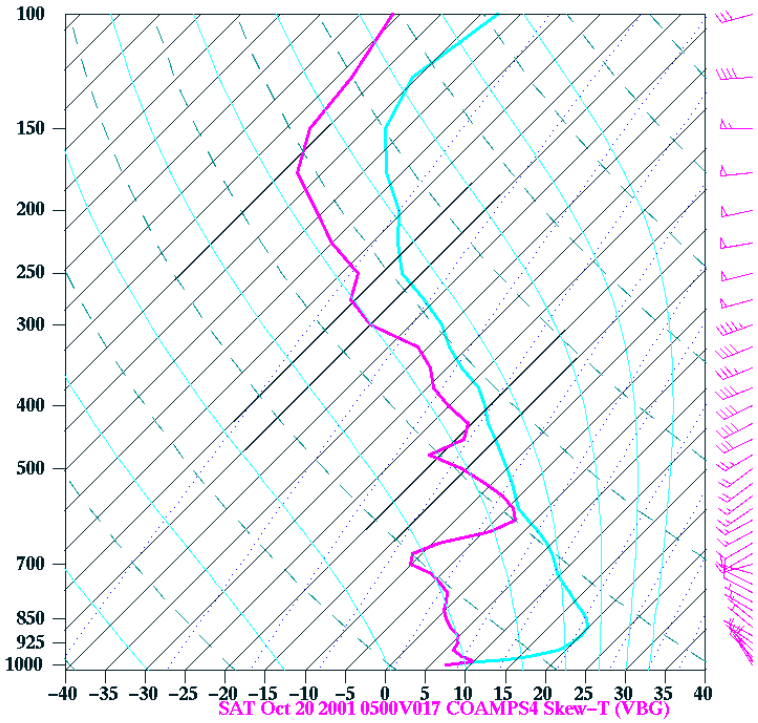

Figure 151. COAMPS forecast for 05Z, 20OCT01.

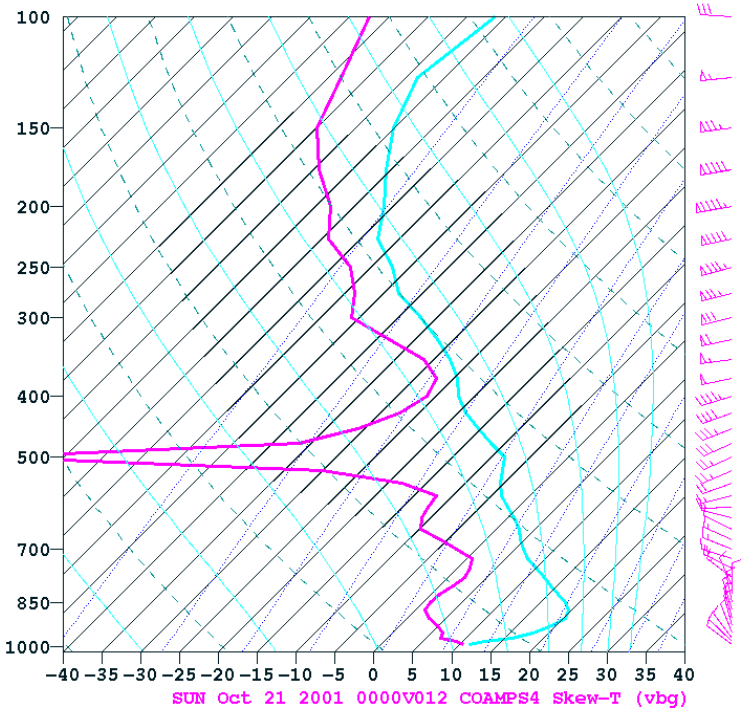

Figure 152. COAMPS forecast for 00Z, 21OCT01.

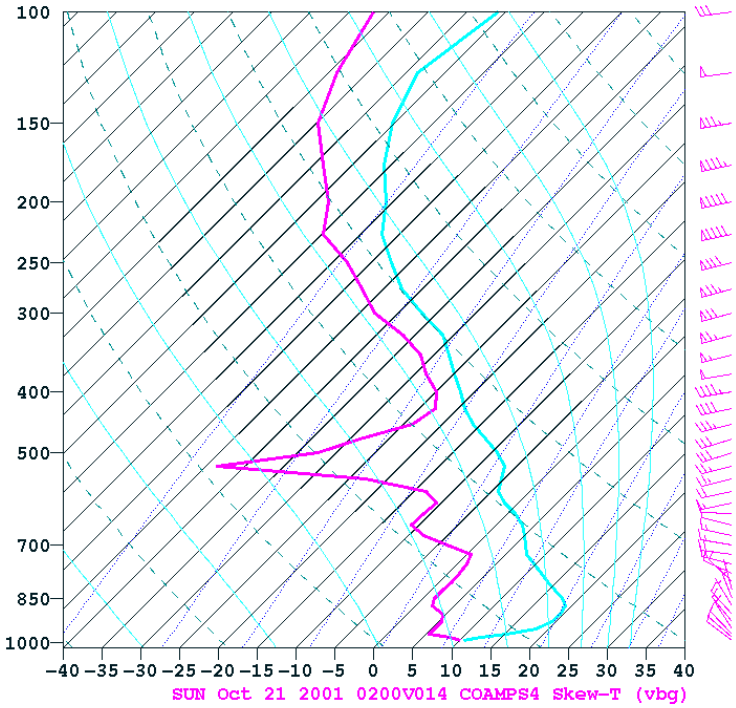

Figure 153. COAMPS forecast for 02Z, 21OCT01.

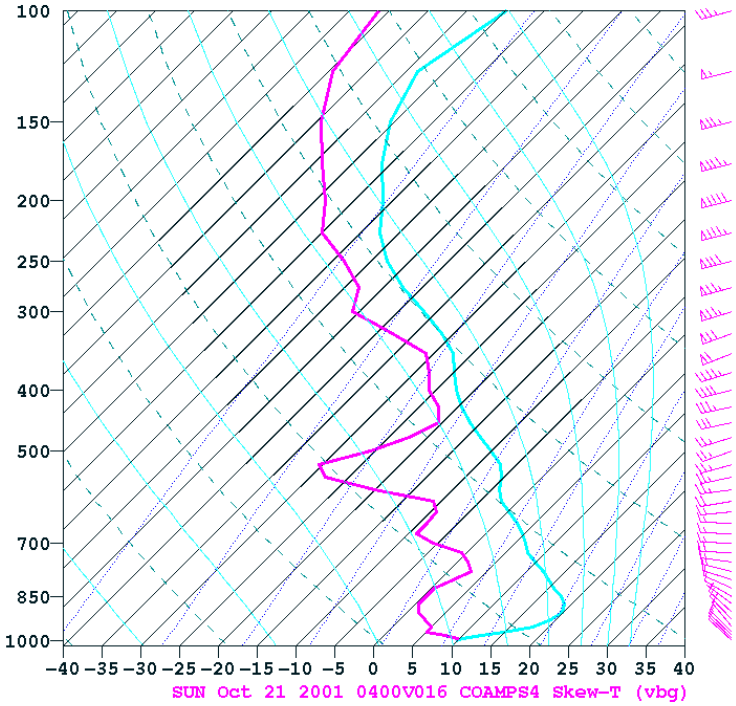

Figure 154. COAMPS forecast for 04Z, 21OCT01.

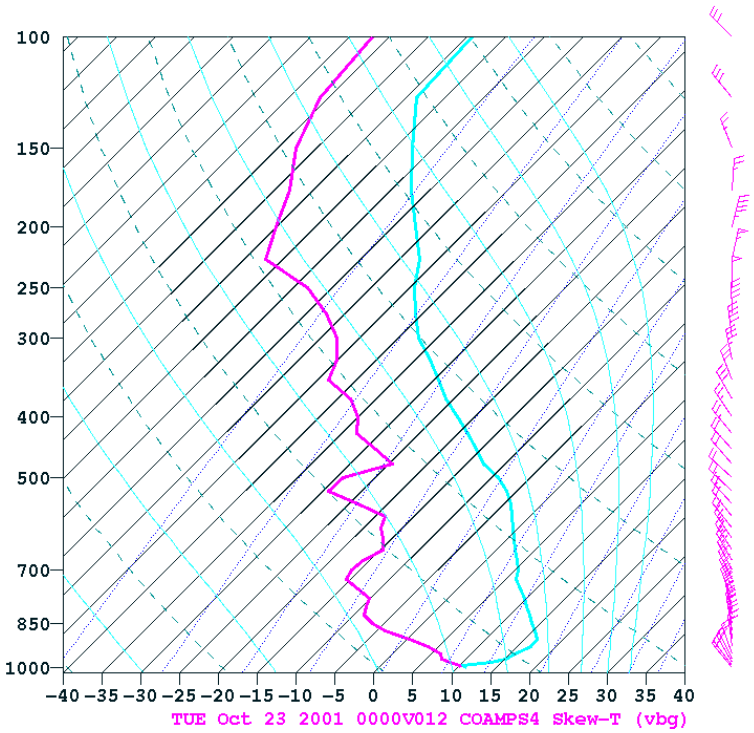

Figure 155. COAMPS forecast for 00Z, 23OCT01.

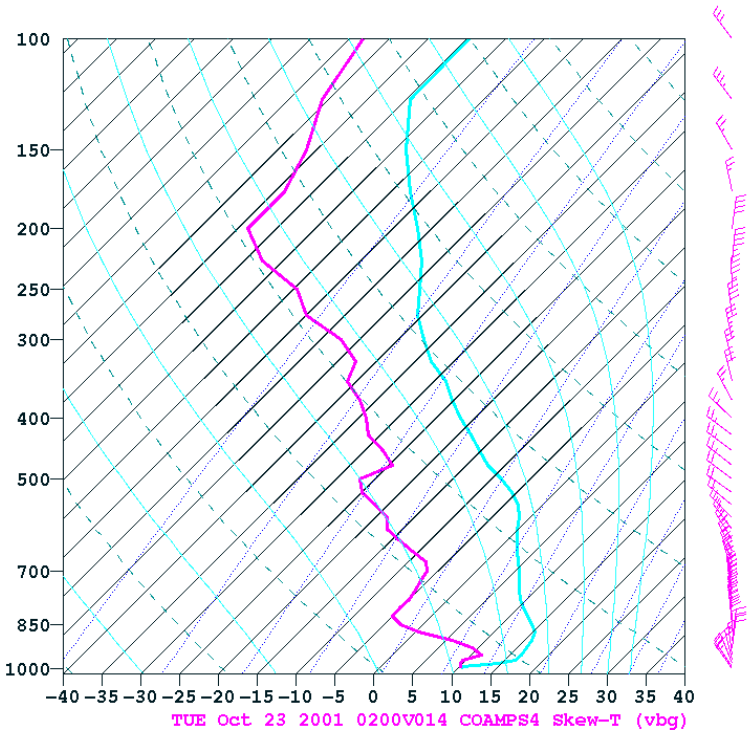

Figure 156. COAMPS forecast for 02Z, 23OCT01.

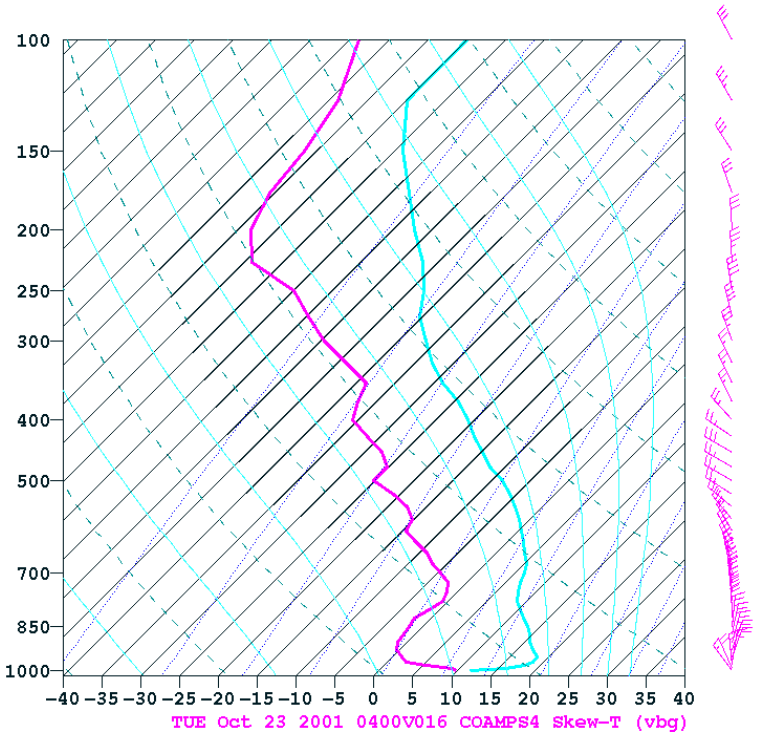

Figure 157. COAMPS forecast for 04Z, 23OCT01.

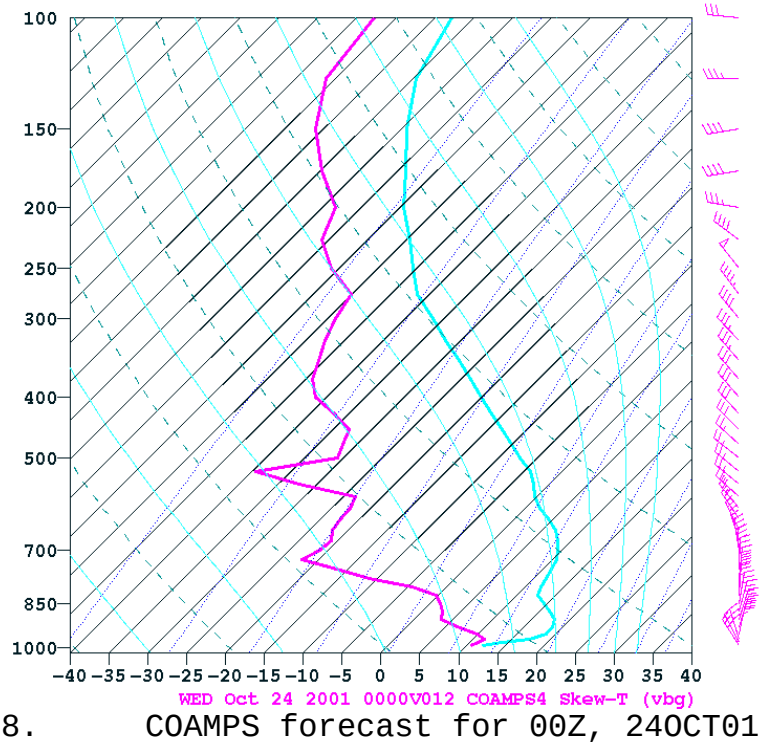

Figure 158. COAMPS forecast for 00Z, 24OCT01.

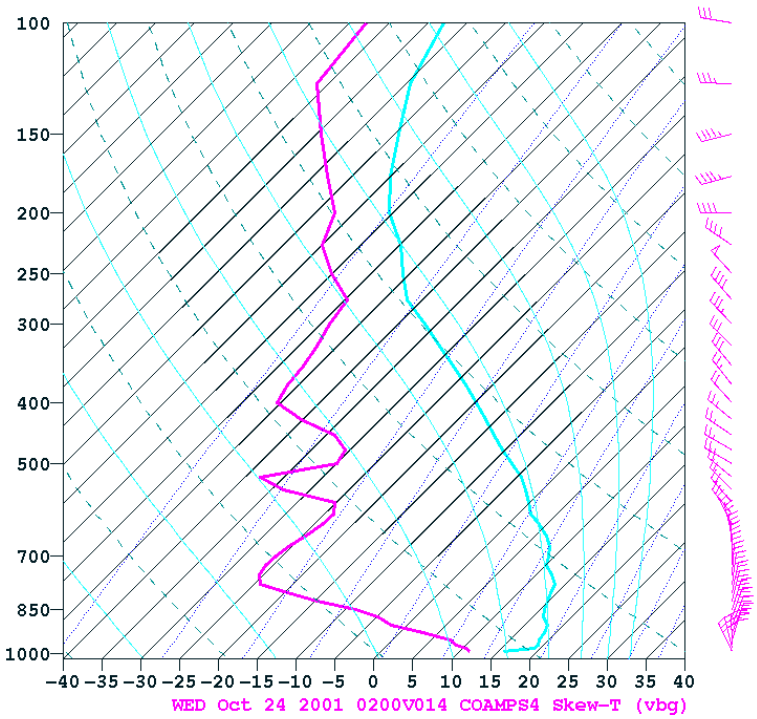

Figure 159. COAMPS forecast for 02Z, 24OCT01.

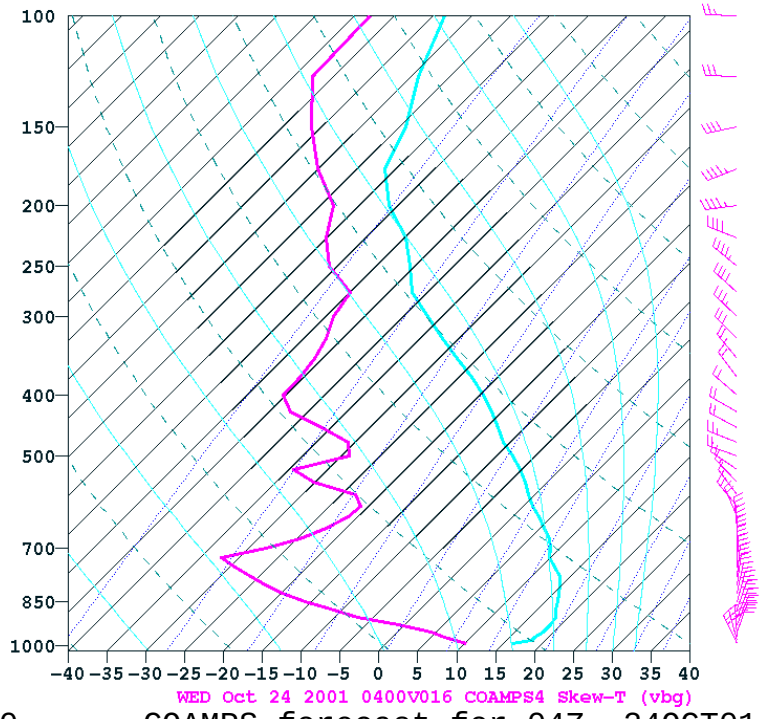

Figure 160. COAMPS forecast for 04Z, 24OCT01.

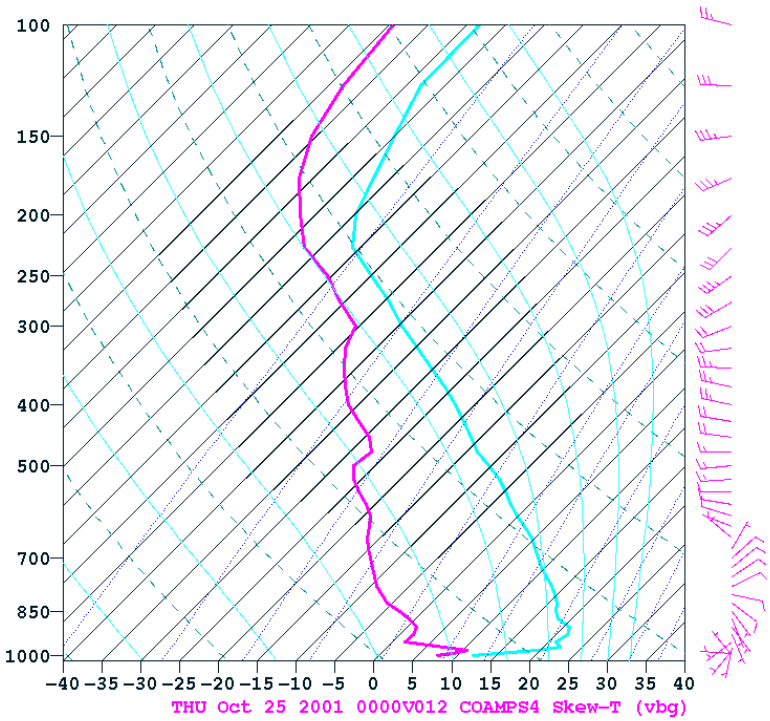

Figure 161. COAMPS forecast for 00Z, 25OCT01.

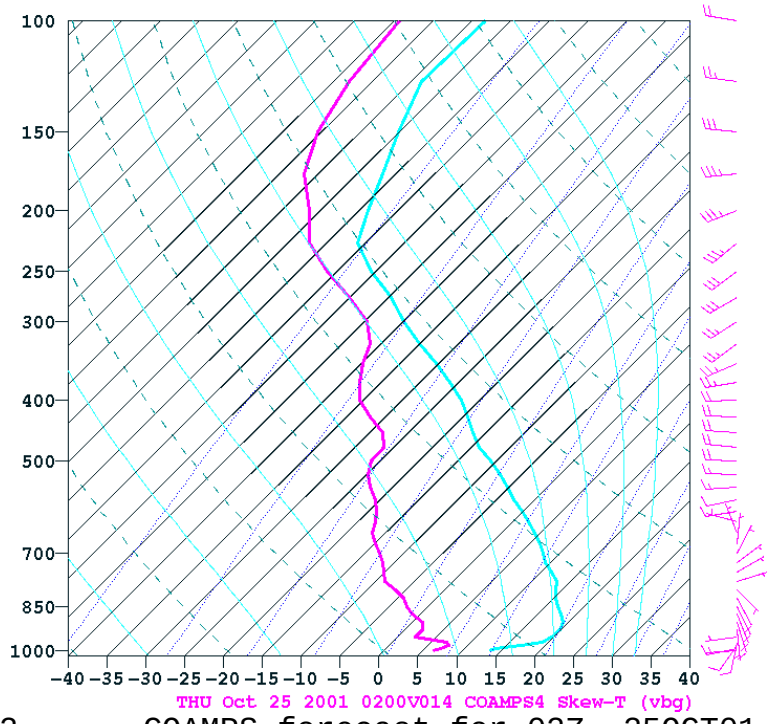

Figure 162. COAMPS forecast for 02Z, 25OCT01.

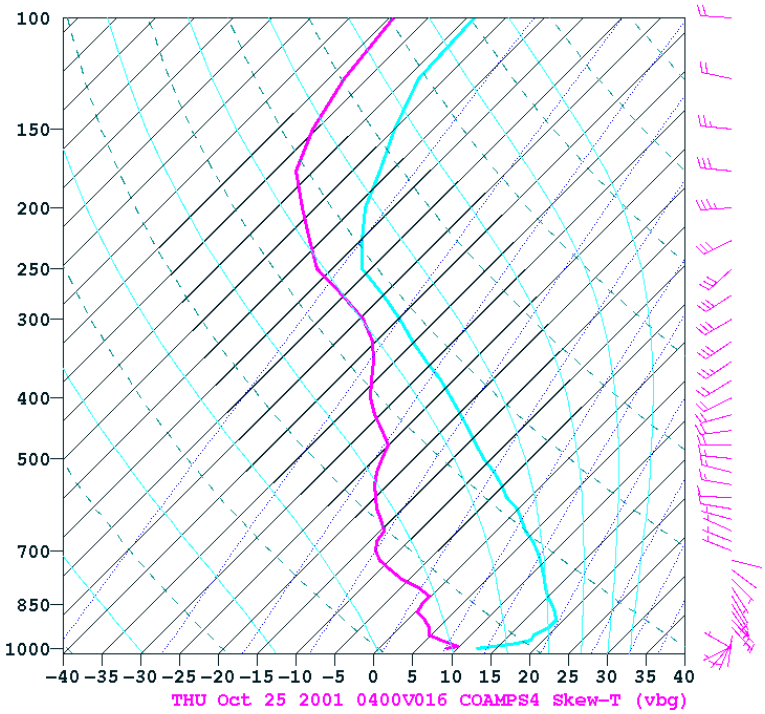

Figure 163. COAMPS forecast for 04Z, 25OCT01.

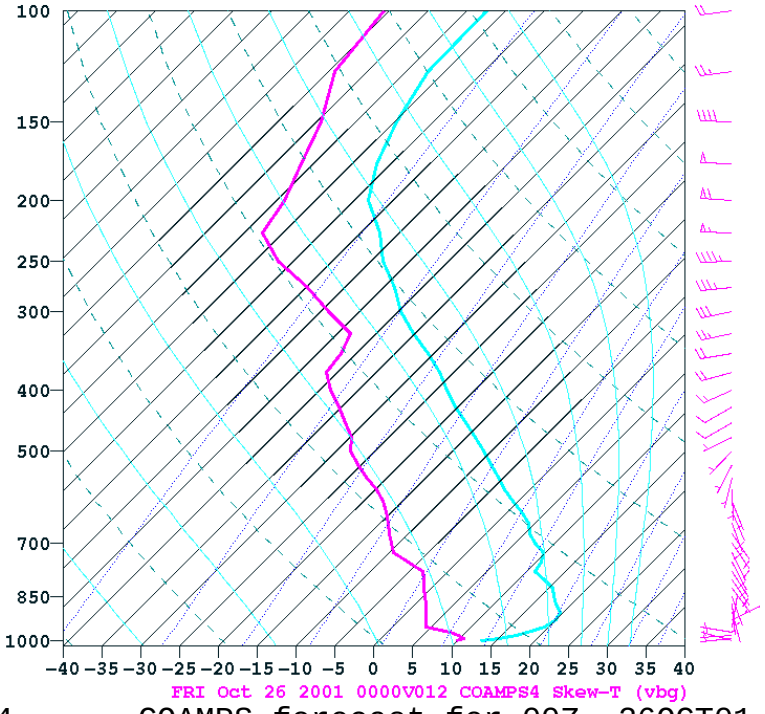

Figure 164. COAMPS forecast for 00Z, 26OCT01.

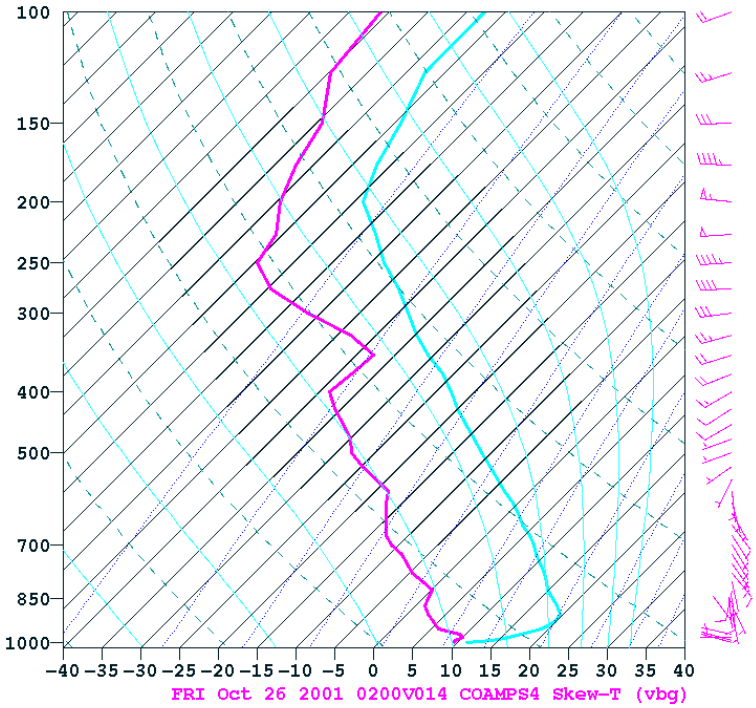

Figure 165. COAMPS forecast for 02Z, 26OCT01.

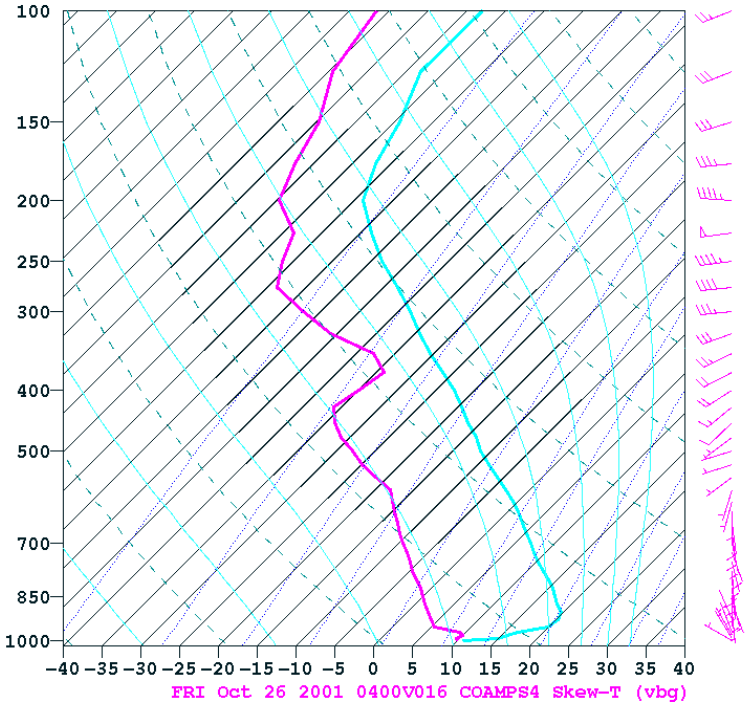

Figure 166. COAMPS forecast for 04Z, 26OCT01.

THIS PAGE INTENTIONALLY LEFT BLANK

APPENDIX H. THERMOSONDE PROFILES

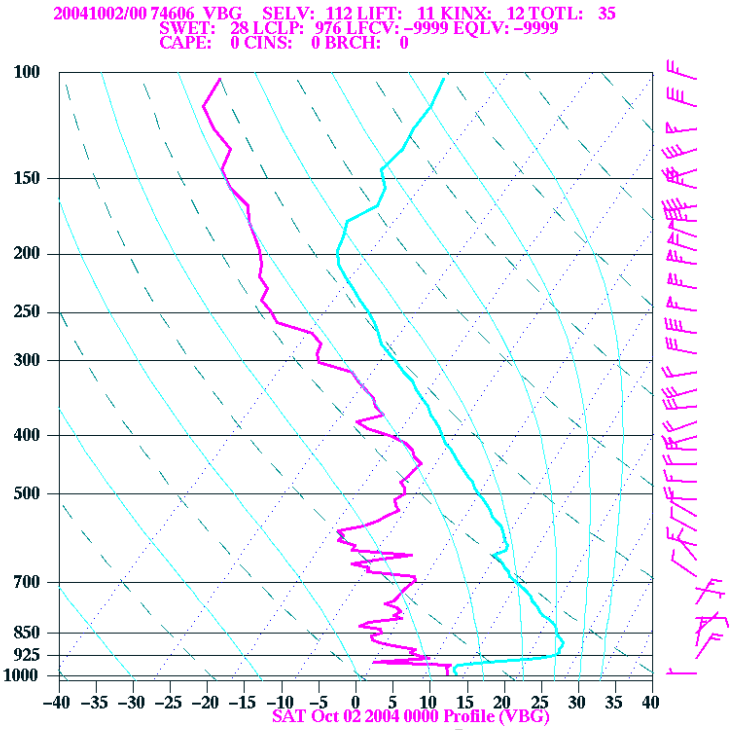

Figure 167. Thermosonde 2, launch time 0132Z 19OCT01.

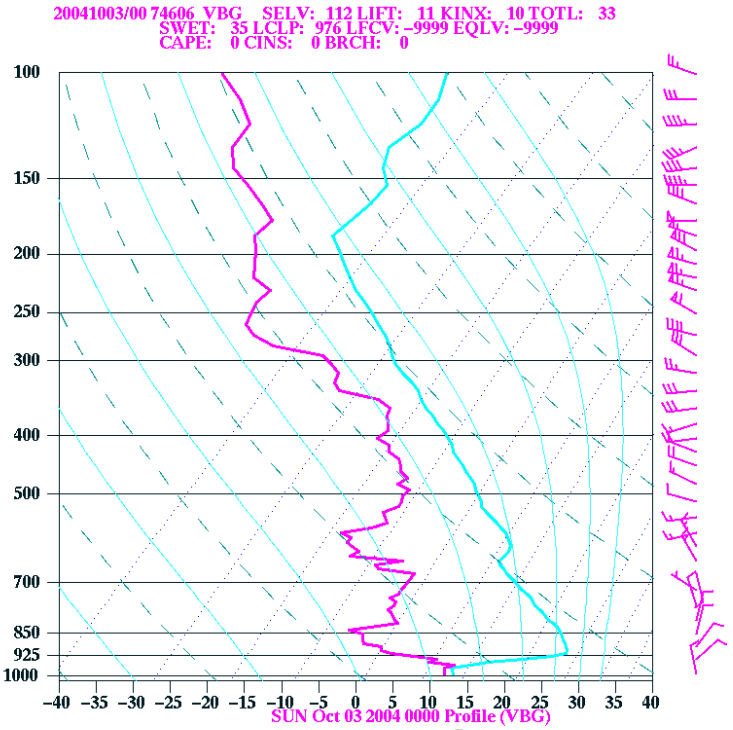

Figure 168. Thermosonde 3, launch time 0322Z 19OCT01.

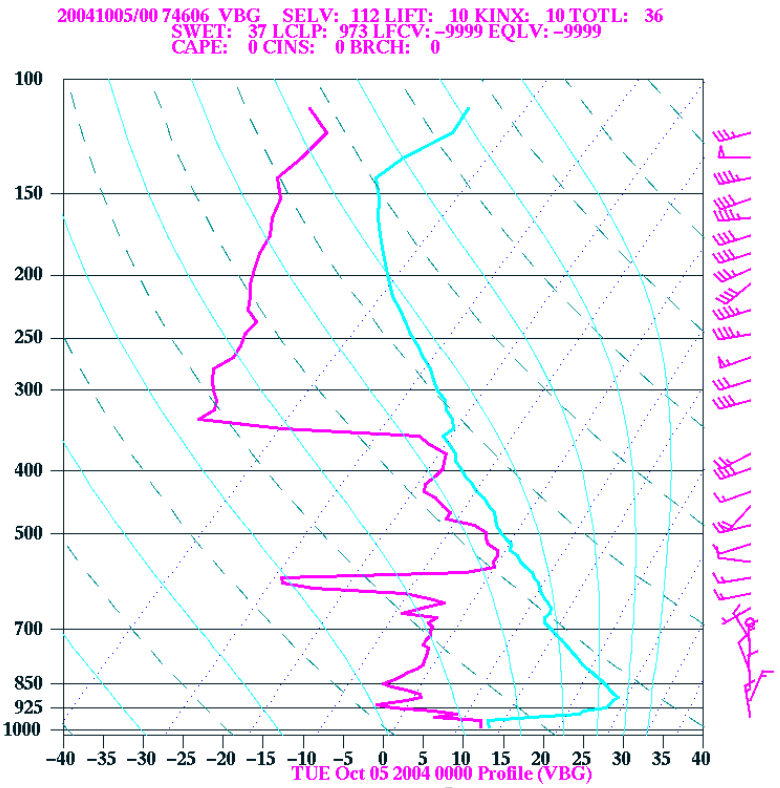

Figure 169. Thermosonde 5, launch time 0115Z 20OCT01.

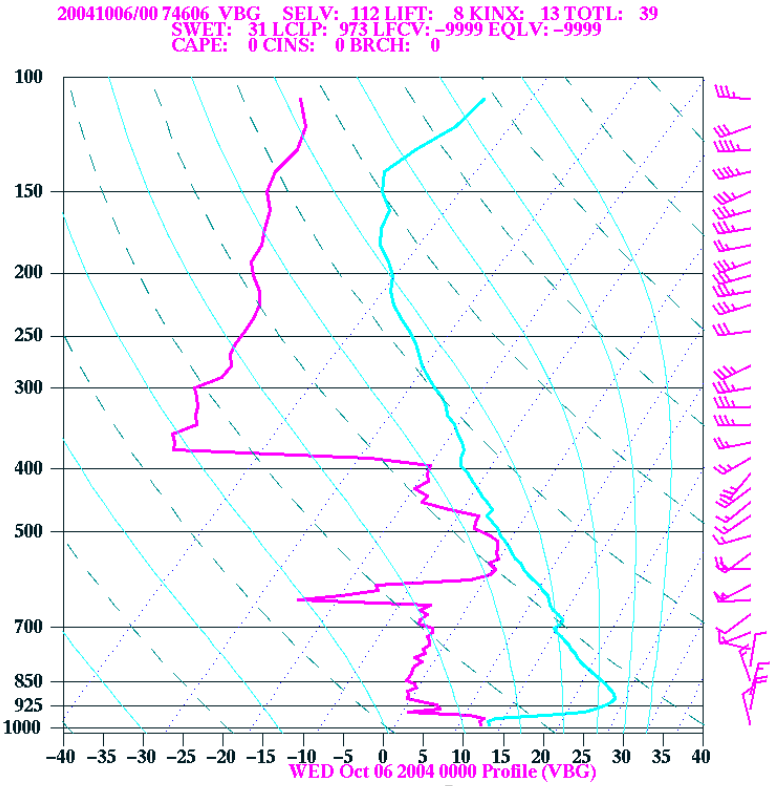

Figure 170. Thermosonde 6, launch time 0300Z 20OCT01.

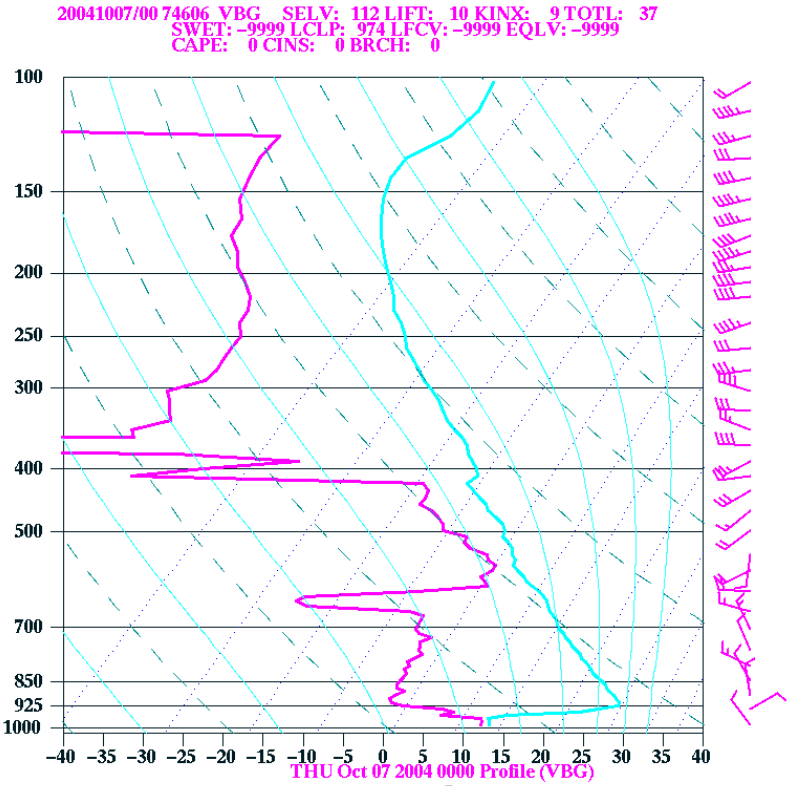

Figure 171. Thermosonde 7, launch time 0444Z 20OCT01.

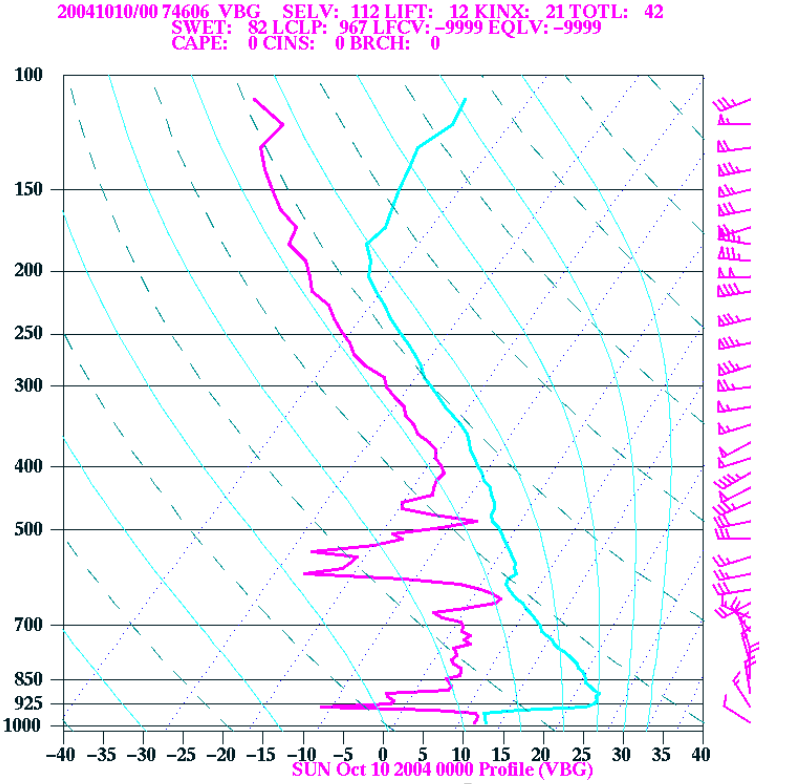

Figure 172. Thermosonde 10, launch time 0235Z 21OCT01.

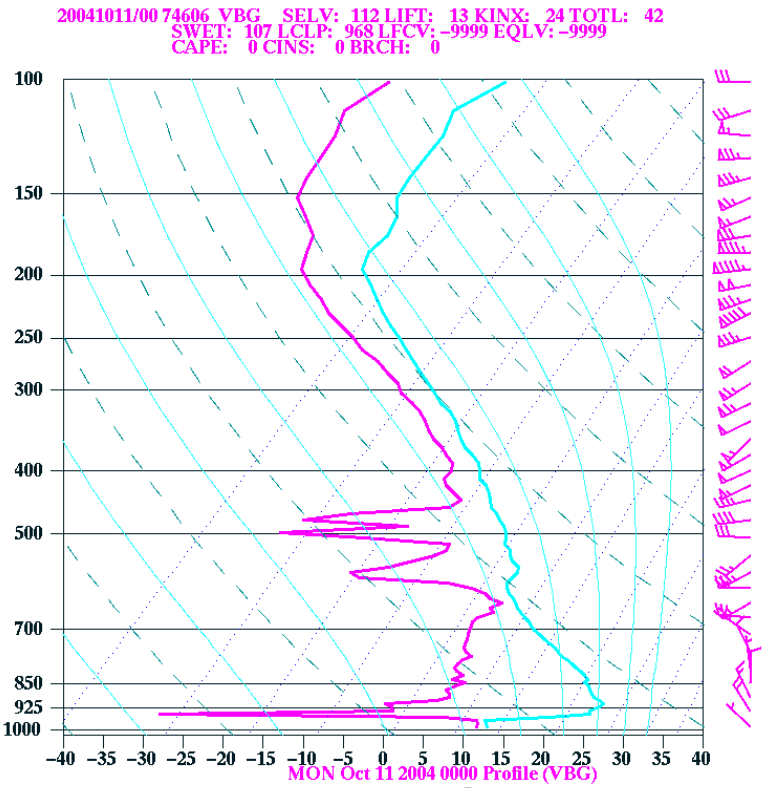

Figure 173. Thermosonde 11, launch time 0413Z 21OCT01.

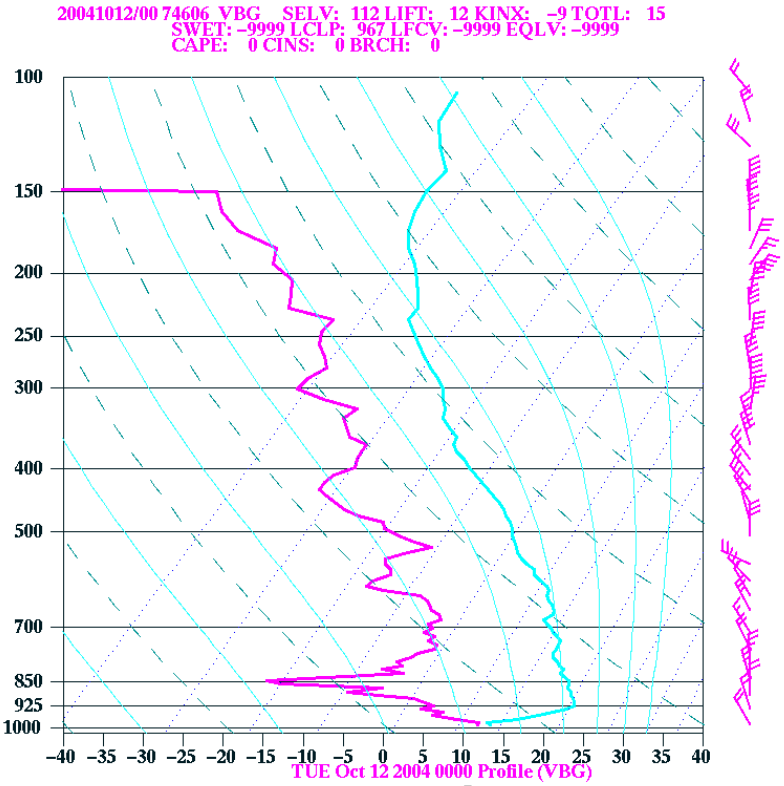

Figure 174. Thermosonde 12, launch time 0115Z 23OCT01.

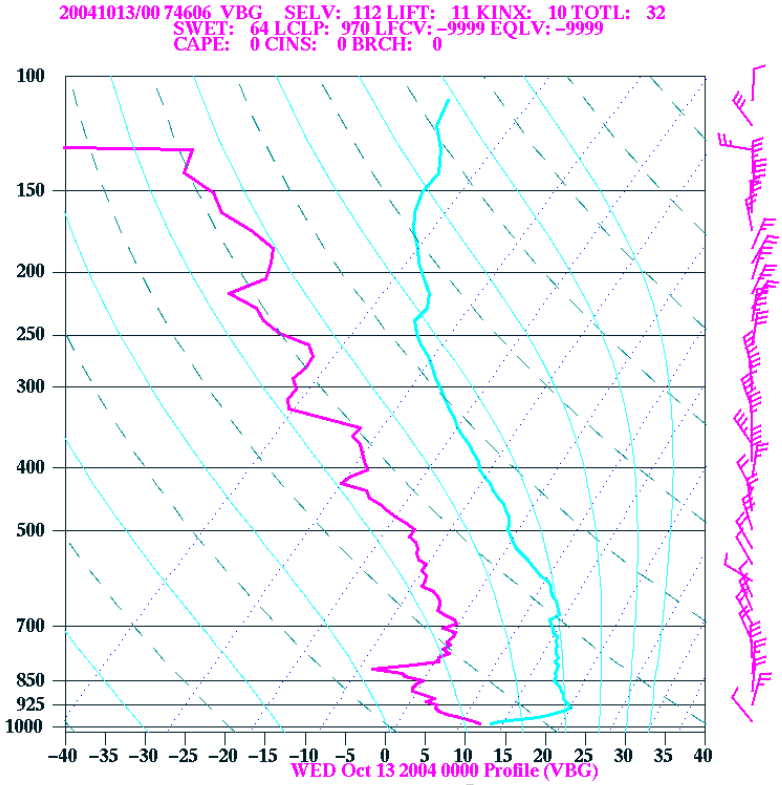

Figure 175. Thermosonde 13, launch time 0254Z 23OCT01.

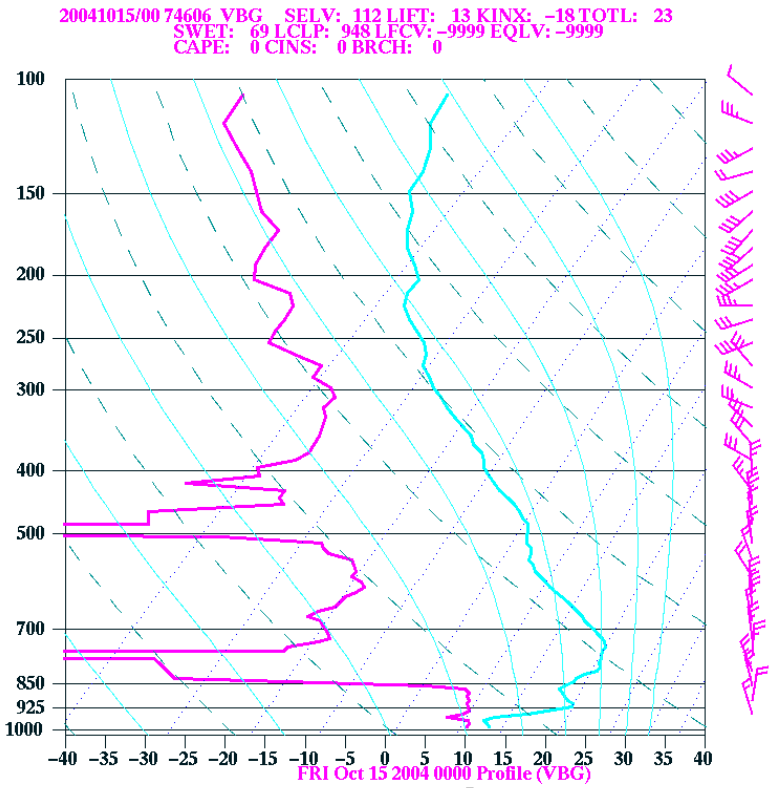

Figure 176. Thermosonde 15, launch time 0114Z 24OCT01.

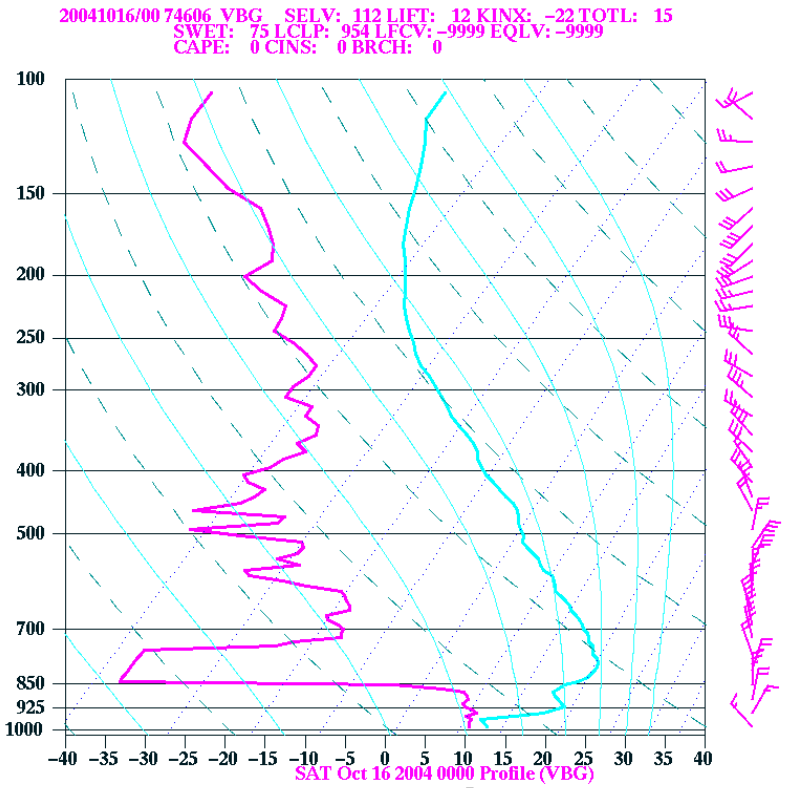

Figure 177. Thermosonde 16, launch time 0248Z 24OCT01.

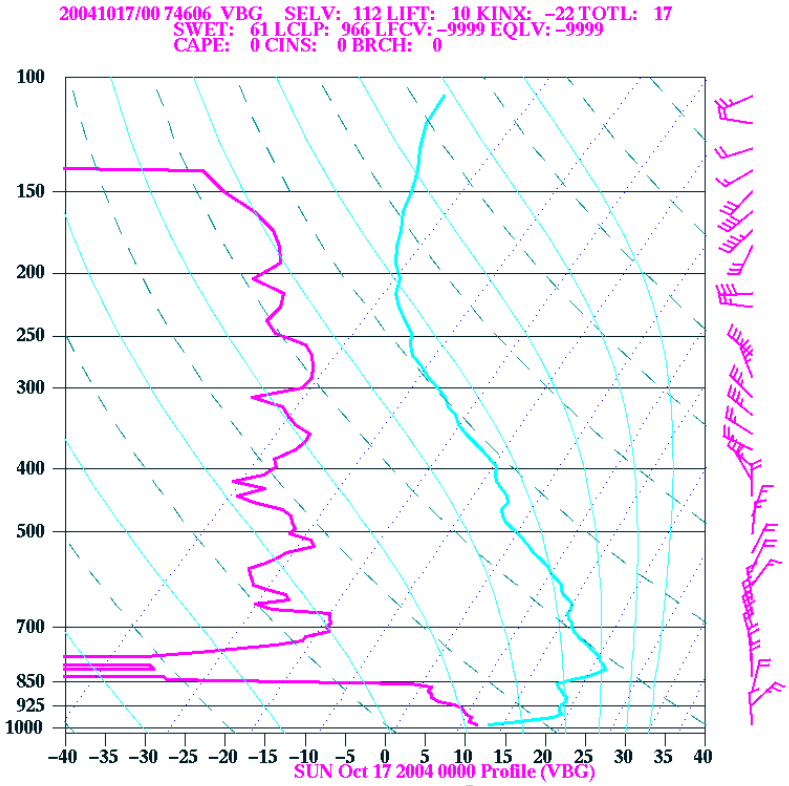

Figure 178. Thermosonde 17, launch time 0430Z 24OCT01.

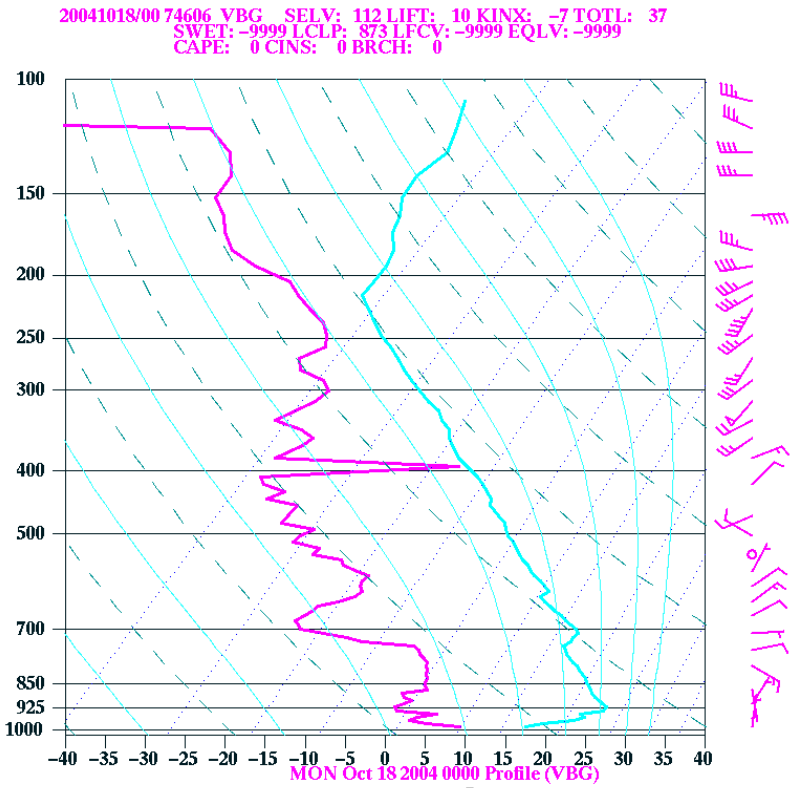

Figure 179. Thermosonde 18, launch time 0115Z 25OCT01.

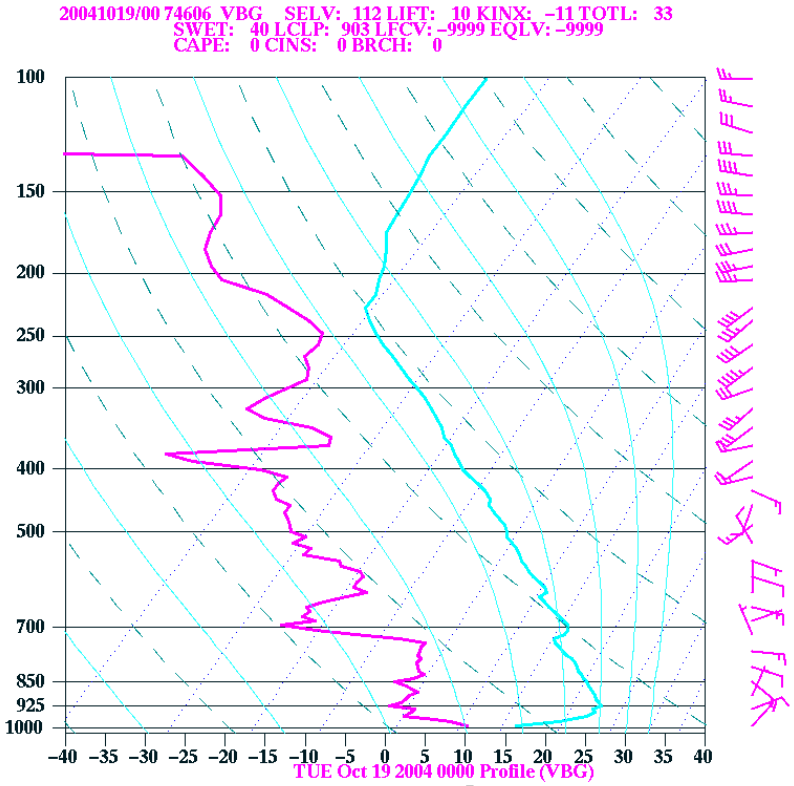

Figure 180. Thermosonde 19, launch time 0253Z 25OCT01.

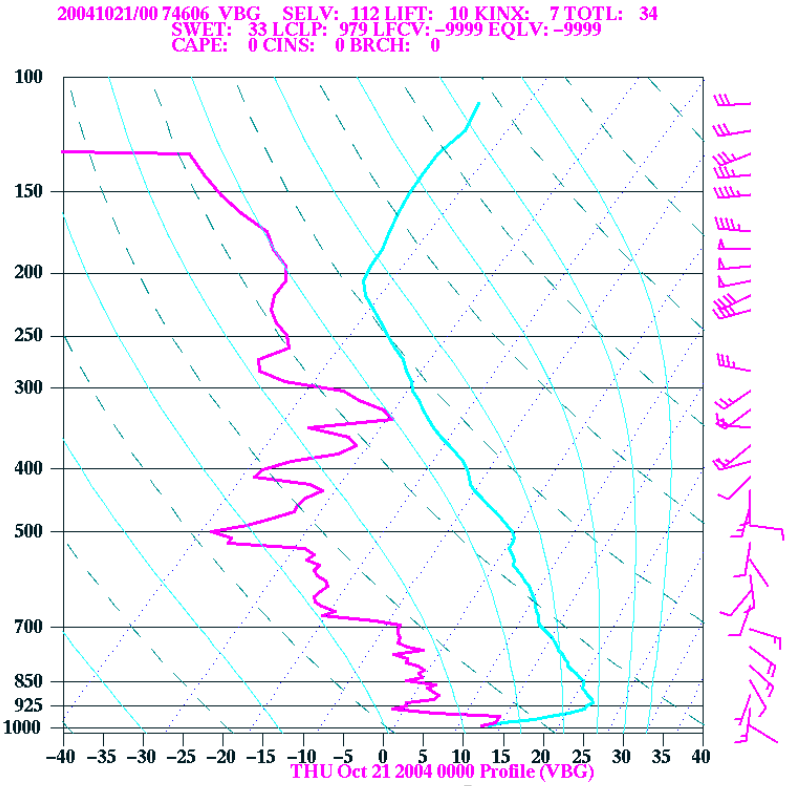

Figure 181. Thermosonde 21, launch time 0249Z 26OCT01.

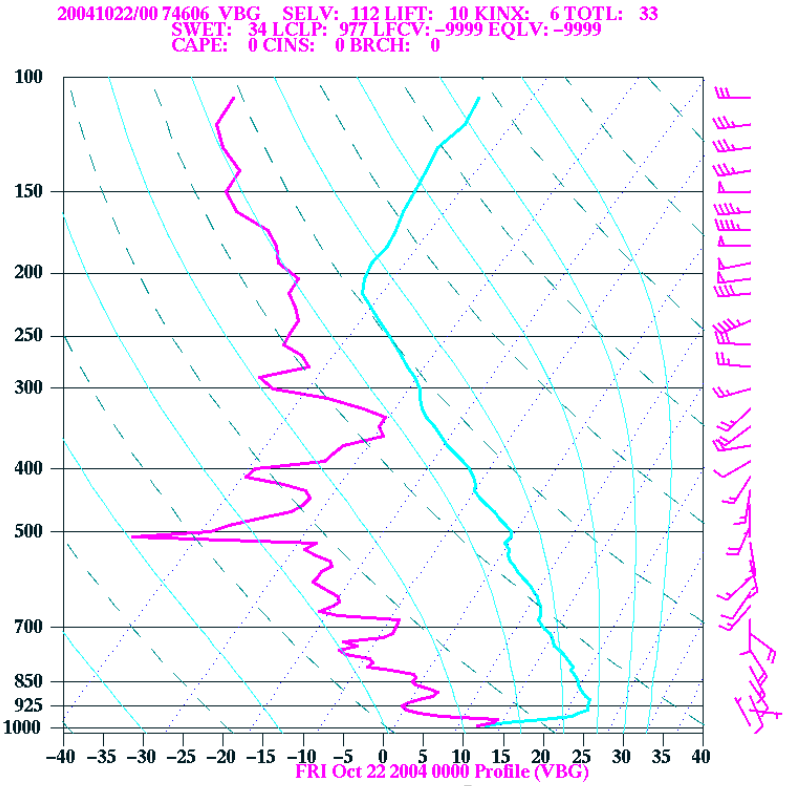

Figure 182. Thermosonde 22, launch time 0423Z 26OCT01.

INITIAL DISTRIBUTION LIST

1. Defense Technical Information Center
   Ft. Belvoir, Virginia

2. Dudley Knox Library
   Naval Postgraduate School
   Monterey, California

3. Chairman, Code MR
   Department of Meteorology
   Naval Postgraduate School
   Monterey, California

4. Professor Douglas K. Miller(Code MR)
   Department of Meteorology
   Naval Postgraduate School
   Monterey, California

5. LCDR Jimmy D. Horne
   Department of Meteorology
   Naval Postgraduate School
   Monterey, California